Dissertation
submitted to the
Combined Faculties for the Natural Sciences and for Mathematics
of the Ruperto-Carola University of Heidelberg, Germany
for the degree of
Doctor of Natural Sciences

Put forward by
M.Sc. Jakob Kunz
born in Schorndorf

Oral examination: 19.04.2017

Active Thermography as a Tool for the Estimation of Air-Water Transfer Velocities

Referees:

Prof. Dr. Bernd Jähne
Prof. Dr. Werner Aeschbach

Abstract
Active thermography offers a tool that can be used to measure air-water transfer velocities at spatial and temporal scales unprecedented by any other measurement technique available. Key to successful measurements is the precise control of a locally applied heat flux density at the water surface. A new way of beam shaping with diffractive optical elements is introduced that significantly increases the spatial homogeneity of the heat flux density. A new multifrequency excitation scheme is developed and successfully implemented that reduces measurement times by a factor of 4 to 12 depending on wind speed. Systematic studies about the dependence of heat transfer on surfactant concentration and fetch length are carried out in the annular wind-wave facility Aeolotron in Heidelberg. The presence of the artificial surfactant Triton X-100 reduces heat transfer for an intermediate wind speed range, but not for extremely low or for high wind speeds. It is found that the heat transfer velocity is strongly dependent on fetch length for low wind speeds. Experiments in the Aeolotron with actual sea water from the North Sea containing natural surfactants show similar results as the measurements with the artificial surfactant Triton X-100. A measurement series in the linear wind-wave facility Pytheas in Marseille, France, shows that wave breaking enhances heat transfer in an intermediate wind speed regime. Simultaneous measurements of heat and gas transfer velocities are in agreement with each other for the sea water conditions investigated in the Aeolotron, when scaled to the transfer velocity of a gas with the same Schmidt number. However, heat transfer velocities are measured to be twice as large as gas transfer velocities in another experimental series with unknown biological activity in the Aeolotron.

Zusammenfassung
Die aktive Thermographie stellt ein Werkzeug zur Messung des Wärmeaustauschs zwischen Luft und Wasser dar, das eine zeitliche und räumliche Auflösung bietet, die sonst keine andere Messtechnik erreicht. Eine Schlüsselkomponente für erfolgreiche Messungen ist die präzise Kontrolle einer lokal induzierten Wärmeflussdichte an der Wasseroberfläche. Eine neue Art der Strahlformung mithilfe von diffraktiven optischen Elementen wird vorgestellt, die die räumliche Homogenität der Wärmeflussdichte signifikant erhöht. Ein neues Anregungsschema, das auf einer Multifrequenzanregung basiert, wird entwickelt und erfolgreich umgesetzt. Dieses Anregungsscheme verringert die Messzeit je nach Windgeschwindigkeit um einen Faktor 4 bis 12. Systematische Untersuchungen der Abhänigkeit des Wärmeaustauschs von Oberflächenfilmkonzentrationen und von der Windwirklänge werden im runden Wind-Wellen Kanal Aeolotron in Heidelberg durchgeführt. Der künstliche Oberflächenfilm Triton X-100 reduziert den Wärmeaustausch in einem mittleren Windgeschwindigkeitsbereich, hat aber keinen Einfluss für sehr kleine oder große Windgeschwindigkeiten. Es stellt sich heraus, dass der Wärmeaustausch für kleine Windgeschwindigkeiten sehr stark von der Windwirklänge abhängt. Experimente im Aeolotron mit echtem Meerwasser aus der Nordsee, die natürliche Oberflächenfilme enthalten, zeigen ähnliche Ergebnisse wie die Messungen mit dem künstlichen Oberflächenfilm Triton X-100. Eine Messreihe im linearen Wind-Wellen Kanal Pytheas in Marseille, Frankreich, ergibt eine Erhöhung des Wärmeaustauschs durch Wellenbrechen in einem mittleren Windgeschwindigkeitsbereich. Gleichzeitige Messungen von Gas- und Wärmetransfergeschwindigkeiten stimmen für die Meerwassermessungen, die im Aeolotron durchgeführt werden, überein, wenn sie auf die Transfergeschwindigkeit eines Gases mit gleicher Schmidtzahl skaliert werden. In einem anderen Experiment am Aeolotron wird hingegen unter dem Einfluss unbekannter biologischer Aktivität eine doppelt so hohe Transfergeschwindigkeit aus der Messung des Wärmeaustauschs ermittelt.

Contents

1. Introduction 1

2. Theory 9
   2.1. Transport - Diffusion and Turbulence . . . 9
      2.1.1. Molecular Diffusion . . . 9
      2.1.2. Turbulence . . . 13
   2.2. Parameters of Turbulent Gas Exchange across the Air-Water Interface 15
   2.3. Models of Turbulent Gas Exchange . . . 19
   2.4. The Influence of Surfactants . . . 23
   2.5. Heat Exchange . . . 24
      2.5.1. Heat Fluxes at the Water Surface . . . 24
      2.5.2. Periodic Heat Flux Densities . . . 25
      2.5.3. Heat as a Proxy Tracer for Gas Exchange . . . 27

3. Experimental Method 29
   3.1. Thermography . . . 29
      3.1.1. Different Types of Sensors . . . 32
      3.1.2. Properties of Water in the IR Regime . . . 34
   3.2. A Brief History of Thermography for the Investigation of Air-Water Heat Transfer . . . 38
   3.3. The Controlled Flux Method . . . 39
      3.3.1. ΔT Method . . . 42
      3.3.2. Amplitude Damping Method . . . 43
      3.3.3. Multifrequency Excitation - Towards Faster Measurements 47
   3.4. Heating an Area . . . 52
      3.4.1. Beam Shaping . . . 53

4. Experimental Setup and Calibration 57
4.1. The Aeolotron . . . 57
4.1.1. Fetch Variation . . . 60
4.1.2. Setup at the Aeolotron . . . 61
4.1.3. Estimating Uncertainties in the Applied Heat Flux Density 63
4.2. Pytheas . . . 67
4.2.1. Setup at Pytheas . . . 68
4.2.2. Minimizing the Uncertainties of the Applied Heat Flux Density . . . 68
4.3. Calibration of the IR Camera . . . 71
4.4. Characterization of the IR Lasers . . . 74
4.5. Diffractive Beam Homogenizers . . . 76

5. Experiments 77
5.1. Systematic Experiments at the Aeolotron with Controlled Boundary Conditions . . . 78
5.2. Sea Water in the Aeolotron with Natural Surfactants . . . 83
5.3. Measurement Campaign 2016 at the Aeolotron with Unknown Biological Activity . . . 87
5.4. Measurement Campaign 2016 at the Large Wind Wave Facility in Marseille . . . 88
5.5. Measurement Procedure . . . 91
5.5.1. Thermographic Measurements - Implementation of the Excitation Schemes . . . 91

6. Data Processing 95
6.1. Selecting the Area of Interest . . . 95
6.1.1. Extrapolating to Thermal Equilibrium . . . 98
6.2. Bad Pixel Correction . . . 100
6.3. Analysis in the Fourier Domain . . . 101
6.3.1. Amplitude Damping Analysis . . . 102
6.3.2. Analysis of the Phase Shift . . . 102
6.4. Correcting for the Penetration Depth of the IR Camera . . . 103

7. Results and Discussion 107
7.1. Improvements of the Measurement Technique . . . 107
7.1.1. Homogeneity of the Applied Heat Flux Density . . . 108
7.1.2. Measurement Uncertainties and Error Discussion . . . 110
7.1.3. New Excitation Pattern . . . 119

7.2. Systematic Study of Heat Transfer Rates under Controlled Conditions . . . 124
7.2.1. Clean Water over an Extended Wind Speed Range . . . 125
7.2.2. Fetch Dependency of Heat Exchange . . . 127
7.2.3. The Influence of Surfactants on Heat Exchange . . . 130
7.3. Sea Water in a Laboratory Environment . . . 136
7.4. Aeolotron with Unknown Biological Activity . . . 145
7.5. Results from the Linear Wind Wave Facility in Marseille . . . 147
7.6. Phase Analysis - An Attempt to Differentiate Between Gas Exchange Models . . . 151
7.7. Comparing Heat and Gas Exchange . . . 155

8. Conclusion and Outlook 163
8.1. Conclusion . . . 163
8.1.1. Advancement of the Measurement Technique . . . 163
8.1.2. Systematic Study of Heat Exchange . . . 164
8.1.3. Heat Exchange under Laboratory Sea Water Conditions . 165
8.1.4. Measurement Campaign in Marseille . . . 166
8.1.5. Differentiating Gas Exchange Models . . . 166
8.1.6. Comparison of Heat and Gas Exchange . . . 166
8.2. Outlook . . . 167
8.2.1. Quantitative Comparison of Locally Measured Heat and Gas Exchange . . . 167
8.2.2. New Thermographic Setup as a Powerful Tool for Field Campaigns . . . 168

Bibliography 169

A. Appendix 181
A.1. Tables of the Results of all Measurements . . . 181
A.2. Estimating Heat Flux Variations . . . 191
A.3. Bad Pixel Removal . . . 194

1 Introduction

Exchange between Ocean and Atmosphere

Knowledge about the exchange of gases between the ocean and the atmosphere is a key component for the understanding of the climate system. The exchange of volatile chemical species is not only important in the context of climate change, but it also plays an important role in the distribution of toxic gases, which for example becomes important after an industrial accident at a chemical facility. On a global scale the ocean is the largest sink for atmospheric CO_2 [68]. This means that the transport of CO_2 from the atmosphere into the ocean is a dominant process that slows down the intensification of the greenhouse effect. However, this slow down of climate change comes at a cost: dissolved CO_2 leads to an acidification of the oceans [26], which threatens sea organisms such as corals [81].

Predicting the future of the earth's climate thus strongly relies on the ability to accurately model the exchange process between the atmosphere and the ocean. However, despite intense research for more than thirty years, no accurate description for gas exchange that is based on physical mechanisms is yet available. The commonly used parametrizations for gas exchange [70, 102, 80, 104, 98, 46] are based on the relationship between the gas exchange rate and the wind speed. This is convenient from a practical point of view, since wind speed measurements have a good global coverage, as they can be performed from satellites with high accuracy [12]. While being convenient to use, the empirical parametrizations suffer from large uncertainties. For example for a typical wind speed of 7 m/s, the predictions from the parametrizations differ by a factor of two [59]. However, despite these uncertainties, nearly all climate models rely on a simple empirical description, which models the exchange rate of CO_2 with a quadratic function of the wind speed [40].

Parameters Influencing the Exchange Process

The uncertainties in the parametrizations of the gas exchange rate that based on wind speed can be understood by looking into the processes driving the exchange. The main barrier for the exchange of sparingly soluble gases between an air and a water phase is controlled by a 20 to 200 µm thin layer that is called the aqueous mass boundary layer [55]. Within this layer molecular diffusion is the dominant transport mechanism which is much less effective than turbulent transport. Wind stress at the water surface causes momentum transport into the water which introduces near surface turbulence. The wind also causes the growth of waves via form drag [83]. Depending on the wind speed different processes such as Langmuir circulations [100, 74], microscale wave breaking [115] and wave breaking with bubble entrainment influence gas exchange. All these phenomena depend on the momentum input by wind. If the fluid dynamics at the surface are altered by the presence of a surface active material, gas exchange will be affected as well. Reduction of gas exchange up to 80% in the presence of surface active material has been reported [13]. Other studies also find significant reduction of the transfer rate of gases [56, 30, 29] and also of heat [31, 91]. On top of the strong influence of the transfer rate on surfactants, the presence of surface films is not a rare situation on the oceans, but many of the oceans are covered to a significant amount by surfactants [109, 110]. Obviously a parametrization that is solemnly based on wind speed does not take the actual dynamics at the water surface into account and thus cannot account for this important influence on gas exchange.
Due to this deficiency of the wind speed parametrizations, another parametrization that uses the mean square slope (mss) of the water surface was proposed [58, 31]. mss is a statistical property of the wave field and serves as a measure for the surface roughness. Promising correlations between mss and gas transfer rates have been observed, especially in the case of surfactants [8, 31].

Measuring Gas Exchange Rates

Measuring gas exchange is commonly done by mass balance methods. These methods are based on monitoring concentration changes of a certain tracer over time. Tracers can be added artificially into the environment or naturally occurring species can be chosen. For the latter option the radon deficit method is the most prominent example. The equilibrium concentration ratio between ^{222}Rn and ^{226}Ra is changed due to the evaporation of ^{222}Rn out of the ocean [89, 84, 7].

The concept of mass balance methods is to monitor the concentration changes of e.g. the air side concentration of a tracer over time and to attribute a decrease or increase in concentration to the exchange with the water phase. Although well applicable in laboratory experiments, where boundary conditions such as wind speed can be controlled and kept constant and air and water compartments are closed with respect to the ambient environment, this assumption hardly holds on the ocean, where currents and winds also contribute to concentration changes by diluting the initial concentration. To account for such effects the dual tracer method has been introduced [106, 105]. The ratio of concentrations of two artificially added tracers is monitored instead of the concentration of a single tracer. However, this approach is limited to tracers with very different diffusion coefficients, because otherwise the concentration ratio will change too slowly. Commonly ^{3}He and SF_6 are used for dual tracer measurements. Still it takes between 12 and 24 hours to detect a significant change in the concentration ratio. For the radon deficit method mentioned above the temporal resolution is limited by the decay time, the half life of ^{222}Rn being 3.8 days. These temporal resolutions yield spatial resolutions of around tens of kilometres for the dual tracer method and hundreds of kilometres for the radon deficit method [40].
Besides the mass balance methods the eddy covariance method is used, which directly measures the turbulent fluctuations of wind speed and trace gas concentration. For a successful application of the method the measurement device must have a fast readout time to capture all turbulent fluctuations, but the over all measurement time must also be long enough to capture fluctuations on all relevant scales. Typical measurement times are between 10 and 60 minutes [40]. The spatial resolution that can be achieved is then around 10 kilometres.
Small scale techniques measuring concentration profiles of trace gases are available via the laser induced fluorescence (LIF) technique [76, 44, 33, 34]. However, this technique cannot be applied at large wind wave facilities or even in the field. An overview of the temporal and spatial resolutions of commonly used measurement techniques is shown in figure 1.1.
The only technique able to measure transfer rates with a spatial resolution of about a square metre and a temporal resolution of 5 minutes to one hour is thermography. The application of thermography as a tool to estimate heat transfer rates has already been introduced in the late 1980s by Jähne [55]. The technology of the available measurement devices at that time limited the application of the measurement technique and it wasn't until the mid 1990s and the technological advancement of infrared cameras and the introduction of powerful CO_2 lasers that the technique became more popular. This technique is also well applicable in the laboratory, which makes it a perfect bridging technology between laboratory and field measurements.

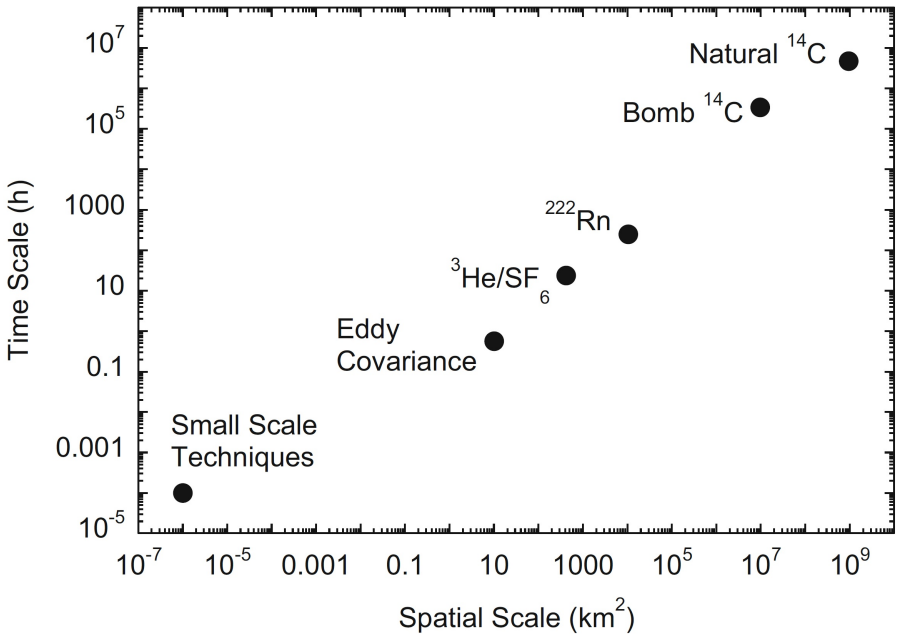

Figure 1.1.: Typical spatial and temporal resolutions of commonly used experimental methods to derive gas transfer rates at the air-water interface. Figure taken from Garbe [40].

There is however a major issue with thermographic measurements. They don't measure gas exchange rates directly, but they measure heat exchange rates. Scaling heat transfer rates to gas transfer rates is done by Schmidt number scaling, but since the diffusion coefficients of heat and CO_2 in water differ by two orders of magnitude, there are still controversies if Schmidt number scaling is applicable for such large differences in the diffusion coefficient. Experimentally the situation is ambiguous, there are studies that find differences between gas and heat transfer rates after scaling them to transfer rates of a gas with the same Schmidt number [6, 5, 3], while other studies find scaled gas and heat transfer rates to be in good agreement with each other [77].

Objectives and Structure of the Thesis

There were mainly two objectives for this thesis. The first one was to improve the experimental setup and the measurement scheme used to conduct thermographic measurements at the air-water interface. The second aim of this thesis was to use the improved measurement technique and to conduct a systematic study of heat transfer across the aqueous boundary layer for a variety of laboratory conditions. In addition a study with actual sea water from the North Sea that had been transported to the annular wind-wave facility Aeolotron in Heidelberg as well as a measurement campaign at the large linear wind-wave facility in Marseille-Luminy, France, were carried out during this thesis.

Advancing the Measurement Technique

As mentioned above thermography is the most promising tool for the investigation of heat and gas transfer in the field. For successful experiments on the ocean a robust and reliable experimental apparatus is needed, that is able to estimate heat transfer rates with a high accuracy. Therefore, the first important task for this thesis was to improve the existing experimental setup as used by Nagel [77]. On top of that, new excitation schemes were to be implemented that allow for even shorter measurement durations and thus a higher temporal resolution.

Improvement of the Experimental Setup Since Jähne's introduction of thermographic measurements at the water surface [55], the experimental setup has

changed significantly. The latest evolution stage, driven by technological advancement, was the setup implemented in the laboratory by Popp [85] that was later used by Nagel [77, 78] in field campaigns. However, this setup suffers from an poor way of beam shaping, which causes a gradient in the laser intensity profile that leads to inhomogeneities of more than 50% in the heat flux density at the water surface. The applied heat flux density at the water surface is the core of the experimental approach, which means that any uncertainty in the heat flux density directly affects the whole measurement. The aim of this thesis was to improve the experimental setup by homogenizing the applied heat flux density and thereby to reduce uncertainties and to increase the overall measurement accuracy.

Implementation of New Excitation Schemes The spatial homogenization of the heat flux density allows for the implementation of another measurement scheme, which leads to a dramatic increase in the temporal resolution of the measurements. This is of profound importance for a device that is aimed for the application in the field. If systematic measurements on the ocean should be possible, measurement times must be kept low, because the boundary conditions like wind speed are likely to change quickly. If a measurement is done during the change of the wind speed for example, the result is biased by this change and distinct conclusions on e.g. the wind speed dependence cannot be drawn from the measurement. An example for the variability of boundary conditions in a complex system is shown in figure 1.2, where heat transfer velocities obtained during a laboratory experiment with actual sea water in the Heidelberg annular wind-wave facility Aeolotron are shown. It can be seen, that at the same wind speed of 5.8 m/s two different values for the heat transfer velocity have been measured. This is due to the influence of natural surfactants on the dynamics at the water surface. These two different values for the heat transfer velocity were obtained within a measurement duration of only 20 minutes, while the wind speed was kept constant. This underlines the variability of the highly complex air-water boundary system and the importance of fast measurements. The second aim of this thesis was thus to implement two new measurement schemes that increase the temporal resolution of the measurements.

Systematic Laboratory Studies

Thermography represents the ideal bridge technology between laboratory and field experiments. However, while for gas exchange systematic laboratory stud-

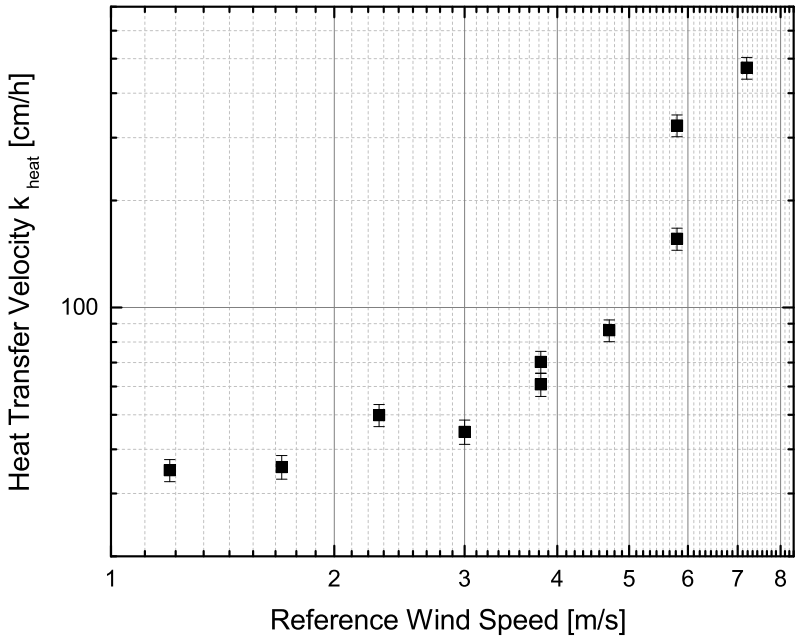

Figure 1.2.: Example for the change of boundary conditions within short time. Two different transfer velocities k_{heat} have been estimated for the same wind speed of 5.8 m/s due to the beak up of a surface film. This break up happened within only 20 minutes of measurement time, underlining the importance of fast measurements if the influence of such effects should be distinguished.

ies for a wide range of boundary conditions are available, e.g. Krall [62], not many comprehensive systematic laboratory studies for wind driven heat exchange are available. The second aim of this thesis was thus to change this situation and to conduct systematic measurements investigating the influence of wind speed on heat exchange, as well as the influence of different degrees of contamination with an artificial surfactant and the dependency of heat exchange on the so called fetch length, i.e. the interaction length between wind and water.

Natural Sea Water Conditions in the Laboratory

In November 2014 actual sea water from the North Sea with natural surfactants was used for an extensive experiment in the large annular wind-wave facility Aeolotron in Heidelberg. One aim of the experiment was to do comparative measurements of heat and gas exchange under conditions as natural as possible in a laboratory and to gain further experimental evidence if heat transfer rates can be scaled to gas transfer rates.

Measurement Campaign in Marseille

Finally, the portability of the thermographic system had to be demonstrated during a measurement campaign at the large linear wind-wave facility Pytheas at the University of Marseille, France, in June 2016. The aim of this measurement campaign was to investigate the influence of breaking waves on heat and gas transfer. This is a subject that can be well studied at the Marseille facility, as wave breaking conditions can be realized by the use of a mechanical wave generator at Pytheas.

Theory 2

This chapter is dedicated at explaining the fundamentals of gas and heat exchange between air and water. The first section presents two important transport mechanisms, molecular diffusion and turbulence. In the next section the most important parameters of gas and heat exchange are presented that are later needed to describe the measurements. A short overview of the most common gas exchange model descriptions is given in the third part of this chapter. In the forth section the influence of surface active material is addressed. In the last section of this chapter a description of heat exchange between air and water is given. Here, an important aspect is the application of heat as a proxy tracer for gas exchange.

2.1. Transport - Diffusion and Turbulence

Diffusion and turbulence are the important transport mechanisms for the exchange of gases, heat and momentum across the air-water interface. Far away from the interface turbulence is the dominant transport process, as it is much more effective than molecular diffusion. However turbulent eddies cannot penetrate the air-water interface and thus in a very small layer around this interface molecular diffusion becomes the dominant process.

2.1.1. Molecular Diffusion

Molecular diffusion is based on the thermal motion of atoms and molecules. The velocity of these particles is given by the Boltzmann distribution. The direction of

the motion is purely random and can be described stochastically by the random walk model [82]. Elastic collisions between the molecules in a medium cause a certain direction of the transport from a region with a higher concentration to a region with a lower concentration. A macroscopic description that links the flux density given by the motion of the molecules and the concentration difference is given by Fick's fist law [28]:

$$\vec{j}_{gas} = -D\vec{\nabla}c \tag{2.1}$$

here $\vec{j}_{gas}$ is the flux density of a certain gas, c is the concentration of this gas and D is the so called diffusion coefficient, a material constant.
For heat and momentum analogue equations can be formulated. For heat Fourier's law

$$\vec{j}_{heat} = -\lambda\vec{\nabla}T \tag{2.2}$$

links heat flux density $\vec{j}_{heat}$ and the temperature gradient $\vec{\nabla}T$ via the thermal conductivity number λ:

$$\lambda = \chi c_p \rho \tag{2.3}$$

χ is the heat conductivity, ρ the density and c_p the specific heat coefficient for constant ambient pressure.
Newton's law of viscosity

$$\vec{j}_{momentum} = -\nu\vec{\nabla}(\rho\vec{u}) \tag{2.4}$$

describes the proportionality of the momentum flux density $\vec{j}_{momentum}$ and the momentum divergence $\vec{\nabla}(\rho\vec{u})$, where ρ is the density and $\vec{u}$ the mean velocity via the kinematic viscosity ν.
To describe the relation between diffusion of momentum and matter, the so called Schmidt number Sc is used:

$$Sc = \frac{\nu}{D} \tag{2.5}$$

For heat the Prandtl number Pr is used

$$Pr = \frac{\nu}{\chi} \tag{2.6}$$

The Prandtl number and the Schmidt numbers of most gases in air are close to one. However in water large differences in the Schmidt number occur. Figure 2.1 gives an overview of the range of Schmidt numbers of a variety of volatile trace gases.

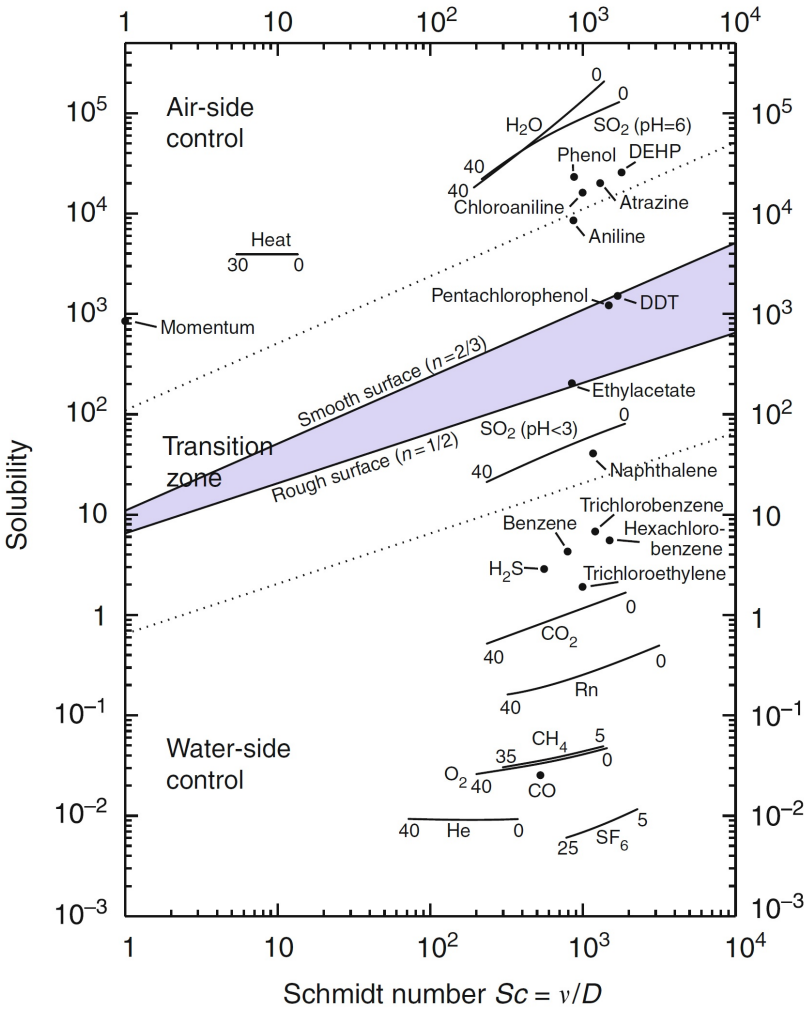

Figure 2.1.: An overview of the Schmidt numbers and solubility of a variety of volatile trace gases. Figure taken from [40], based on [52]. Note the large difference in solubility and Schmidt number between heat and CO_2.

For media without any sources or sinks the continuity equation can be applied:

$$\frac{dc}{dt} = -\vec{\nabla}\vec{j}_{gas} \tag{2.7}$$

Inserting Fick's first law (equation 2.1) into equation 2.7 yields Fick's second law [28] that describes temporal changes of the concentration:

$$\frac{dc}{dt} = D\Delta c \tag{2.8}$$

For heat and momentum the equations read as

$$\frac{dT}{dt} = \chi\Delta T \tag{2.9}$$

and

$$\frac{d\vec{u}}{dt} = \nu\Delta\vec{u} \tag{2.10}$$

Applying the so called material derivative, equation 2.8 can be split up into

$$\frac{dc}{dt} = \frac{\partial c}{\partial t} + \vec{u}\vec{\nabla}c \tag{2.11}$$

Inserting the continuity equation 2.7 yields for the transport equation

$$\frac{\partial c}{\partial t} = D\Delta c - \vec{u}\vec{\nabla}c \tag{2.12}$$

The first part in equation 2.12 denotes the transport due to molecular diffusion and the seconds part describes the advective transport due to the mean velocity $\vec{u}$ of the medium. Equation 2.12 can be rewritten if

$$\vec{u}\vec{\nabla}c = \vec{\nabla}c \cdot \vec{u} - c \cdot \vec{\nabla}\vec{u} \tag{2.13}$$

is used, where $\vec{\nabla}\vec{u} = 0$ for incompressible fluids:

$$\frac{\partial c}{\partial t} = -\vec{\nabla}\left(\vec{j}_{diff} + \vec{j}_{adv}\right) \tag{2.14}$$

with the diffusive contribution $\vec{j}_{diff}$ and the advective contribution $\vec{j}_{adv}$ to the flux density.
A more detailed description of molecular diffusion can be found e.g. in [19].

2.1.2. Turbulence

Turbulence is driven by statistical fluctuations in the velocity field. Close to boundaries, turbulence can be described by eddies, whose length's scale is dependent on the distance to the interface. This is why turbulence is very effective far away from the air water interface, where large eddies are present. Close to the interface the eddies become very small and at some point molecular diffusion starts to become the dominant transport mechanism.
The general transport equation as given by equation 2.12 cannot be solved, as the exact velocity field is unknown. This velocity field is the solution of the Navier-Stokes equation for incompressible fluids:

$$\frac{\partial \vec{u}}{\partial t} + \vec{u}\nabla\vec{u} = \vec{f} - \frac{1}{\rho}\nabla p + \nu\Delta\vec{u} \tag{2.15}$$

Here, ν is the kinematic viscosity, p the pressure, ρ the density and $\vec{f}$ the resulting body force from all forces acting on the fluid. Due to the part $\vec{u}\nabla\vec{u}$ in equation 2.15 the equation is not linear. This non-linearity in the Navier-Stokes equation also means that in general there is no analytical solution for the equation. Exact solutions are only available for special cases and boundary conditions where the equation can be reduced to a linear equation [86]. The non-linearity in $\vec{u}$ is caused by the fact that the velocity $\vec{u}$ itself is the transported quantity.
To approximate a solution for the gas exchange and to describe turbulent transport in analogy to molecular diffusion, it is convenient to use the Reynold's decomposition. However, this analogy is only valid for long time periods or stationary situations [66]. The idea behind the Reynold's decomposition is to split concentration and velocity into a temporal mean value and a fluctuation:

$$c = \overline{c} + c' \tag{2.16}$$

and

$$\vec{u} = \overline{\vec{u}} + \vec{u}' \tag{2.17}$$

For long time periods averaging over the fluctuating concentration and velocity components yields:

$$\overline{c'} = 0 \tag{2.18}$$

$$\overline{\vec{u}'} = 0 \tag{2.19}$$

Assuming a stationary one dimensional flow in x-direction, equation 2.12 simplifies to

$$\frac{\partial \overline{c}}{\partial t} = \frac{\partial}{\partial z}\left(D\frac{\partial \overline{c}}{\partial z} - \overline{c' u_z'}\right) \tag{2.20}$$

where z is the vertical direction and u_z' is the vertical velocity component. In analogy the velocity field is given by

$$\frac{\partial \overline{u}}{\partial t} = \frac{\partial}{\partial z}\left(\nu\frac{\partial \overline{u}}{\partial z} - \overline{u_x' u_z'}\right) \tag{2.21}$$

using the Reynold's decomposition. u_x is the velocity components along x direction.
Using the continuity equation 2.7 the mean flux density of the concentration can be expressed as

$$\overline{j_{gas}} = -D\frac{\partial \overline{c}}{\partial z} + \overline{c' u_z'} \tag{2.22}$$

Comparison with the diffusion equation given by Fick's first law (equation 2.1) shows that the term $\overline{c' u_z'}$ accounts for the turbulent transport. A turbulent diffusivity K_c can be formulated under the assumption that the turbulent transport is proportional to the concentration gradient:

$$\overline{c' u_z'} = -K_c(z)\frac{\partial \overline{c}}{\partial z} \tag{2.23}$$

Inserting the turbulent diffusivity into equation 2.20 and using the continuity equation 2.7 results in

$$j_{gas} = -\left(D + K_c(z)\right)\frac{\partial \overline{c}}{\partial z} \tag{2.24}$$

Analogously one obtains the momentum transport

$$j_{momentum} = -\rho\left(\nu + K_m(z)\right)\frac{\partial \overline{u_x}}{\partial z} \tag{2.25}$$

as the sum of the diffusive and turbulent transport with the turbulent viscosity

$$\overline{u' u_z'} = -K_m(z)\frac{\partial \overline{u_x}}{\partial z} \tag{2.26}$$

In analogy to the turbulent diffusivity also a turbulent Schmidt number Sc_{turb} can be defined:

$$Sc_{turb} = \frac{K_m}{K_c} \tag{2.27}$$

In order to quantify the level of turbulence, the Reynolds number Re can be used:

$$Re = \frac{ul}{\nu} \tag{2.28}$$

Here, u is the mean velocity of a medium, ν is the kinematic viscosity of the medium and l is a characteristic length scale. Small Reynolds numbers describe laminar flow. Above a certain critical Reynolds number the velocity field will become unstable and the flow will become turbulent.

2.2. Parameters of Turbulent Gas Exchange across the Air-Water Interface

The transport of gases between air and water is dominated by the boundary layer at the air-water interface. Turbulent eddies cannot penetrate through this boundary layer due to the large difference of air and water densities ($\rho_{water}/\rho_{air} \approx 780$). Instead the eddies get smaller when approaching the water surface [86]. Within the boundary layer molecular diffusion dominates the transport of trace gases and heat due to the reduced amount of turbulence. Following the description given in section 2.1.2 this can be expressed as

$$K < D \tag{2.29}$$

Far away from the boundaries in contrast large turbulent eddies are present and

$$K \gg D \tag{2.30}$$

This means, that the entire exchange process of gases, heat and momentum between air and water is dominated by a bottleneck represented by the boundary layer at the air-water interface.

Boundary Layer and Transfer Velocity

When approaching the water surface turbulence becomes less and less important until at some point molecular diffusion becomes the dominant transport mechanism. Directly at the water surface only molecular diffusion is possible.

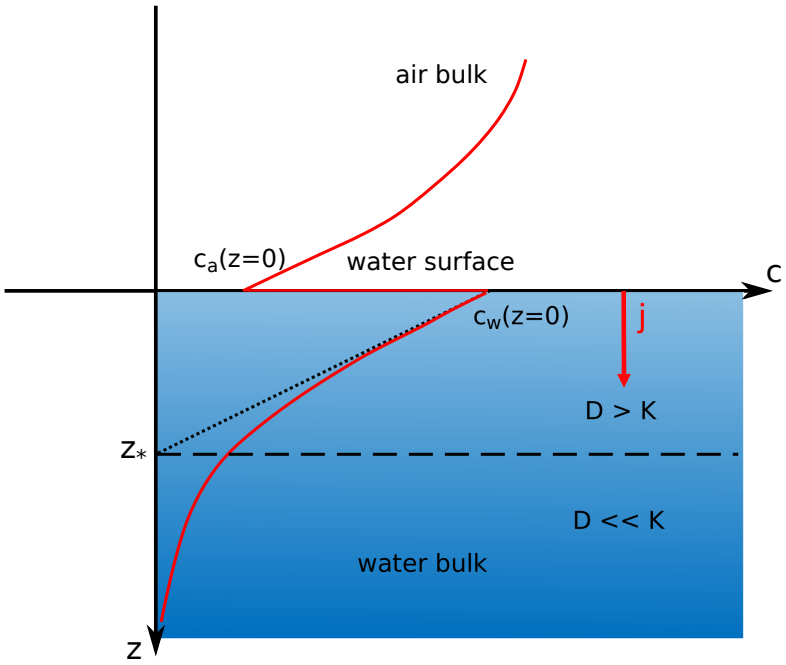

Figure 2.2.: Schematic representation of a concentration profile for an invasion for a gas with a solubility $\alpha > 1$. The mass boundary layer is indicated by the dashed line at z_*.

For a plane water surface in the x-y plane and a vertical z direction the transport equation thus becomes

$$j_{gas} = -D \frac{\partial \bar{c}}{\partial z}\bigg|_{z=0} \tag{2.31}$$

This means, that the concentration gradient directly at the water surface is directly proportional to the flux density. To describe the transport of gases macroscopically, the so called transfer velocity k is used:

$$k = \frac{j}{\Delta c} \tag{2.32}$$

The transfer velocity is thus the proportionality constant between the flux density and the concentration difference between the air and the water phase. Combining equations 2.31 and 2.32 yields the so called boundary layer thickness z_*:

$$z_* = \frac{\Delta c}{(\partial \bar{c}/\partial c)\,|_{z=0}} = \frac{D\Delta c}{j} = \frac{D}{k} \tag{2.33}$$

Figure 2.2 visualizes the meaning of the boundary layer thickness. Graphically it

corresponds to the interception of the concentration gradient at the water surface and the concentration in the water bulk.
The definition of the transfer velocity (equation 2.32) and the definition of the boundary layer thickness (equation 2.33) can be used to define a characteristic time scale t_* for the exchange process:

$$t_* = \frac{z_*}{k} \tag{2.34}$$

In a descriptive way, this time scale corresponds to the time that a tracer needs to penetrathe through the boundary layer.

Transfer Resistance

Boundary layers exist on the air and water side of the air-water interface. However, in general one of these layers is the dominant resistance for the transport. If the air or water sided boundary layer is more important for a specific tracer is given by its solubility α. Henry's law states that right at the air-water interface the air and water concentration of a trace gas are in equilibrium:

$$\alpha = \frac{c_{water}}{c_{air}}. \tag{2.35}$$

Tracers with high solubility, like heat or ammonia have their main resistance in the air sided boundary layer. On the other hand, low solubility results in a dominant resistance on the water side. Important gases with low solubility are e.g. CO_2 or N_2O. The resistance R is given by the inverse of the transfer velocity:

$$R = \frac{z_*}{D} \tag{2.36}$$

In analogy to electrical resistances, the air and water side resistances add up to the total resistance R_{total} for tracers when penetrating the air-water interface [71]. From the water sided perspective the total resistance is given by

$$R_{total} = \alpha R_{air} + R_{water} \tag{2.37}$$

Figure 2.1 gives an overview of different trace gases, their solubility and shows which side of the boundary layer dominates their transfer resistance. It should be mentioned here that for heat the air side resistance controls the air-water transfer process. However, with the measurement technique used within the scope of this thesis, only the water sided resistance is relevant, since heat is directly deposited

at the water surface and does not need to pass through air (c.f. section 3.3). Thus the transfer across the aqueous thermal boundary layer is investigated.

Friction Velocity

Equation 2.25 describes the flux density of momentum. This flux density corresponds to the shear stress τ at the water surface:

$$\tau = j_{momentum} \tag{2.38}$$

The shear stress can also be expressed as

$$u_* = \sqrt{\frac{|\tau|}{\rho}} \tag{2.39}$$

where the parameter u_* has the dimensions of a velocity and is thus called friction velocity. Directly at the water surface the shear stress in air τ_{air} equals the shear stress in water τ_{water}:

$$\tau_{air} = \tau_{water} \tag{2.40}$$

The air and water sided friction velocities can thus be converted into each other via the square root of the ratio of densities:

$$u_{*,water} = u_{*,air}\sqrt{\frac{\rho_{air}}{\rho_{water}}}. \tag{2.41}$$

Mean Square Slope

The mean square slope (mss) of the water surface is a statistical wave parameter used to characterize the roughness of the water surface. If x and y correspond to wind and cross-wind direction, mss can be defined as the sum of the variances of surface slopes $s_{x,y}$ in x and y direction, respectively:

$$mss = \overline{(s_x - \overline{s_x})^2} + \overline{(s_y - \overline{s_y})^2} \tag{2.42}$$

mss can vary significantly in the presence of surface active substances that especially dampen small capillary waves. This makes mss a very useful indicator for the presence and the magnitude of surface films (c.f. 2.4).

2.3. Models of Turbulent Gas Exchange

In this section four semi-empirical models will be outlined that are used to solve the transport problem for different boundary conditions. The first boundary condition is a rigid wall which corresponds to a smooth water surface. The other boundary condition is a free water surface. A schematic representation of the three of the presented models is shown in figure 2.3.

Film Model

The film model is the simplest model. It has already been presented in the 1920s [107]. It divides the transfer process into two zones. One well mixed turbulent bulk regime where turbulence dominates and one zone, the boundary layer, which is purely governed by molecular diffusion. At the end of the boundary layer, i.e. $z = z_*$ the regime will switch immediately from an entirely diffusive regime into a completely turbulent regime. This assumption however strongly oversimplifies the transfer process. Even smallest eddies introduce some residual turbulence into the boundary layer and affect the transport significantly. Still the simplicity of the model makes it useful for estimations of the lower level for the transfer velocity, given by pure diffusive transport. The model predicts a linear relationship of the transfer velocity and the Schmidt number:

$$k \propto Sc^{-1} \tag{2.43}$$

However the Schmidt number exponent is usually smaller than 1, which is another indicator that this model underestimates the transfer velocity [51].

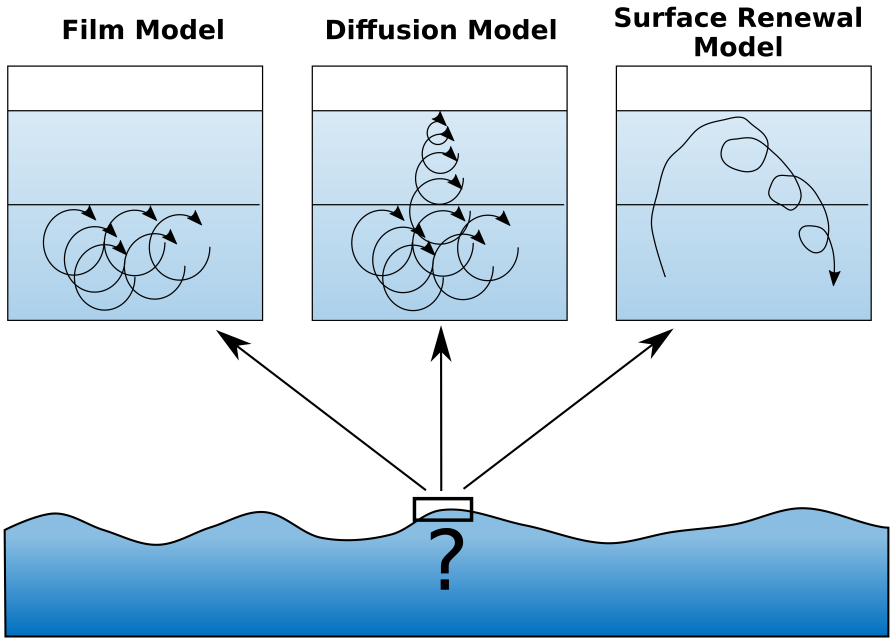

Figure 2.3.: Schematic representation of the film model, the diffusion model and the surface renewal model. Modified after Schimpf [91].

Diffusion Model

In the diffusion model it is assumed that the eddy size decreases continuously with decreasing distance to the water surface until the eddies vanish directly at the air-water interface. A common way to describe this behaviour mathematically is to use a depth dependent turbulent diffusion coefficient:

$$K(z) = \alpha z^m \tag{2.44}$$

Thus the turbulent diffusion coefficient will become larger, the larger the distance to the air-water interface becomes. The proportionality between the transfer velocity and the Schmidt number now is dependent on the boundary condition:

$$k \propto u_* Sc^{-1+\frac{1}{m}} \tag{2.45}$$

where $m = 2$ for a free water surface or $m = 3$ for a rigid wall [15, 111].
Another solution is provided by Deacon [21] who used a semi-empiric formula for the description of the turbulent diffusion coefficient based on velocity profiles

in turbulent flow as presented by Reichardt [88] at a solid wall. For the transfer resistance R Deacon finds

$$R = \frac{15.2}{u_*} Sc^{0.61} \qquad 0.6 < Sc < 10 \tag{2.46}$$

$$R = \frac{12.1}{u_*} Sc^{2/3} + \log(Sc) + 2.9 \qquad Sc > 10 \tag{2.47}$$

It is important here to emphasize that the Schmidt number exponent for heat, which has a Prandtl or Schmidt number of 7 at 20°C, for a smooth water surface is only 0.61 and not 2/3.

Surface Renewal Model

The surface renewal model assumes a boundary layer where molecular diffusion dominates the transport process. However in contrast to the film model additional eddies can penetrate the boundary layer and replace volume elements within the boundary layer. The original formulation of the surface renewal model [45] assumed periodic renewal events. Later the formulation was altered by Danckwerts and Hariott into statistically occurring renewal events [20, 42]. The renewal time τ depends on the water depth z [54] and is given by

$$\tau \propto z^{-p}. \tag{2.48}$$

The classical depth independent situation is described by $p = 0$. The transport equation in this case becomes

$$\frac{\partial^2 c}{\partial z^2} - \frac{c - c_{bulk}}{D\tau} = 0 \tag{2.49}$$

This leads exponential concentration profile:

$$c(z) = (c_{surface} - c_{bulk}) \exp\left(-\frac{z}{\sqrt{D\tau}}\right) + c_{bulk} \tag{2.50}$$

with the effective thickness [51]

$$z_* = \sqrt{D\tau} \tag{2.51}$$

The transfer velocity is then given by:

$$k = \sqrt{\frac{D}{\tau}} \tag{2.52}$$

The dependence of the Schmidt number can be derived from an analysis about the dimension of τ [79] and is given by

$$k = \frac{1}{\beta} u_* Sc^{-1/2} \tag{2.53}$$

with the dimensionless scaling factor β. This equation is valid for a free water surface. A more general formulation that also allows for a rigid wall is given by Jähne [55] and Csanady [18]:

$$k = \frac{1}{\beta_p} u_* Sc^{-1+\frac{1}{p+2}}. \tag{2.54}$$

For $p = 0$, the relation between the transfer velocity and the Schmidt number is

$$k \propto Sc^{-1/2}. \tag{2.55}$$

This case corresponds to a wavy water surface. For $p = 1$, one obtains

$$k \propto Sc^{-2/3}. \tag{2.56}$$

which corresponds to a smooth water surface.

Facet Model

All models described above show the same proportionality between the Schmidt number and the transfer velocity:

$$k \propto \frac{u_*}{\beta} Sc^{-n} \tag{2.57}$$

where n is the Schmidt number exponent and β the dimensionless momentum resistance.
The models explained so far consider two extreme cases: a free surface corresponding to $n = 1/2$ or a smooth water surface with $n = 2/3$. However experimental data suggests a gradual transition of the Schmidt number exponent

from 2/3 to 1/2 with increasing wind speed [58, 79, 62]. The facet model is an attempt to combine the models existing so far and to describe also situations where the water surface is not entirely rough or entirely flat, but where the water surface is governed by intermittency [57]. The model description assumes a certain fraction a_{rough} of the water surface to be rough and the rest of the water surface to be smooth. Those two types of area differ in the dimensionless momentum resistance β and the Schmidt number exponent n. The resulting transfer velocity is then given by

$$k = \left(1 - a_{rough}\right) \frac{u_*}{\beta_{smooth}} Sc^{-2/3} + a_{rough} \frac{u_*}{\beta_{rough}} Sc^{-1/2} \tag{2.58}$$

a_{rough} can be obtained from a parametrization based on the mean square slope of the water surface, which showed promising results [22, 62]. However a comparison of measured gas transfer velocities with transfer velocities predicted by the facet model showed deviations of up to nearly 300% [62].

2.4. The Influence of Surfactants

Surfactants are chemicals that lower the surface tension of water. The influence of surfactants on gas exchange has been studied a lot in the past. Significant reductions of gas transfer rates have been observed experimentally that are due to the presence of surface films [4]. Broecker et al. [13] found out, that for a given wind speed the addition of an artificial surfactant can reduce gas transfer velocities of up to 60%. The presence of a surfactant in the water becomes especially important in annular facilities, like the Aeolotron, as there is no cleaning procedure that removes the surface film from the water, but the film can stay on the water surface forever, as described by Jähne et al. [56].
There are two different types of surfactant: soluble surfactants and insoluble surfactants. Insoluble surfactants like oil accumulate at the water surface and can form thick spills [47]. They can act as an additional resistance by forming a condensed monolayer at the water surface [97]. However Liss [72] found that this effect is only relevant for low wind speeds in the field, as wind and waves can scatter the surface active material and thereby reduce its local concentration. Soluble films in contrast consist of a hydrophilic and a hydrophobic part. This leads to the formation of so called slicks at the water surface where the hydrophobic part sticks out of the water into the air and the hydrophilic part remains inside the water. In this way a monomolecular layer at the air-water

interface is formed [47].
The effect of surfactants on gas exchange is mainly an indirect one [30]. Surfactants alter the hydrodynamic processes at the air-water interface and thus reduce the amount of turbulence in the boundary layer. For example wave damping has been observed by Alpers and Hühnerfuss [1, 48]. Surface films also alter the sub-surface turbulence and reduce the rates of surface renewal [72, 40].

2.5. Heat Exchange

There are mainly three transport mechanisms for heat exchange within a fluid: convective transport, conductive transport and radiative transport.
Radiative transport is the basis for the measurement method used in this thesis and is described in detail in section 3. Radiative transport is present with all objects that have a temperature above the absolute zero temperature point of 0 K. All these objects both emit and absorb electromagnetic radiation that can be transported without the presence of matter, i.e. also in the vacuum.
Conductive transport in contrary needs matter to work. It is based on collisions of atoms and molecules due to their thermal motion. Molecules with a higher temperature have higher kinetic energy and conduction is aimed at equalizing these energy differences among molecules in a fluid.
Convection is based on macroscopic flow, that can carry molecules with it. In this way it also transports the thermal energy of these molecules. However convection is also possible without external flows, as it can also be caused by temperature differences. The temperature difference is accompanied by a difference in density and this causes a flow, which then carries molecules and their thermal energy to another location. A study of heat (and also gas exchange) for convective transport can be found e.g. in [67].

2.5.1. Heat Fluxes at the Water Surface

Three types of heat flux occur at the air-water interface: latent heat fluxes j_l, sensible heat fluxes j_s and radiative heat fluxes j_r. These heat fluxes cause deviations of the surface temperature from the temperature of the water bulk. A well known effect of this deviation is the so called cool skin of the ocean. Different heat fluxes across the water surface cause the surface temperature of the ocean to be cooler than the bulk temperature.

Latent heat fluxes describe the exchange of water between air and water as water vapour. Water molecules evaporate at the water surface and go into the air phase. This phase transition from the liquid to the gas phase needs energy, which is taken from the water and cools the water surface. Evaporation depends on the air humidity, the evaporation rate will be smaller for a more humid air space. For natural environments like on the ocean with air humidities between 60% to 80%, the latent heat flux $j_l \approx 140\ W/m^2$ [36].
Sensible heat fluxes occur when two objects with different temperature get into contact. They exchange thermal energy through the contacting interface. On the ocean the resulting sensible heat fluxes are in the order of -50 to $50\ W/m^2$ [91].
Radiative Heat Fluxes play an important role for measurements on the ocean. The temperature of the sky at night can be up to 65 K below the water temperature This causes a radiative heat flux of up to $200\ W/m^2$ that cools the ocean [90, 36]. However on sunny days the radiative balance might change into the other direction and thus the ocean can be heated radiatively by up to $500\ W/m^2$ [27].

2.5.2. Periodic Heat Flux Densities

All the model descriptions given in section 2.3 are valid for stationary flux densities only. The controlled flux technique, which is used for the measurements conducted within the scope of this thesis operates with periodically changing flux densities (see section 3.3). Detailed descriptions about the solutions for the film model, the diffusion model and the surface renewal model can be found in Jähne [55] and in Popp [85]. Here only the solutions should be presented. A discussion about the consequences of these solutions is given in section 3.3.2.
For the calculations dimensionless variables are used:

$$z_+ = \frac{z}{z_*} \tag{2.59}$$

$$t_+ = \frac{t}{\tau} \tag{2.60}$$

$$\omega_+ = \omega\tau \tag{2.61}$$

$$\overline{c_+} = \frac{\overline{c}}{\Delta\overline{c}} \tag{2.62}$$

where $\Delta\overline{c} = \overline{c}(0) - \overline{c}_{water,bulk}$ is the concentration difference between the concentration directly at the water surface and the concentration in the water bulk, τ is the settling time of the system and ω is the excitation frequency.

The basic concept behind the calculations is to solve the transport equations in the Fourier space. As analytical solutions only exist for the film model and for the surface renewal models only the solutions of these two models are listed here. The solution for the concentration directly at the water surface for the surface renewal model with a depth independent renewal rate, i.e. p=0 (c.f. section 2.3) is then given by the complex function

$$\overline{c_+}(0) = \frac{1}{\sqrt{1+i\omega_+}} \tag{2.63}$$

and the absolute of the concentration

$$|\overline{c_+}(0)| = \left(1+\omega_+^2\right)^{-1/4}. \tag{2.64}$$

The phase shift between the excitation signal, which is zero and the concentration response of the water surface is given by

$$\Delta\phi = 0 - \phi(0) = \arctan\left(\frac{\omega_+}{\sqrt{\sqrt{1+\omega_+^2}+1}}\right). \tag{2.65}$$

For the film model the concentration directly at the water surface is given as

$$\overline{c_+}(0) = \frac{\tanh\left(\sqrt{i\omega_+}\right)}{\sqrt{i\omega_+}}. \tag{2.66}$$

The absolute of the concentration at the water surface and thus of the amplitude is

$$|\overline{c_+}(0)| = \frac{\sqrt{\sinh^2\left(\frac{1}{2}\sqrt{2\omega_+}\right)+\sin^2\left(\frac{1}{2}\sqrt{2\omega_+}\right)}}{\sqrt{\omega_+\left(\sinh^2\left(\frac{1}{2}\sqrt{2\omega_+}\right)+\cos^2\left(\frac{1}{2}\sqrt{2\omega_+}\right)\right)}}. \tag{2.67}$$

The solution for the phase shift between excitation and response is given by

$$\Delta\phi = 0 - \phi(0) = \arctan\left(\frac{\sinh\left(\sqrt{2\omega_+}\right)-\sin\left(\sqrt{2\omega_+}\right)}{\sinh\left(\sqrt{2\omega_+}\right)+\sin\left(\sqrt{2\omega_+}\right)}\right). \tag{2.68}$$

2.5.3. Heat as a Proxy Tracer for Gas Exchange

A motivation for using heat as a proxy tracer for gas exchange is given in section 3.3. Here only the fundamental considerations behind this concept should be outlined.
As already shown in section 2.1.1, an analogy exists for molecular diffusion between gas transport and heat transport (c.f. equations 2.1 and 2.2). Generally heat conduction and molecular diffusion follow the same mechanisms [17]. In the context of gas exchange the correlation between gas exchange and momentum exchange is obvious. Momentum input into the water body introduces turbulence in the water which enhances gas transfer. Heat transfer is affected by this momentum input as well. Momentum, mass and heat transport are driven by concentration differences. However, while concentration difference for mass transfer really means a difference in concentration, for momentum it corresponds to a difference in momentum that causes a momentum flux and in the case of heat transport, it is an energy difference expressed as thermal energy. The concept of the transfer velocity, equation 2.32 is thus universally applicable. Equation 2.57 states that the transfer velocity is proportional to the Schmidt number to the power of the Schmidt number exponent. Thus, a scaling from the measured transfer velocity of a tracer a with known Schmidt number Sc_a to the transfer velocity of a tracer b with a known Schmidt number Sc_b only requires the knowledge of the Schmidt number exponent n. If n is known, the scaling of the transfer velocities can be done by

$$\frac{k_a}{k_b} = \left(\frac{Sc_a}{Sc_b}\right)^{-n}. \tag{2.69}$$

Complications arise from the fact, that the main resistance for heat transfer lies on the air side, while many gases are water side controlled (c.f. figure 2.1). The thermal boundary layer is thicker than the mass boundary layer by roughly a factor of 5 [91] due to the large difference between the Schmidt and Prandtl number between most gases and heat, e.g. $Pr = 7$ and $Sc_{CO_2} = 600$ at 20°C for fresh water. Additionally most gases have a much lower solubility in water than heat. Given these large differences in the tracer properties the question arises if a scaling for such extreme differences is possible. A further discussion about the feasibility of this scaling is given in sections 3.3 and 7.7.

3 Experimental Method

The experimental method that is used in this thesis is based on infrared thermography. The first part of this chapter is therefore dedicated to explain infrared thermography in general. Afterwards the important properties of water in the infrared wavelength regime are outlined. The history of the investigation of air-water heat transfer by thermography is briefly depicted, before a description of the controlled flux method, the key concept behind the measurements, is presented. Three different excitation schemes are explained. The last section of this chapter shows the need to heat an area and presents possible beam shaping solutions that are required to achieve a spatially homogeneous heating.

3.1. Thermography

All objects with a temperature above the absolute zero temperature of 0 K emit electromagnetic radiation due to molecular motion. This motion's kinetic energy is transformed into radiative energy. The wavelength of the radiation depends on the kinetic energy and therefore on the temperature of the object.
Not all objects are equally good emitters. The emissivity ϵ is a measure for the ability of an object to emit radiation. The maximal emittance $\epsilon = 1$ occurs with a so called black body. Good emitters are in general also good absorbers [24]. Thus, an ideal black body is an object that has an emissivity and absorption of 100%, which means that it emits as much radiation at a certain wavelength as it absorbs. The total spectral emittance of a perfect black body with an absolute temperature T can be described by the Planck distribution for black body radiation:

$$M_\lambda(T) = \frac{2hc^2}{\lambda^5} \frac{1}{\exp(\frac{hc}{k_B T \lambda}) - 1} \tag{3.1}$$

where $h = 6.6262 \cdot 10^{-34}$ Js is Planck's constant, $k_B = 1.3806 \cdot 10^{-23}$ J/K is the Boltzmann constant and $c = 2.9979 \cdot 10^{8}$ m/s is the speed of light in vacuum. The spectral emissivity of black bodies with three different temperatures is shown in figure 3.1.
There are two main consequences from equation 3.1:
1.) For a certain wavelength the emission increases with temperature. This means that spectra of objects with different temperatures have no crossings.
2.) The peak of the spectrum changes with temperature. The higher the temperature, the more radiation is emitted at shorter wavelengths.

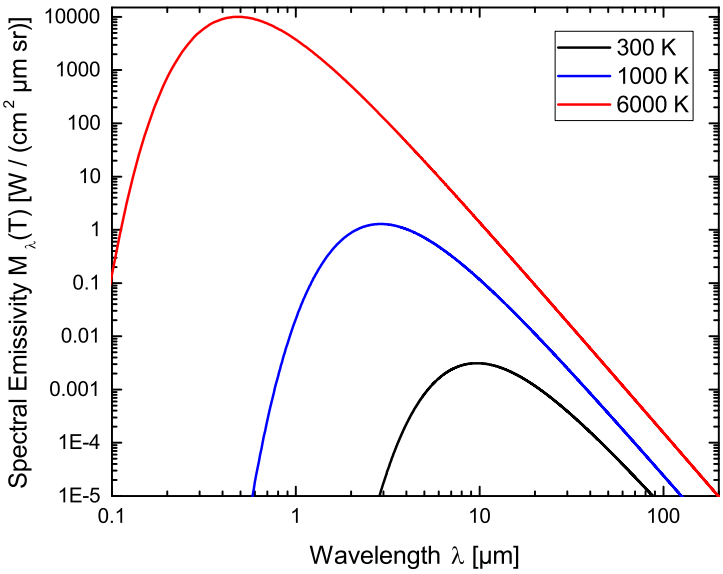

Figure 3.1.: Spectral emissivity of a black body for three different temperatures.

The peak wavelength of the spectral emittance can be calculated via Wien's displacement law:

$$\lambda_{max} \cdot T = 2897.8\ \mu m \cdot K \tag{3.2}$$

For example a black body at 300 K has a maximal emission at around 10 µm, while the sun with a surface temperature of approximately 6000 K has a maximal emission at 500 nm.
The total emission of a black body can be calculated with the Stefan-Boltzmann law:

$$M(T) = \int_0^\infty M_\lambda(T) d\lambda = \sigma T^4 \tag{3.3}$$

where $\sigma = 5.67 \cdot 10^{-12} \frac{W}{m^2 K^4}$ denotes the Stefan-Boltzmann constant.
Measuring the radiation in the infrared wavelength regime can be used to determine the temperature of an object. The application of this principle is called thermography.
Most objects however are no black bodies. Their emissivity is smaller than 1, which complicates the temperature measurement. Only a fraction of the outgoing light of such an object can be attributed to its own temperature, but there is also a radiative contribution, that is due to reflection of the surrounding at the object's surface. Under the assumption, that the surrounding has a constant temperature T_s the influence on the accuracy of a temperature measurement can be estimated after Jähne [50]. The total emission is then given by

$$M = \epsilon \sigma T^4 + (1 - \epsilon) \sigma T_s^4 \tag{3.4}$$

In the measured signal the recorded object will appear to have the temperature T'

$$\sigma T'^4 = \epsilon \sigma T^4 + (1 - \epsilon) \sigma T_s^4 \tag{3.5}$$

This can be rearranged:

$$T' = T \left(\epsilon + (1 - \epsilon) \frac{T_s^4}{T^4} \right)^{\frac{1}{4}} \tag{3.6}$$

For small temperature differences $\Delta T = T_s - T \ll T$ equation 3.6 reduces to

$$T' \approx \epsilon T + (1 - \epsilon) T_s \tag{3.7}$$

It follows

$$T' - T \approx (1 - \epsilon) \Delta T \tag{3.8}$$

From equation 3.8 it can be concluded that a deviation of only 1 % in ϵ causes an error in the measured temperature of 0.01 K per 1 K. For relative temperature measurements the effect is not as pronounced as for absolute temperature measurements:

$$\partial T' \approx \epsilon \partial T \tag{3.9}$$

if $(T_s - T) \ll T$. Thus the measured temperature difference appears to be a factor of ϵ smaller than the real temperature difference.

3.1.1. Different Types of Sensors

There are mainly two different types of sensors used to construct cameras for the infrared wavelength regime: thermal and quantum detectors.
The most relevant thermal detector that is used for cameras are **microbolometers**. Microbolometers make use of the fact that materials change their conductivity with temperature. For example the conductivity of a semi-conductor increases with increasing temperature. In a microbolometer the resistance is measured for each pixel. Through a calibration with an object of known temperature, the measured resistance can be matched to the corresponding temperature. Microbolometers are rather slow and need around 10 ms integration time for one image [101]. This integration time cannot be changed as it corresponds to the thermal time constant of the bolometer detector itself. The noise equivalent temperature (NETD) which is the measure for the temperature resolution of the IR camera is between 50 to 100 mK for modern bolometric camera systems [65]. An advantage of microbolometric cameras is, that they don't need cooling of their sensor. They only need a temperature stabilization and can therefore be kept compact in size.
Quantum detectors work like conventional semi-conductor based cameras for the visible wavelength regime. If the energy E_{ph} of an incoming photon is large enough, i.e.

$$E_{ph} = h\nu = \frac{hc}{\lambda} \tag{3.10}$$

then it can excite an electron from the valence band of the semi-conductor detector material of the camera sensor into the conduction band. This working principle is based on choosing a detector material with the right band gap energy E_{gap} for the corresponding wavelength regime, where radiation should be detected. The maximum wavelength that can be detected with a given semi-conductor is thus

$$\lambda_{max} = \frac{hc}{E_{gap}} \tag{3.11}$$

However in the IR wavelength regime the energies for the band gap of the semi-conductor are quite small. For example for a wavelength of 3 µm the energy of a photon is 0.4 eV. At 500 nm for comparison a photon has an energy of 2.5 eV. The band gap of silicon is 1.1 eV at room temperature [49]. This means that the widely used semi-conductor silicon and the corresponding well advanced technology to process silicon cannot be used for the IR regime. There are several semi-conductor materials, that are used for IR cameras, two of the most common ones are InAs/GaSb and GaAs/AlGaAs [50]. Depending on the chosen detector material, the IR imager is typically sensitive either to wavelengths between 3 µm

and 5 µm or to wavelengths between 8 µm and 12 µm.
If an electron is excited into the conduction band, it has to be kept separate from the positively charged hole in the conduction band. To detect the electron, there are mainly two possibilities [50]: collect the electron with an applied voltage or detect changes in the conductivity of the conduction band that are due to the presence of the electron in the conduction band.
Quantum detectors allow for shorter integration times as they convert incoming photons directly into a photo current. Modern camera systems can reach down to integration times of only 1 µs and they offer a higher thermal accuracy of up to 20 mK NETD [101].
The disadvantage of quantum detectors is, that they need to be cooled. The thermal energy at a temperature of $T = 300$ K is 25.9 mK. This corresponds to the peak in the Maxwell-Boltzmann distribution, which has a long tail towards higher energies. This means, that there is a significant amount of photons, whose energy is high enough to lift an electron from the valence band to the conduction band of the IR sensor. For a rough estimation [101], only the Boltzmann factor

$$W(E) \propto \exp\left(\frac{E}{k_B T}\right) = \exp\left(\frac{hc/\lambda}{k_B T}\right) \tag{3.12}$$

is considered. For a photon with wavelength $\lambda = 5$ µm, the probability of a thermal carrier excitation $W(E)$ is proportional to $4.2 \cdot 10^{-3}$. At liquid nitrogen temperature $T = 77$ K, however, it is only proportional to $3.8 \cdot 10^{-9}$. This means that by cooling the sensor and its immediate surrounding to 77 K, the free charge carrier concentration is reduced by six orders of magnitude and the background noise in the signal is dramatically reduced. Because of this reason, modern quantum detectors that operate at wavelengths between 3 µm and 12 µm are cooled thermoelectrically to 77 K by a Stirling cooler.
There are mainly two wavelength intervals that are used for IR cameras: 3-5 µm and 8-12 µm. The reason for these two wavelength intervals is, that they correspond to two windows in the absorption spectrum of air [50]. Thus within these two wavelength intervals, the radiation is only weakly absorbed by air.
For the application as a detector for the investigation of air-water heat transfer two aspects have to be considered when choosing one of those wavelength intervals: The advantage of the 8-12 µm wavelength interval is a smaller penetration depth in water (c.f. section 3.1.2) and a larger amount of photons at the relevant temperatures. However, for the wavelength interval from 3-5 µm the relative change in radiation with temperature is larger. The relative change in radiation

can be calculated as the derivative of equation 3.1 by temperature divided by the spectral excitance as given by equation 3.1:

$$\frac{dM_\lambda(T)/dT}{M_\lambda(T)} = \frac{\frac{hc}{k_B\lambda} \cdot \exp(\frac{hc}{k_BT\lambda})}{T^2\left(\exp(\frac{hc}{k_BT\lambda}) - 1\right)} \tag{3.13}$$

Figure 3.2 shows the different relative changes in the spectral excitance for the relevant wavelengths for thermographic applications. This means that a detector

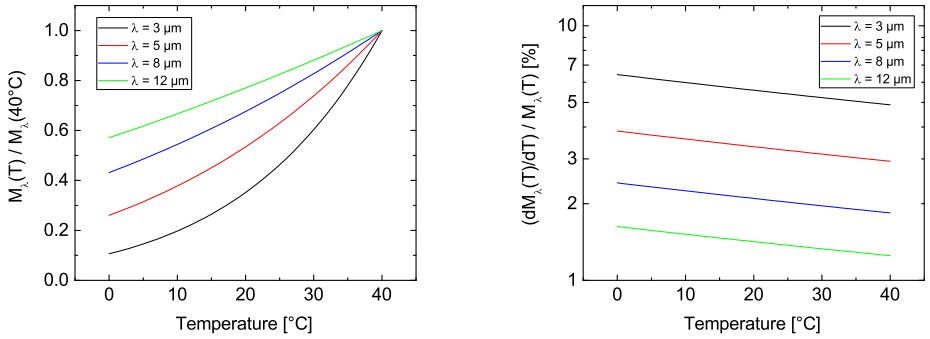

(a) **(b)**

Figure 3.2.: Relative change in the spectral radiance for different wavelengths with temperature. The relative change is higher for wavelengths between 3 µm and 5 µm compared to wavelengths between 10 µm and 12 µm. Modified after Jähne [50].

operating between 3 and 5 µm is more sensitive to temperature changes. Another reason for choosing the 3 to 5 µm wavelength regime for the application of active thermography at the air-water interface is to be able to separate the temperature signal of the water surface from reflections of the excitation beam of the CO_2 laser, that operates at 10.6 µm (c.f. section 4.4).

3.1.2. Properties of Water in the IR Regime

To describe the absorption and emission of radiation in water, the complex index of refraction N can be used:

$$N = n(\lambda) + ik(\lambda) \tag{3.14}$$

The real part $n(\lambda)$ represents the index of refraction used in geometrical optics. Applying Snellius law it can be used to determine the direction of propagation of an incoming ray in a medium with the refractive index n_1 with an inclination angle α into another medium with the refractive index n_2:

$$\frac{\sin(\alpha)}{\sin(\beta)} = \frac{n_2(\lambda)}{n_1(\lambda)} \tag{3.15}$$

β is the angle of inclination in the medium with n_2. For the transition from air to water, equation 3.15 simplifies with $n_1(\lambda) = n_{air}(\lambda) \approx 1$:

$$n_{water} = \frac{\sin(\alpha)}{\sin(\beta)} \tag{3.16}$$

The imaginary part of the complex index of refraction $k(\lambda)$ carries the information about the absorption of a certain medium. The absorption coefficient is given by

$$\beta(\lambda) = \frac{4\pi k(\lambda)}{\lambda} \tag{3.17}$$

The penetration depth $z_p(\lambda)$ follows

$$z_p(\lambda) = \frac{1}{\beta(\lambda)} = \frac{\lambda}{4\pi k(\lambda)} \tag{3.18}$$

The reflectivity of a certain material can be deduced from the complex index of refraction using Fresnel's equation (see for example [23]).
Measurements of the complex refractive index of water show that there is a significant wavelength dependence of the refractive index and the penetration depth. The penetration depth is shown in figure 3.3, where the data is taken from the measurements from Wieliczka et al. [108].
The optical properties of water come close to those of an ideal black body. The average emissivity of water is 0.97 [50]. Additionally, for emission angles smaller than 55° the water surface acts like a Lambertian radiator [43]. This means, that the water surface emits equal amounts of radiation into all directions within this angle. A schematic drawing of the radiance distribution of a perfect Lambertian radiator is shown in figure 3.4. Sea water only differs slightly in its optical properties from fresh water. The differences have been studied by Friedman [35]. The main difference is that there is a slight increase in the real part n of the complex refractive index for wavelengths smaller than 9 µm. However, the change in n is only 0.006 for a chlorinity of 19.0 ppt compared to absolute values

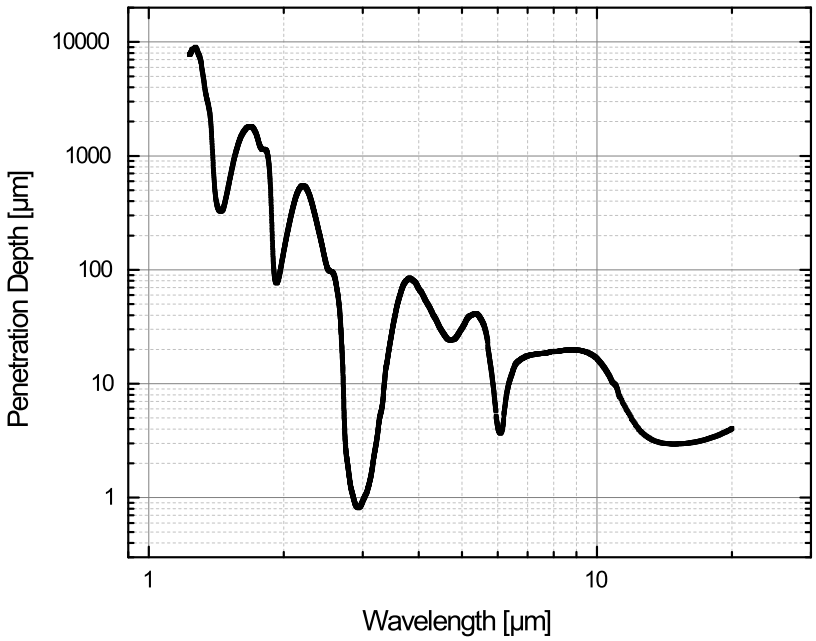

Figure 3.3.: Penetration depth in water for wavelengths between 1.2 µm and 20 µm. Data from Wieliczka et al. [108].

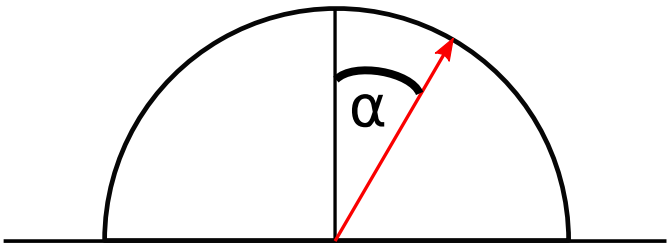

Figure 3.4.: Distribution of the radiance for a perfect Lambertian radiator. The radiance is independent of the angle between the emitting surface and the radiation.

of n around 1.3 in this wavelength interval. For higher salt concentrations the change in n needs to be extrapolated.

3.2. A Brief History of Thermography for the Investigation of Air-Water Heat Transfer

Heat transfer velocities (see chapter 2) across the aqueous boundary layer can be measured via thermography either in a passive or in an active measurement approach. When an active scheme is chosen, an external heat source is used to apply a controlled heat flux density at the water surface. In a passive scheme, the effect of surface cooling at the water surface due to evaporation is utilized.
Jähne and Libner [55, 69] were the first to use active thermography for the investigation of air-water heat transfer. Their measurements were based on the controlled flux method, that is described in detail in section 3.3. The experimental setup at that time consisted of an IR radiator and a chopper, that was needed to block the IR radiation periodically and to excite the water surface with certain heating frequencies. However, the chopper only allowed for excitation frequencies of up to 2 Hz. The temperature of the water surface was measured with an IR radiometer at one point of the water surface. A few years later the technological advancement had made IR cameras available as a tool for the investigation of air-water heat transfer. Haussecker [43] used an IR camera for his measurements together with a different measurement approach than Jähne in 1989 [55]. Haussecker used a 25 W CO_2 laser to heat spots on the water surface and tracked these spots and their temperature decay with an IR camera. A numerical analysis of the transport processes provided Haussecker with a formula that could be used to fit the temperature decay curve and to derive heat transfer velocities from the fit parameters.
Schimpf [91, 92] chose a passive measurement approach. An IR camera is used to record the temperature distribution at the water surface. This distribution consists of cooler areas at the water surface that are due to evaporative cooling and warmer areas, where water from the bulk is mixed with the evaporatively cooled surface water. A statistical analysis of the temperature distribution allows to estimate the heat transfer velocity. For Schimpf's measurements the latent heat flux still needed supplementary measurements to the IR images in order to estimate the latent heat flux. Garbe [39, 38, 36] introduced an alternative way to estimate heat transfer velocities solemnly from the recorded IR sequences without the need of additional measurements.
Haussecker's, Schimpf's and Garbe's measurement techniques share one drawback. They rely on model assumptions in the analysis of the measured data. This lead to some controversies [3, 6] when heat transfer velocities were used to infer gas transfer rates as described in section 2.5.3. Simultaneously measured heat and gas transfer velocities were not in accordance when scaled to the transfer

velocity of a gas with the same Schmidt number.
Due to these discrepancies the original measurement scheme from Jähne [55] came up again and was used by Popp [85] together with an improved experimental setup. To measure the water surface temperature, an IR camera was used and as a heat source a 100 W CO_2 laser was used. As lasers can be switched on and off very quickly, it was possible to use a broader frequency range for the excitation of the water surface. The laser beam was broadened with a cylindrical lens in one dimension. The laser line that is created in this was is positioned along the cross wind direction at the water surface. It is then moved forwards and backwards along the wind direction by means of a moving mirror. As a result a rectangular area on the water surface is heated. With this setup it could be shown, that without any model assumptions involved gas transfer velocities can be obtained from heat transfer velocities [78, 77].
The drawback in Popp's experimental setup, also used by Nagel [78, 77], was the inhomogeneity of the laser profile at the water surface. This is due to the initially Gaussian intensity profile of the laser beam, that can still be found in cross wind direction in the intensity of the rectangular laser intensity profile on the water surface. This inhomogeneity causes an inhomogeneous heat flux which affects the measurement accuracy. This problem has been solved by improvements in the experimental setup performed within the scope of this thesis. A detailed description of the beam shaping is given in section 3.4.1, section 4.1.3 and section 4.2.2.
Thermography can also be used to analyse footprints of near surface turbulence [95, 94]. Langmuir circulations have been studied via thermography by Marmorino et al. [73] and Zappa et al. use thermography to analyze microscale wave breaking [114, 115] to name just a few examples. However the analysis of turbulent structures at the air-water interface is not the subject of this thesis and no further information about this topic will be given here.

3.3. The Controlled Flux Method

The controlled flux method inverts the measurement principle of the commonly used mass balance methods, that are utilized for gas transfer velocity measurements. For the mass balance method, a certain amount of a trace gas or of several trace gases is added into the air or water phase. This causes a concentration difference between the air and water phase, which leads to a mass flux density

that is directed to balance the concentration difference according to Henry's law:

$$c_{water} = \alpha c_{air} \tag{3.19}$$

where α is the solubility of a certain tracer.
By monitoring concentration changes of the gas of interest over time, it is possible to derive the gas transfer velocity from the concentration gradient. For mass balance methods, as they are commonly implemented, this means, that the initial concentration difference is controlled.
The controlled flux method however controls the flux density at the water surface instead of the initial concentration difference. The knowledge about the transfer velocity is then gained from measuring concentration changes that are driven by the applied flux density.
This approach yields two big advantages: firstly, the control of a local flux density on the water surface clearly separates the area of interest where the exchange is stimulated from the surrounding environment, where no flux density is applied. It is therefore possible to conduct local measurements, which is a prerequisite for doing measurements in an open environmental surrounding like on the ocean. In such an environment mass balance methods are difficult, as already outlined in the introduction (c.f. section 1). If a certain gas is put e.g. into the air space over the ocean, then the concentration will decrease with time, but it is not clear, to what extend the decrease in concentration can be attributed to the exchange of gas between the atmosphere and the ocean and what amount of gas has simply been spread over a larger air volume by wind. There are ways to correct for this, for example in a dual tracer approach the concentration ratio of two gases is monitored instead of the absolute concentration [105].
However, the measurement speed for such a dual tracer experiment is limited by the settling time of the two trace gases, which typically leads to measurement times of at least several hours [40]. The consequence is, that the boundary conditions are very likely to change during such a long measurement time and the estimated exchange velocity will be an average over the different boundary conditions. The controlled flux method in contrary is a very fast measurement technique. Theoretically, transfer velocities can be obtained within a few seconds with such a technique. However, in a real experiment a certain degree of statistics has to be reached which leads to a minimum measurement duration between 5 minutes to one hour, depending on the chosen measurement scheme. More details and a discussion about the measurement time is given in section 7.1.3.
The key to the controlled flux method, is the ability to control the flux density at the water surface and to be able to change it quickly and with steep gradients. This is not possible for gases, but it can be done very well for heat. Two core components are needed to implement this measurement approach. The first

one is a heat source that provides the heat flux density at the water surface and that can be turned on and off quickly. The other core component is a device to monitor the temperature changes at the water surface. The basic operation principle is shown in figure 3.5. Jähne [55] used an IR radiator to apply the

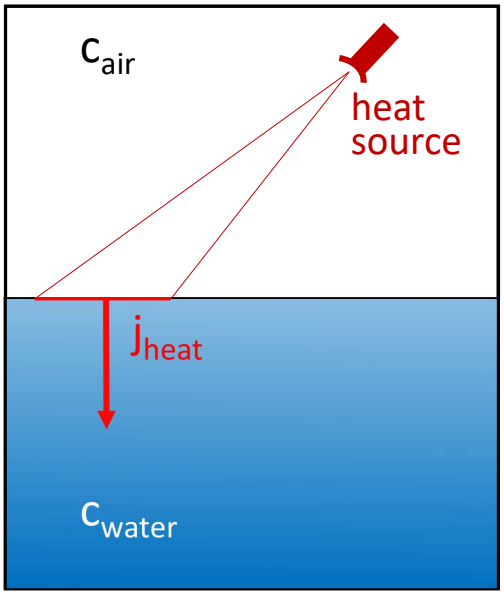

Figure 3.5.: Principle of the controlled flux technique. A heat source in the air space is used to apply a certain heat flux density at the water surface. The temperature detection device is not shown.

heat flux density and an IR thermometer to measure the temperature changes. Since Jähne's first experiments with the controlled flux technique there were several technological advancements. The heat flux density in the present setup is provided by one to two 100 W CO_2 lasers, depending on the desired heat flux density. Those lasers can be switched on and off with frequencies up to 1 kHz. The temperature measurement at the water surface is nowadays done by an IR camera that has a thermal resolution of 20 mK. The latter device is not just a precise thermometer, but it is also a thermometer with a high spatial resolution. The exact resolution depends on the chosen optics, however it is in the order of 0.5 mm to 1.5 mm. More details about the technical components of the actual experimental setup can be found in chapter 4.
In the following sections, the different measurement schemes are described.

3.3.1. ΔT Method

The simplest method from a physical point of view to determine the heat transfer velocity k_{heat} is to use equation 2.32, where only the concentration difference has to be changed to the thermal energy difference given by $\rho c_p \Delta T$ (c.f. section 2.2):

$$k_{heat} = \frac{j_{heat}}{\rho c_p \Delta T} \tag{3.20}$$

The density of water ρ and the heat capacity c_p of water are known and the heat flux density j_{heat} is given by the laser power P_{laser} and the size A_{heated} of the heated area

$$j_{heat} = \frac{P_{laser}}{A_{heated}} \tag{3.21}$$

This means that the only unknown variable in equation 3.20 is the temperature difference ΔT. ΔT however can be measured very well with an IR camera.
One problem of the present setup is, that the size of the heated area A_{heated} changes with the elevation of the water surface due to waves. This is described in detail in section 4.1.3. Another problem is, that the used optical components (see section 4) are not perfect, which means that not all of the laser's output power reaches the water surface. To quantify this loss of energy is difficult. However there is another way to determine the mean heat flux density at the water surface from the measurement directly. If the laser modulation frequency is high enough, then the transport of heat is dominated by molecular diffusion [69]. This means that the heat flux density can be determined by

$$j_{heat} = \rho c_p \Delta T \sqrt{D\omega} \tag{3.22}$$

where D is the diffusion constant of heat in water, $D = 0.0014 \frac{cm^2}{s}$ [53] and ω is given by $2\pi\nu$ with ν the applied modulation frequency of the laser.
In conclusion the heat transfer velocity can be determined by measuring the temperature difference at the water surface and by either directly measuring the heat flux density or by estimating it from the laser power and the size of the heated area.
The temperature difference can be measured with a static heat flux, meaning the laser is constantly switched on. However, it is easier to extract the temperature difference from a time series through a Fourier analysis. To do this, a very low excitation frequency is applied to estimate ΔT. This frequency ν_{low} must be small enough, so that

$$\frac{1}{2} \cdot \frac{1}{\nu_{low}} > \frac{L_{heated}}{\nu_{drift}} \tag{3.23}$$

where L_{heated} is the length of the heated area in wind direction and v_{drift} is the surface drift velocity. This means, that a water element should have enough time to travel completely through the heated area on the water surface in wind direction within the half period of the laser excitation cycle where the laser is switched on. Then, the same information can be gained from this periodic excitation as from the static case with a laser that is constantly switched on.

3.3.2. Amplitude Damping Method

The original measurement from Jähne [55] introduced the amplitude damping method. This is a kind of lock-in thermography, a concept that is well known in system theory. An application is for example the non destructive testing of metals and composite materials [101]. The conceptual idea is to stimulate an unknown system with different excitation frequencies and to monitor its response. This method can e.g. be used to test an electronic circuit. An advantage of this approach is, that the response of the system can be filtered from the output signal very well by a Fourier transformation, as the excitation frequency is known. This is e.g. used for non destructive material testing, where an object is periodically heated and the temperature changes and phase shifts from the excitation of the object are recorded with an IR camera. Then only temperature changes and phase shifts at the excitation frequency need to be taken into account, which makes the measurement more robust against other heat sources in the surrounding area.
The same principle applies to the measurement of the heat transfer velocity across the aqueous boundary layer. A consecutive set of frequencies is applied to modulate the laser and thus the water surface is excited with different periodically varying heat flux densities. The temperature changes that are caused by these excitations are monitored with an IR camera. The recorded temperature data is analysed in the Fourier domain.

Amplitude Analysis

The analysis of the temperature amplitudes provides the information needed to estimate the heat transfer velocity. For a periodic heating frequency two cases have to be considered: firstly the excitation frequency might be low enough for the water surface to reach a stable temperature equilibrium. At this equilibrium state the incoming energy into the system that is provided by the laser is balanced by the transport of heat down into the bulk water. The second possibility is, that

the frequency is too high for the water surface to reach this thermal equilibrium. The two cases are visualized in figure 3.6. If the laser is turned on, the water will

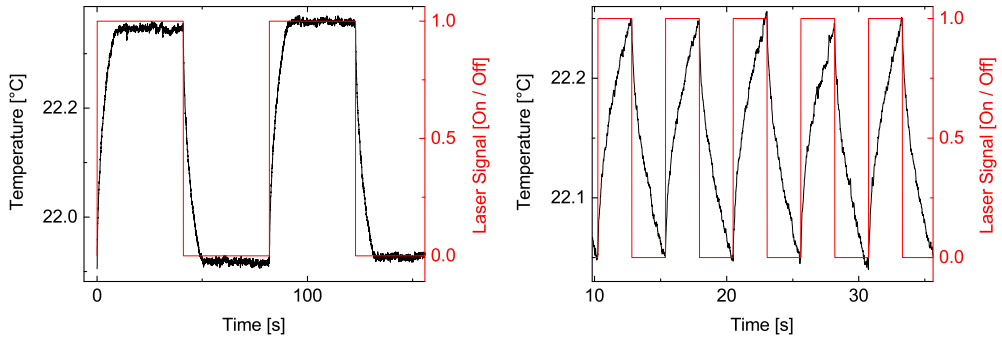

(a) **(b)**

Figure 3.6.: Comparison of a low and a high excitation frequency. For a low excitation frequency (a) the temperature response of the water surface can follow the excitation signal and reaches a stable temperature level. For a high excitation frequency (b) the water surface cannot reach a stable temperature level.

start to heat and at the same time the transfer of heat down into the bulk water through the boundary layer will start. The water will continue to heat, until at some point an energetic equilibrium between the incoming energy from the laser and the energy that is transported into the bulk water as heat, is reached. If the laser's modulation frequency is high, then the time is not sufficient to reach this equilibrium, but the laser will already be switched off before the water surface has fully heated to the equilibrium state. If the temperature amplitudes that are measured for a high and for a low frequency are compared, the amplitude that corresponds to the high frequency will be smaller, i.e. this amplitude appears as if it was damped. Therefore this method is called amplitude damping method. By applying many frequencies, from very low frequencies to high frequencies, it is possible to detect the frequency, where the damping starts. The principle is shown in figure 3.7. At the critical frequency ω_c where the damping starts, the following equation holds:

$$\omega_c \cdot \tau = 1 \tag{3.24}$$

The physical meaning of equation 3.24 is, that at the critical frequency there is just enough time for heat to penetrate from the surface through the boundary layer within one time period. This is the so called settling time τ of the system.

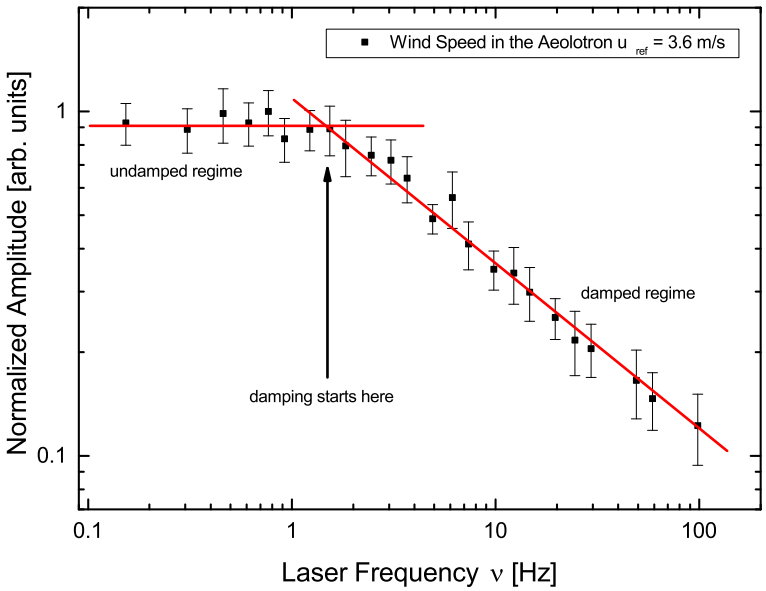

Figure 3.7.: Amplitude behaviour for different excitation frequencies. From a critical frequency onwards, the temperature response of the water surface is increasingly damped, as the excitation frequency increases further.

From the settling time of the system and the knowledge about the diffusion constant D of heat in water the transfer velocity can be derived:

$$k_{heat} = \sqrt{\frac{D}{\tau}} \tag{3.25}$$

There are different models for heat and gas exchange, respectively (c.f. section 2.3). Calculating the behaviour of the exchange process for a periodically varying heat flux density for three given models has been done by Jähne [55] and can also be found in Popp [85]. These calculations provide model functions for the amplitude behaviour of the air-water interface system for periodic excitations. However, the three models used by Jähne (the film model, the surface renewal model and the turbulent diffusion model) only differ around the critical frequency in their amplitude damping behaviour. A comparison of the surface renewal and the film model and their amplitude damping behaviour can be seen in figure 3.8. A lot of frequencies are needed for a measurement to make sure that the frequency region around the critical frequency, where the damping starts, is well covered and a high thermal resolution is required to distinguish even

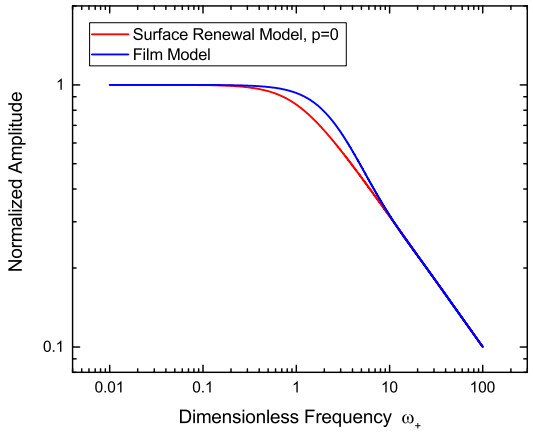

Figure 3.8.: Amplitude behaviour for different excitation frequencies as predicted by the surface renewal and the film model (c.f. section 2.3).

the smallest temperature changes to allow for a comparison of the calculated curves with the measured data. These circumstances make this approach very challenging and time consuming for an experiment. Thus this way of differentiating different models has not been pursued for the measurements done within this thesis.
There is, however, also an advantage if the models cannot be separated with the given experimental precision: as the models cannot be separated, any of them can be chosen to derive the settling time τ by means of a fit to the measured data. For the analysis of the data gained during this thesis, the surface renewal model has been chosen for this purpose, with the corresponding equation for the amplitude behaviour (c.f. equation 2.64):

$$c(\omega) = c_0 \cdot (1 + (\omega\tau)^2)^{-\frac{1}{4}} \tag{3.26}$$

Phase Analysis

The phase shift between the excitation signal and the temperature response of the water surface can be used to differentiate between the different models for heat and gas exchange. In contrast to the calculated curves for the amplitude behaviour, the calculated curves for the phase shift not only differ at the critical frequency, but also for any frequency below the critical frequency. In this low frequency regime the model predictions have a different slope in a logarithmic

plot. The calculated curves are shown in figure 3.9. The differences between

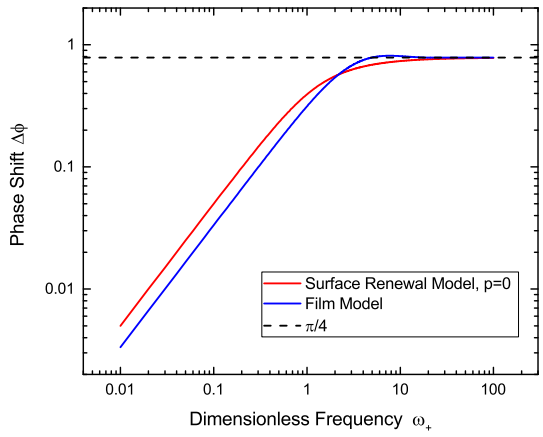

Figure 3.9.: Phase shift between the excitation signal and the response of the water surface for different excitation frequencies as given by the surface renewal and the film model (see section 2.3).

the model curves are obviously much more pronounced for the phases than for the amplitudes, so that here a comparison between different models and the measured data is feasible.

3.3.3. Multifrequency Excitation - Towards Faster Measurements

In section 3.3.1 a description how heat transfer velocities can be derived from a measurement that consists of only two frequencies is given. One low frequency is needed to get the temperature difference in thermal equilibrium ΔT and one high frequency is used to estimate the heat flux density j_{heat} at the water surface. As only two frequencies are required, this measurement scheme is already a fast scheme compared to the amplitude damping method that is composed of repetitive measurements with many varying frequencies. However, as those two frequencies are measured consecutively the measurement might be biased if the boundary conditions change during the measurement time. To avoid this, a new approach was tested within this thesis, where two frequencies are not measured consecutively, but at the same time by a multifrequency excitation. A convolution in the frequency domain corresponds to a multiplication in the time

domain. Thus the two modulation patterns for the laser signal can simply be multiplied to achieve the new excitation. This is visualized in figure 3.10.

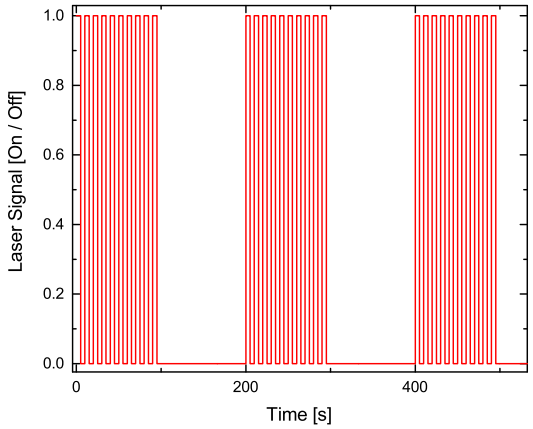

Figure 3.10.: The resulting excitation signal that results from the multiplication of two separate signals with different frequencies.

Having two different excitation frequencies at the same time, the power of the laser is distributed to those two frequencies and their higher harmonics. This means that there is less energy available per excitation frequency, compared to a measurement scheme, where only one excitation frequency is probed at a time. An attempt to compensate for this effect has been made by changing the duty cycle of the two excitation frequencies. However the energy for the two desired excitation frequencies could not be increased in this way. Figure 3.11 shows an excitation frequency of $\nu = 25$ Hz with different duty cycles of 25%, 50% and 75%. It can clearly be seen from the spectra in figure 3.11 (b), (d) and (f) that by increasing the duty cycle, energy is transferred to the first harmonic of the excitation signal and the signal of the ground excitation frequency is reduced. The same holds true for decreasing the duty cycle of the excitation frequency.
Figure 3.12 shows multifrequency excitation signals with a duty cycle of 50% for the slow frequency of $\nu = 0.049$ Hz and duty cycles of 50% and 75% for the higher frequency with $\nu = 25$ Hz. As for the case with only one single excitation frequency, the increase of the duty cycle transfers energy to the first harmonic of the excitation frequency. However, by increasing the duty cycle of the 25 Hz excitation frequency, also the amplitude of the 0.049 Hz signal is increased. Unfortunately the signal at 25 Hz itself is significantly reduced.
Figure 3.13 shows the excitation signals and spectra for a duty cycle of 75% for the 0.049 Hz frequency and duty cycles of 50% and 75% for the 25 Hz frequency.

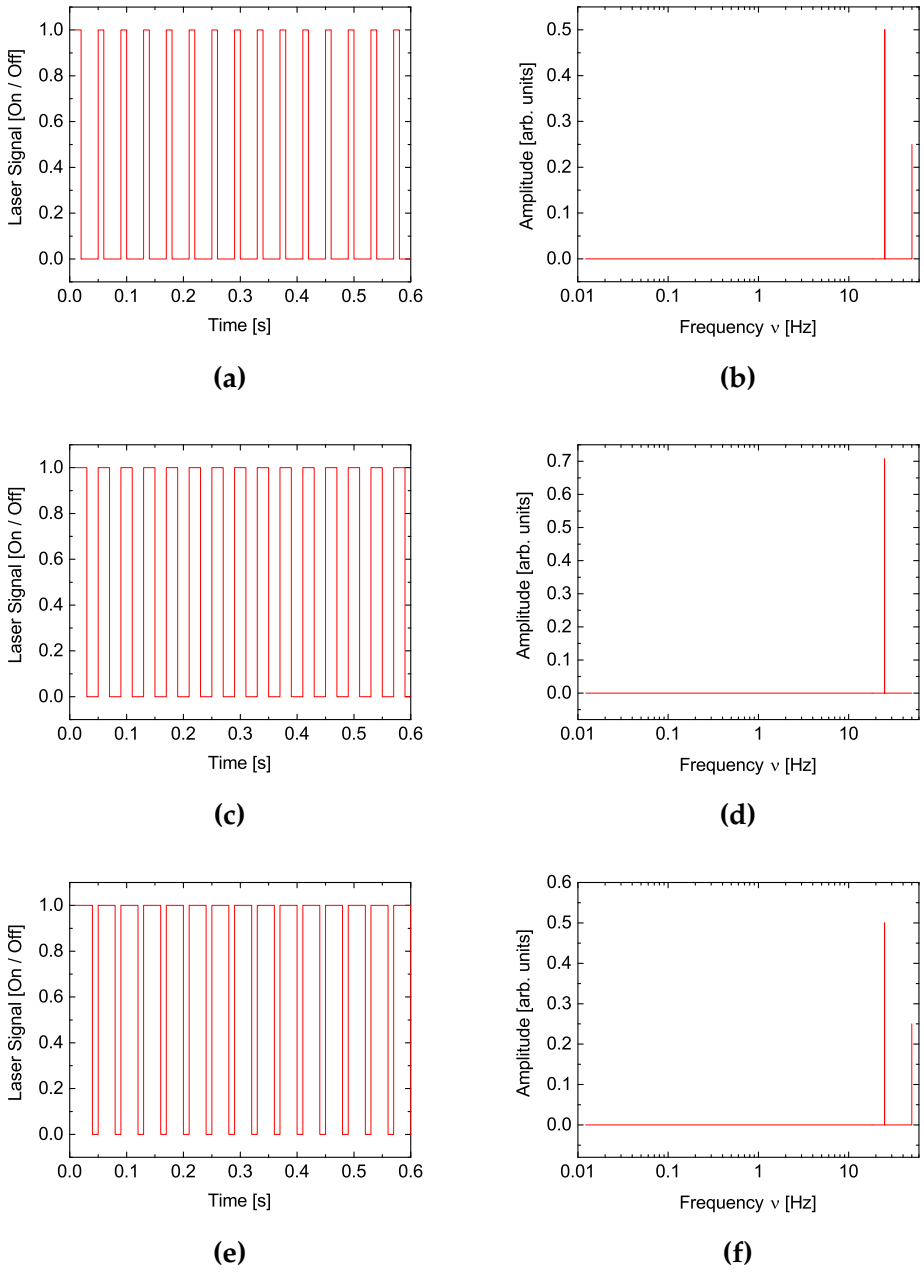

Figure 3.11.: Excitation frequency of 25 Hz with different duty cycles. (a), (c) and (e) show the time series of the excitation signal for duty cycles of 25%, 50% and 75%, respectively. (b), (d) and (f) show the corresponding spectra. It can be seen that most energy is transferred into the ground excitation frequency for a duty cycle of 50%. For 25% and 75% duty cycle the amplitude of the ground excitation frequency is reduced and its first harmonic appears.

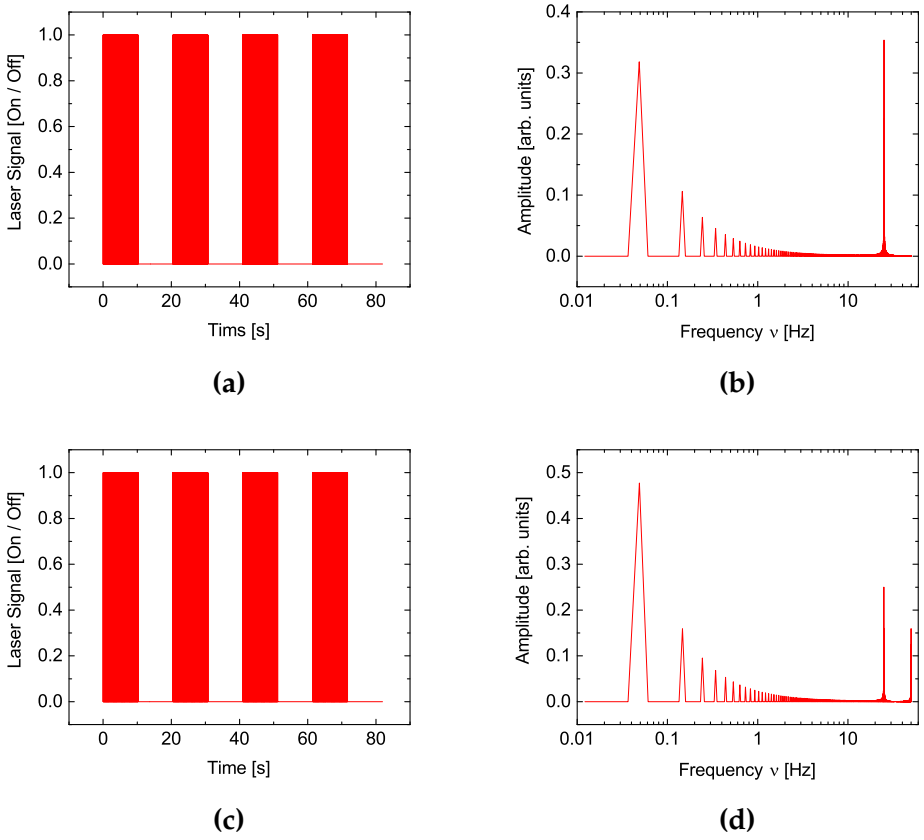

Figure 3.12.: Exemplary multifrequency excitation scheme. The two frequencies used are 0.049 Hz and 25 Hz. (a) and (c) show the time series of the excitation pattern and (b) and (d) show the corresponding spectra. The duty cycle for the excitation frequency with 0.049 Hz is 50% in both cases. However the 25 Hz frequency has a duty cycle of 50% in (a) and (b) and a duty cycle of 75% is (c) and (d).

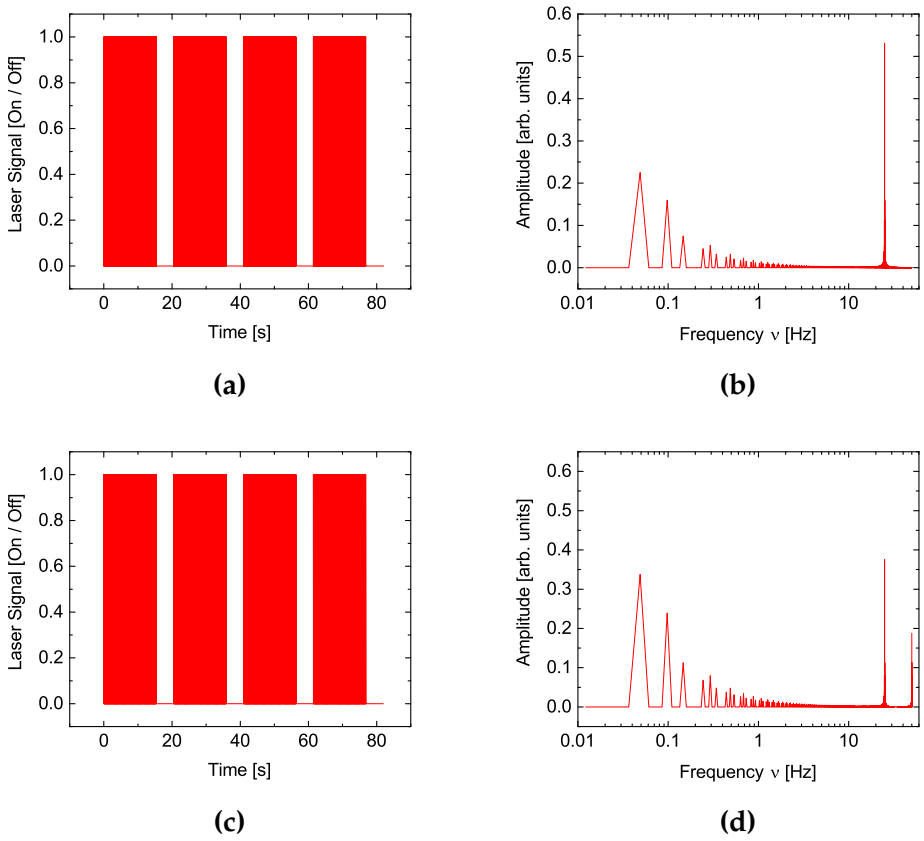

Figure 3.13.: The same case as in figure 3.12, only that the duty cycle of the excitation frequency with 0.049 Hz is now 75% in the signals shown.

The observations are basically the same as for the cases shown in figure 3.12. The increase of duty cycle of the 25 Hz frequency increases the frequency at 0.049 Hz and the first harmonic of the 25 Hz frequency at 50 Hz appears. The amplitude of the 25 Hz frequency itself is reduced again. However the increase in duty cycle for the 0.049 Hz frequency also comes along with the appearance of the first harmonic at 0.098 Hz. If both, the 0.049 Hz and the 25 Hz frequency have duty cycles of 75% the signal is very similar to the case where both frequencies have duty cycles of 50%, but with the difference that both frequencies have first harmonics in the spectra. The amplitudes of the ground frequencies are both increased by 6%. For the measurements the excitation patterns with duty cycles of 50% and 75% for both frequencies have therefore been tested. The results of the measurements are discussed in section 7.1.3.

3.4. Heating an Area

For all the measurement schemes described in the previous sections, it is necessary to heat an area on the water surface and not just a spot. There are two reasons for this: the first one is to reduce the influence of horizontal diffusion onto the measurement. If a dot is heated on the water surface, the heat will diffuse into all directions. The transport upwards into the air space can be neglected due to the large solubility of heat in water (c.f. figure 2.1). However the exchange process of interest is the transport of heat down into the bulk water and thus horizontal diffusion disturbs the measurement. By homogeneously heating an area, horizontal diffusion is limited to the borders of this area, if all the water within this area has the same temperature. Thus it becomes possible to avoid horizontal diffusion by only analysing an inner part of the heated area.
The second reason for heating an area is, that it takes a certain time for the water to heat up until a stable temperature is reached. At this equilibrium temperature the incoming energy from the laser equals the energy, that is transported down into the bulk water as heat. Figure 3.14 visualizes the heating process when surface water enters the area that is illuminated by the laser and when it is pushed through this illuminated area by the surface drift. Once a surface water

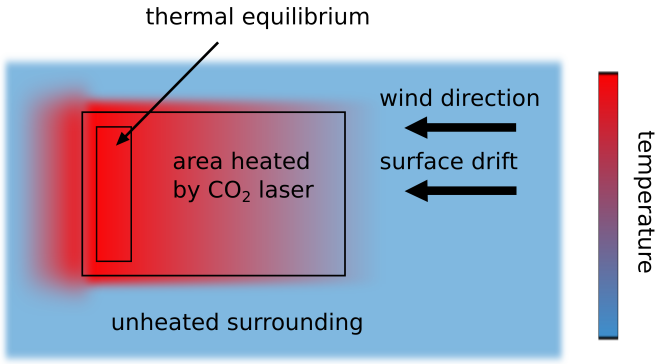

Figure 3.14.: Top view on the heating process of the surface water as it flows through the area that is heated by the IR laser. Behind the area heated by the laser the water starts to cool down again. Note that at the borders of the heated area horizontal diffusion takes place.

element enters the illuminated area it will start to heat up, but it will take some time to reach the thermal equilibrium, described above. For the analysis of the measured data, the area that is indicated as "thermal equilibrium" in figure 3.14 is selected.
In order to have a homogeneous heat flux density at the water surface the laser

intensity profile needs to be homogeneous. To achieve this, diffractive optical elements (DOEs) are used. Diffractive beam homogenizers are discussed in section 3.4.1 and the exact models used are listed in section 4.5.

3.4.1. Beam Shaping

A large improvement for the measurements in this thesis was the use of diffractive optical elements (DOEs). These devices shape an incoming laser beam into any desired output profile based on diffraction. For this thesis diffractive beam homogenizers have been used that create a homogeneous square intensity profile from a Gaussian input laser beam. Two different diffractive beam homogenizers have been used in this thesis. Both models are listed in section 4.5.
"Beam shaping is the process of redistributing the irradiance and phase of a beam of optical radiation" [25]. For many scientific as well as industrial applications, e.g. material processing, lithography and medical applications, beam shaping is crucial. One of the most important applications of beam shaping is the conversion of a Gaussian laser beam profile into a flat top profile, i.e. a profile with spatially homogeneous intensity distribution. The simplest implementation to

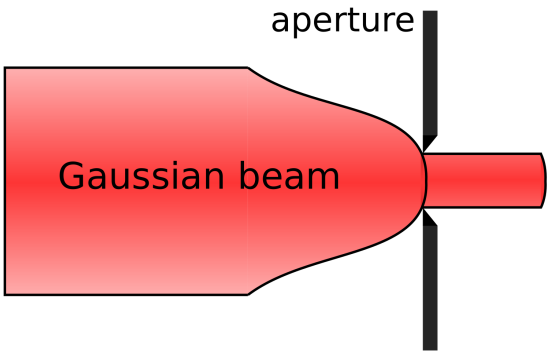

Figure 3.15.: Beam shaping with the use of an aperture. Only an inner fraction of the incoming Gaussian beam can pass the aperture. The intensity variation in the beam profile is thus minimized, although no perfectly homogeneous intensity profile can be achieved.

achieve a homogeneous intensity profile is to apply an aperture, as shown in figure 3.15. However as can directly be seen from the figure this approach causes high energy losses, as only a small fraction of the initial laser beam passes the aperture. In the case of high power applications such as material processing or heating the water surface with powerful 100 W to 1 kW CO_2 lasers, the aperture

approach also requires cooling of the aperture.
Lossless beam shaping was introduces in the mid-1960s [32] which proposed the use of either two plano-aspheric lenses or the use of a pair of selectively aberrated lens systems. Today, there are three major categories that distinguish beam shapers by their operating principle: aperturing systems, field mappers and beam integrators. The diffractive beam homogenizers are field mappers. Figure 3.16 shows the principal setup used for beam shaping with such a device.

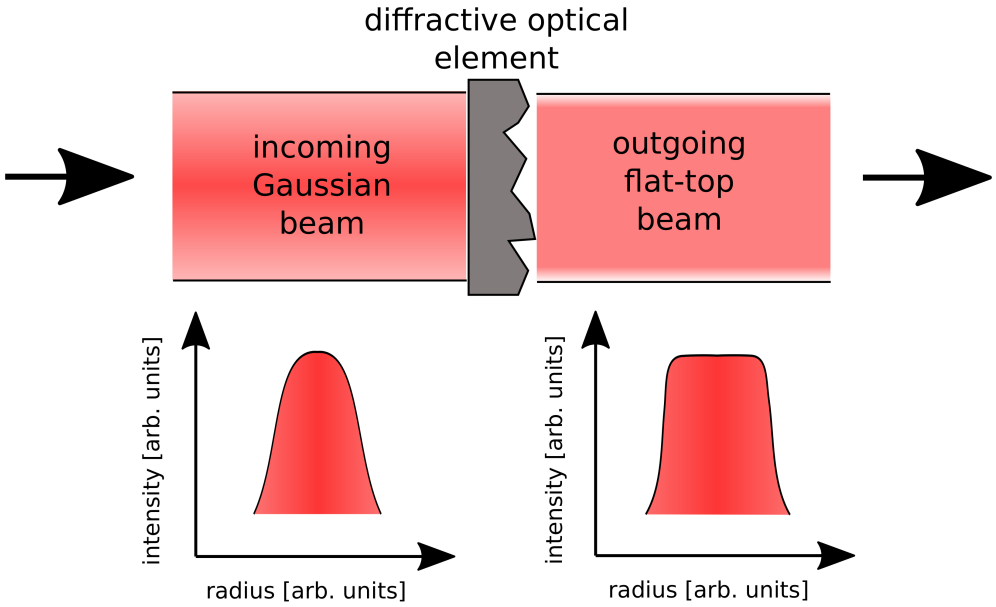

Figure 3.16.: Schematic representation of the beam shaping process with a diffractive optical element.

An input beam is modified by a beam shaping element, in this case a diffractive optical element. This element can either work as a field mapper or as a beam integrator.
The concept of field mapping applies to both lossless beam shaping devices. The following mathematical description is based on the overview paper concerning beam shaping by Dickey [25]. The basic field mapping problem can be formulated by the Fresnel integral as

$$U(x_0, y_0) = \frac{\exp(ikz)}{i\lambda z} \int\int U(x_1, y_1) \exp\left(\psi(x_1, y_1)\right) \cdot \exp\left(\frac{ik}{2z}\left[(x_0 - x_1)^2 - (y_0 - y_1)^2\right]\right) dx_1 dy_1 \tag{3.27}$$

with $k = 2\pi/\lambda$ and $U(x_1, y_1)$ the complex representation of the input beam, $\psi(x_1, y_1)$ the phase function that represents the lossless beam shaping element and $U(x_0, y_0)$ the shaped complex field in the output plane at distance z. If the last exponential in the integrand is expanded and the remaining quadratic phase function is included in the beam shaping element ψ, the beam shaping problem can be expressed as a Fourier transform:

$$U(x_0, y_0) = \frac{\exp(ikz)}{i\lambda z} \exp\left(x_0^2 + y_0^2\right) \int\int U(x_1, y_1) \exp \psi(x_1, y_1) \cdot \exp\left[-i\frac{2\pi}{\lambda z}(x_0 x_1 + y_0 y_1)\right] dx_1 dy_1. \tag{3.28}$$

Solving equation 3.28 corresponds to determining the phase function ψ for a simultaneously given magnitude of a function and of the function's Fourier transform.
The uncertainty principle of quantum mechanics acts as a constraint for the lower limit of the product of the root-mean-square width the root-mean-square bandwidth of a function:

$$\Delta_x \Delta_\nu \geqslant \frac{1}{4\pi} \tag{3.29}$$

From the uncertainty principle the parameter β can be derived for the problem of beam shaping:

$$\beta = C\frac{r_0 y_0}{zf} \tag{3.30}$$

with r_0, y_0 the half width of the input beam and output beam, respectively, and C a constant depending on the exact definition of the beam widths and f the focal length of the system. The size of β is crucial for obtaining a good solution to the beam shaping problem.
Different approaches to solving the beam shaping problem yield different sensitivities on alignment errors. Some designs are very sensitive to small misalignments like decentering the input beam by only 10% of its diameter. Also changes in the input beam diameter by only 10 % can affect the homogeneity of the output intensity distribution. Inclinations between the beam shaping element and the input beam also decrease the beam shaping element's performance and result in a decreased quality of the resulting output intensity. Some designs are also constructed to work at a specific working distance only and the output profile will change when the target is at another distance from the beam shaping element. As optical calibration for a field experiment is very demanding the beam shaping element for the active thermographic measurement should be as insensitive to misalignments as possible. On top of that a fixed working distance is not acceptable as the water surface is not rigid but moves up and down due to

wave modulation. The diffractive beam homogenizers listed in section 4.5 and discussed in section 7.1.1 were thus the beam shaping elements of choice for the present experiments.

Experimental Setup and Calibration

4

In this chapter the experimental setup is described. Most of the experiments were conducted at the annular wind-wave facility Aeolotron in Heidelberg. The first section therefore introduces this facility shortly and explains the location of the measurement devices needed for the thermographic measurements.
In June 2016 a measurement campaign was conducted at the large wind-wave facility Pytheas in Marseille, France. This facility in comparison to the Aeolotron has a linear geometry. The second section explains the experimental setup at the Marseille facility.
In the third section the properties of the infrared camera are discussed and the temperature calibration is presented.
The forth section then details the used infrared lasers, before in the last section the diffractive beam shaping devices are listed that have been used for the experiments.

4.1. The Aeolotron

The Aeolotron in Heidelberg is an annular wind-wave facility. A schematic representation of the facility is shown in figure 4.1. The Aeolotron is the largest operational wind-wave facility in the world. The inner diameter of the facility is 10 m and the channel with is approximately 60 cm. The water channel in the Aeolotron is typically filled up to a water level of 1 m which corresponds to a total water volume of 18 m^3. The air space then comprises 25 m^3 of air. The annular shape provides an unlimited distance for the interaction between the wind and the water. This distance is called fetch. In linear facilities waves cannot grow until they reach equilibrium for higher wind speeds, as the fetch distance is typically in the order of 30 m, which is not long enough to fully establish the

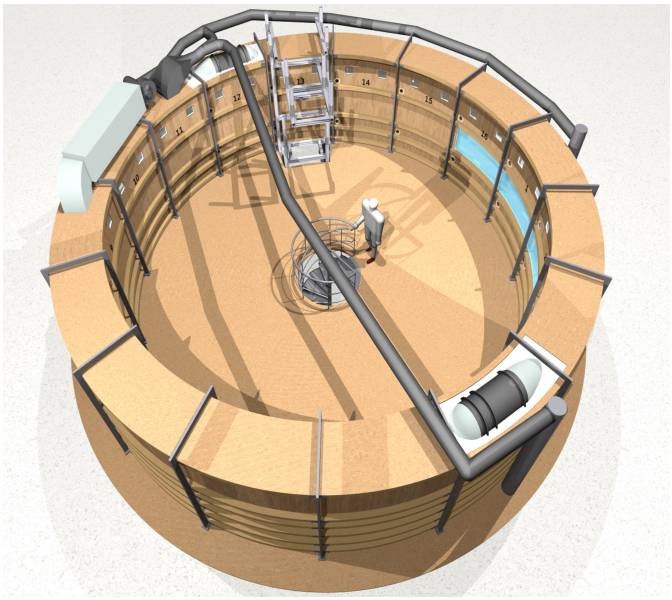

Figure 4.1.: Schematic representation of the Aeolotron. The inner diameter of the facility is 10 m. Figure taken from Krall [62].

wave field.
The wind in the Aeolotron is generated by two axial fans that are mounted on opposite sides of the facility. The maximum wind speed that can be achieved is 11.3 m/s. Due to the fact that the wind is generated locally at two distinct locations at the facility and due to the annular shape, there exist spatial inhomogeneities in both, the air and water flow [10].
An important feature of the Aeolotron for the thermographic measurements is, that the facility is thermally insulated. To reduce the influence of radiative heat exchange, the walls are covered with reflecting aluminium foil. Given these two properties of the Aeolotron, radiative heat fluxes and conductive heat fluxes can be neglected.
The Aeolotron is air tight, which is important for gas exchange measurements. Latent heat fluxes can be controlled in the Aeolotron by means of an air-condition device. If this device is not used, as is the case for the active thermographic measurements, the air humidity inside the Aeolotron will quickly reach 100% and latent heat fluxes also become negligible.
As can be seen in figure 4.2 the Aeolotron is divided into 16 segments. There is one section of the Aeolotron where all the optical measurement devices are located (section 13). The advantage of combining all optical measurements at one location is, that all gained information from one measurement can be compared directly to the other measurements. For example the measured wave slopes can

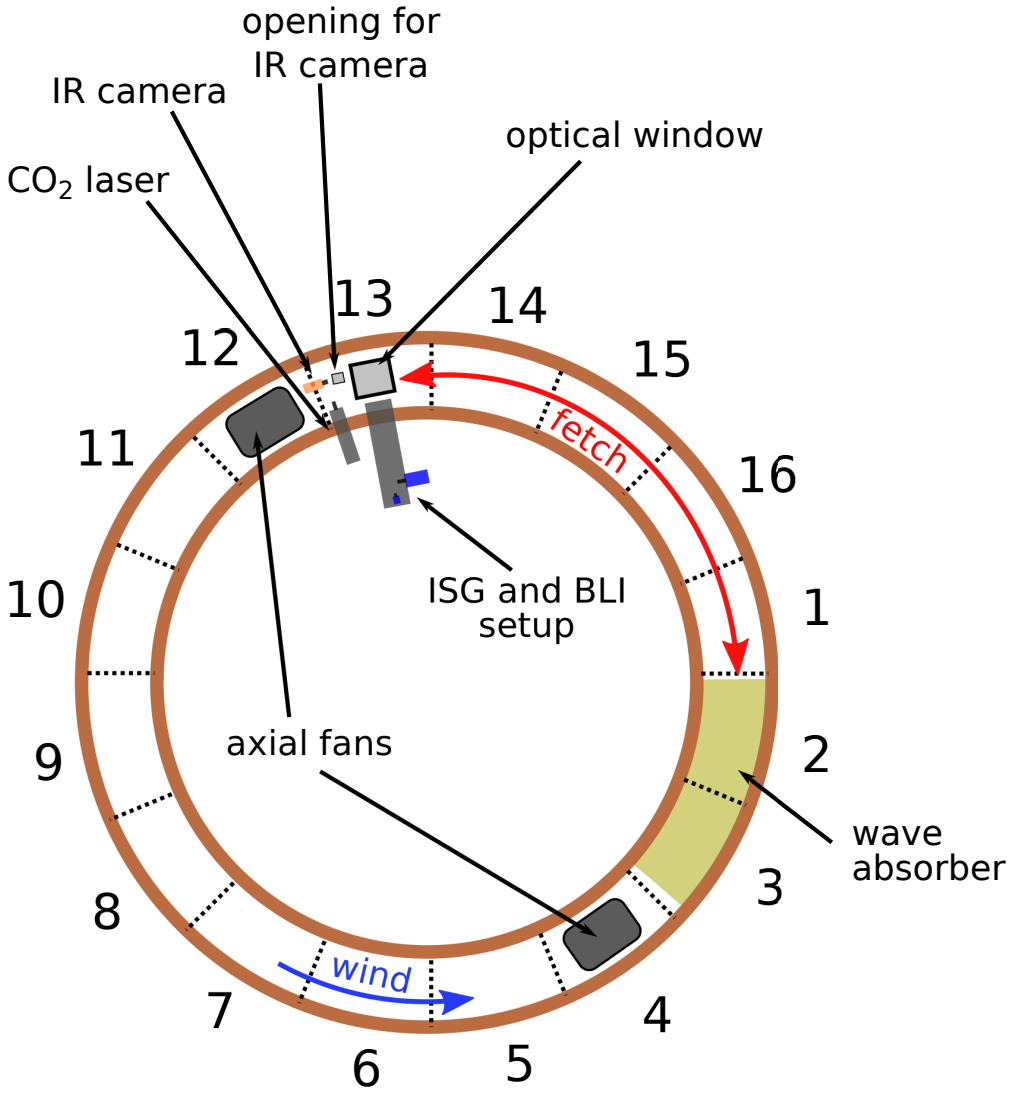

Figure 4.2.: Schematic representation of locations of the measurement instruments at the Aeolotron. All optical measurements take place at segment 13. This is also where the infrared camera and the CO_2 laser are located. For better clarity not all optics like mirrors etc. are included in the drawing.

directly be compared to the structures seen by the infrared camera and correlations between the two image types can be investigated.
At this optical section all cameras, except for the IR camera, observe the water surface through a glass window. For the wave imaging technique [61] and the boundary layer visualization technique [63], a telecentric setup is implemented, where the cameras look straight down onto the water surface and the elevation of the water surface does not change the size of the structures in the image. The wave slope measurement device used in parallel to the thermographic measurements of this thesis, the so called imaging slope gauge (ISG) is described in detail by Kiefhaber [61]. For some of the thermographic measurements, also the boundary layer imaging technique (BLI) was used in parallel. This technique allows for the visualization of turbulent structures in the boundary layer during gas exchange of ammonia. The technique is based on a fluorescent dye that is sensitive to changes in the pH values. The technique and the experimental implementation at the Aeolotron is described in detail by Kräuter [63].
For all measurements the wind has been measured at a reference position directly below the ceiling at segment 15 by a pitot tube and by an anemometer (Greisinger STS020). This is why the wind speed will also be called reference wind speed in the following sections. The bulk water velocity is measured at a height of approximately 50 cm above the bottom via an acoustic velocity sensor (Nobska MAVS-3). Additionally there are sensors for humidity, air and water temperature (Pt-100, Greisinger GMH 5530).

4.1.1. Fetch Variation

To investigate the influence of the fetch length, i.e. the interaction length between wind and water, on air-water heat exchange, a wave absorber has been designed and constructed for the Aeolotron, that can be moved around the annular water channel without having to open the air space. This was the work of a bachelor's thesis (see Kropp [64]). The wave absorber is a swimming object, that is roughly 3 m long, and consists of two main parts. One is made of a bubble foil and the other of a honey comb like structure, made of polyethylene. The open ends of the honey combs are oriented vertically on the water surface, so that they lie perpendicular to the direction of surface drift. The honey combs then redirect the momentum of the waves into the vertical direction and thereby absorb the energy from the waves and dampen the waves. A problem is the disturbance of the wind field at the honey combs. To minimize this effect, the honey combs should not stick out too high above the water surface.
To avoid reflections of small waves at the Lee side of the wave absorber, a bubble

foil is used. This foil dampens small waves effectively, as it provides a solid surface, comparable to a thick surface film. Additionally the foil prevents large waves from overflowing the homey comb like structure of the wave absorber. More details about the wave absorber can be found in Kropp [64].

Figure 4.3.: Pictures of the wave absorbed used in the Aeolotron. The left picture shows the wave absorber from the top, the middle picture shows the support structures on the bottom side, that are needed to make it more stiff and to maintain it from sinking to deep into the water. The right picture shows the wave absorber installed in the Aeolotron's water channel. Pictures taken from Kropp [64].

4.1.2. Setup at the Aeolotron

The experimental setup for the thermographic measurements at the Aeolotron is shown schematically in a side view in figure 4.4. Photos of the experimental setup at the Aeolotron can be seen in figure 4.5. For the thermographic measurements the combination of all optical experiments at one location described in section 4.1 has consequences for the experimental setup. Glass is not opaque in the infrared, the IR camera thus cannot use the same optical paths as the other cameras. This means, that the IR camera and the IR laser need additional separate openings in the ceiling of the Aeolotron. Unfortunately, these openings are located next to the normal glass window at the ceiling of the Aeolotron and thus to observe the same spot on the water surface, the IR camera needs to have an inclination of about 15°. A consequence of this inclination is, that the view of the camera is

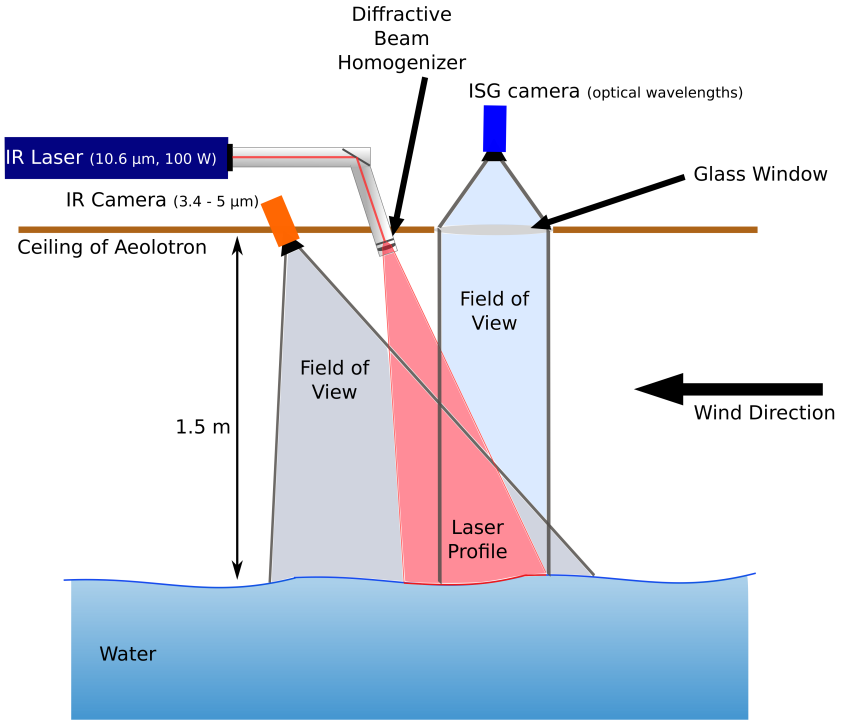

Figure 4.4.: Schematic representation experimental setup at the Aeolotron as seen from the side of the facility. The IR camera's field of view is chosen in a way, that the complete area that is heated by the laser can be observed, as well as the surrounding unheated water. The imaging slope gauge (ISG) measures at the same location as the IR camera.

slanted. This causes distortions in the image.
While slanting the IR camera also avoids the detection of reflections from the camera sensor that is cooled to 77 K, slanting the IR laser beam strongly affects the intensity distribution at the surface. The consequences of this inclination of the laser beam in the Aeolotron are discussed in detail in the next section.
For all measurements in the Aeolotron, except the measurements in October 2016, a 28 mm lens for the IR camera was used. The resolution in this case is approximately 1.4 mm/pixel for a field of view of roughly 0.90 m · 0.72 m. For the measurements in October 2016 a 50 mm lens was used. The resulting resolution is 0.7 mm/pixel for a field of view of 0.45 m · 0.36 m. Both lenses have fixed f-numbers of f/2.

(a) (b)

Figure 4.5.: Photos of the experimental setup for the thermographic measurements at the Aeolotron. (a) shows the IR camera and the black aluminium tubes which shield the IR laser beam. (b) shows the CO_2 laser Synrad Evolution 100. In both images the Qioptiq X 95 bars carrying the optical components are visible.

4.1.3. Estimating Uncertainties in the Applied Heat Flux Density

As described in section 3.4, for the present experiments diffractive beam homogenizers have been used to heat an area on the water surface. Both diffractive beam homogenizer models used for the experiments, create a square intensity profile with an opening angle of 19.92°. The fixed opening angle becomes a problem in the presence of large gravity waves that modulate the distance between the diffractive beam homogenizer and the water surface significantly. Figure 4.6 schematically shows the change of size of the heated area due to the change in the distance between the diffractive optical element (DOE) and the water surface for the simple assumption, that the water surface is moved up and down like a plane and not locally modulated like by a realistic wave. The change in area of the heated area A_{heated} directly corresponds to a change in the heat flux density j_{heat} at the water surface:

$$j_{heat} = \frac{P_{laser}}{A_{heated}} \tag{4.1}$$

with the optical output power of the laser P_{laser}. Typically an excitation with one frequency takes between 1.5 and 5 minutes depending on wind speed. This

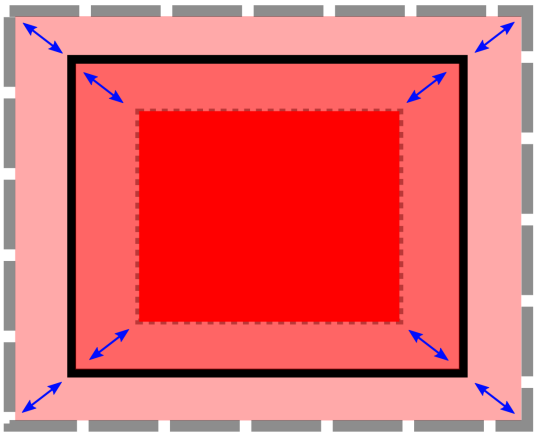

Figure 4.6.: Schematic representation of the variation of the size of the heated area on the water surface due to the change in distance between the diffractive beam homogenizer and the water surface.

means, that the heat flux density is an average over all the different heat flux densities, that occur during this time due to the surface modulation by waves. To estimate the effect of the variability in the heat flux density due to waves, a simple calculation is made: A sinusoidal modulation of the distance between the diffractive beam homogenizer and the water surface is assumed, that lifts the whole water surface corresponding to the phase of the sine. Then the average over all resulting heat flux densities for the whole period time of the sine is taken and compared to the static case where no height modulation of the water surface happens.
Wave height measurements have not been done in parallel with all measurements conducted within the scope of this thesis, however, for estimating the effect it is not necessary to have a perfectly simultaneously measured wave height. Instead data from Bopp [11] is taken. In the presence of a wave absorber the gravity waves will not become as large as they do with infinite fetch (c.f. section 4.1.1). To have an estimation for an extreme case, the largest wind speed for a clean water surface from Bopp [11] is taken, i.e. a wind speed of $u_{ref} = 9.74$ m/s. The presence of surface active material will dampen the waves and thus potentially reduce the wave height. Note that for a few conditions in this thesis, the wind speed was slightly higher (11.3 m/s) than the 9.74 m/s from Bopp. At 9.74 m/s the significant wave height is 27.36 cm. As this corresponds to the peak to peak displacement of the water surface the amplitude is only 13.68 cm, assuming a simple sinusoidal wave. With these parameters, the distance between the diffractive beam homogenizer and the water surface of 1.4 m and the opening angle of 19.92° of the diffractive beam homogenizer and an output power of

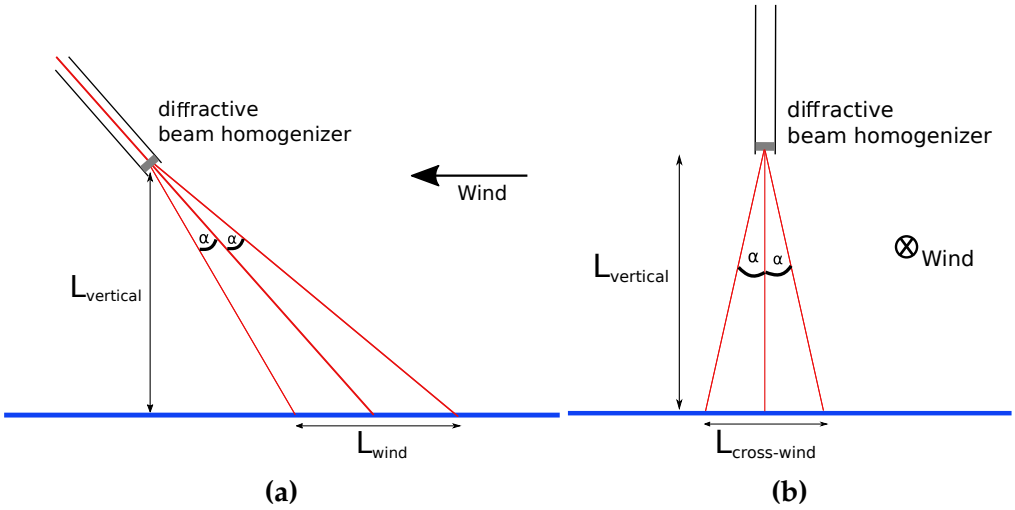

Figure 4.7.: Schematic drawing of the laser beam expansion into an area in the Aeolotron. (a) shows the beam expansion in wind direction, (b) shows the beam expansion along cross wind direction. 2α correspond to the opening angle of the diffractive beam homogenizer of 19.92°. Note that the angle of inclination of the laser beam is not in scale with the opening angle of the diffractive beam homogenizer.

150 W of the IR laser, the static heat flux density for the elevation of the water surface can be calculated to be $j_{heat} = 611.08\ \frac{W}{m^2}$. The average heat flux density for a complete cycle of sinusoidal modulation is $\overline{j_{heat}} = 616.97\ \frac{W}{m^2}$. The difference between the two values is only 1 %.
However, the simple expansion scheme as shown in figure 4.6 is only present in the Marseille facility (c.f. section 4.2.1). In the Aeolotron the laser beam cannot be directed onto the water surface straight vertically due to reasons explained in section 4.1.2. The laser beam has an inclination of 20° to the vertical axis in wind direction. This is visualized in figure 4.7, where 2α correspond to the opening angle of 19.92° of the diffractive beam homogenizer. Note that the angles are not to scale for a clearer representation. Due to the inclination in wind direction, the expansion of the heated area will change in cross wind direction with the distance from the diffractive beam homogenizer even for a static water surface without elongation due to waves. The laser intensity profile on the water surface is thus a trapeze instead of a square. This trapeze then also changes the size with surface modulation due to waves. This is schematically shown in figure 4.8. Taking into account the inclination of the IR laser beam of 20°, the calculation for the heat flux density variation yields :

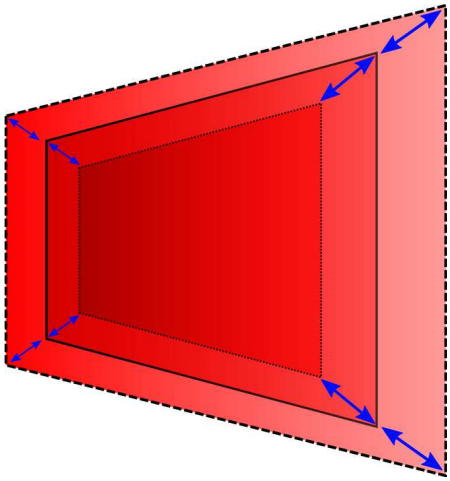

Figure 4.8.: Variation of the size of the heated area on the water surface due to the change in distance between the diffractive beam homogenizer and the water surface. Due to the inclination of the diffractive beam homogenizer in wind direction, the heated area is a trapeze rather than a square.

$$j_{heat} = 477.26 \ \frac{W}{m^2}$$
$$\overline{j_{heat}} = 472.70 \ \frac{W}{m^2}$$

with j_{heat} the heat flux density for a calm water surface and $\overline{j_{heat}}$ the average heat flux density for the case with wave amplitudes of 13.68 cm as described above. The variation is again only 1 %. If not the mean intensity is regarded, but only the difference between the maximum and minimum laser intensity (wave crest vs. wave trough), then the deviation is much larger:

$$j_{heat,max} = 580.63 \ \frac{W}{m^2}$$
$$j_{heat,min} = 392.29 \ \frac{W}{m^2}$$

where $j_{heat,max}$ is the heat flux density at a wave crest and $j_{heat,minx}$ corresponds to the heat flux density in the trough of a wave. The relative difference is 48%. Additionally, another effect is important for the case where the heated area is a trapeze: Since the heated area changes its elongation in cross wind direction, the heat flux density will have a gradient in wind direction. Moving along wind direction, the heat flux density will be the lowest, where the cross wind expansion of the heated area is the largest. As can be seen from figure 4.7, this is where the surface water enters the heated area. The heat flux density then

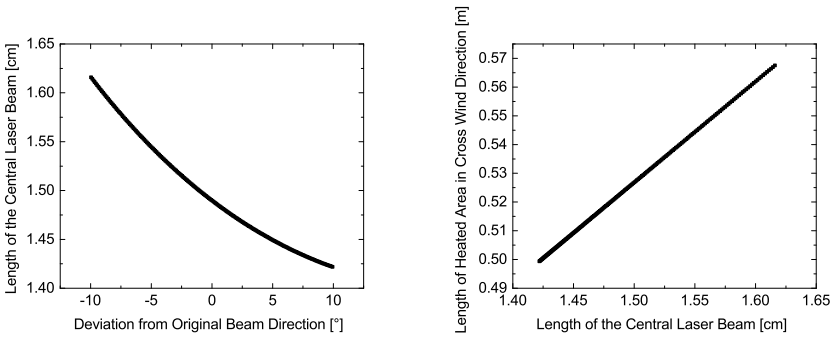

(a) **(b)**

Figure 4.9.: (a) shows the length of a central laser beam in wind direction for different angles α from figure 4.7a. (b) shows the corresponding expansion of the heated area in cross wind direction for the beam lengths from (a).

gradually increases as the water advances further through the heated area. This effect cannot be avoided in the Aeolotron, but it is important to remember it, when analysing the data. The maximum change in the elongation in cross wind direction for the typical case in the Aeolotron, as described above, is 13.7 %. Figure 4.9 shows how the expansion of the cross wind elongation of the heated area changes with the position in wind direction. For the experiments, in most cases a focussing lens is used in front of the diffractive beam homogenizer to reduce the opening angle and to increase the heat flux density on the water surface. The resulting opening angle is typically 15° after the focussing lens and the difference of the cross wind elongation of the heated area reduces to 10 % in this case.

4.2. Pytheas

The Pytheas facility in Marseille-Luminy, France, is a linear wind-wave tank. The facility is 40 m long and 2.6 m wide. The water depth varies with the distance from the wind inlet and is approximately 0.9 m at the position of the optical measurements. The distance from the water surface to the ceiling of the facility is 1.4 m.
At Pytheas the wind is recirculated. A large tube connects both ends of the facility and runs above the wind-wave tunnel. In this tube a large fan generates the wind. Wind speeds can be set up to 14 m/s. A detailed description about the Marseille facility can be found in Coantic and Bonmarin [16].

4.2.1. Setup at Pytheas

For the experiments at the Marseille facility two lasers instead of one laser were used, in order to increase the size of the heated area, and to have a larger region for the thermal equilibrium (c.f. section 3.4). How the two lasers have been arranged to achieve one larger area that is heated on the water surface is described in section 4.2.2. Additionally, two new diffractive beam homogenizers (c.f. section 4.5) have been bought for the application in Marseille. These homogenizers offer a much better spatial homogeneity compared to the one used for the experiments in Heidelberg in 2014 and 2015 (more details about the different beam homogenizers are given in section 4.5 and in section 7.1.1). The experimental setup of the thermographic measurement devices is shown in

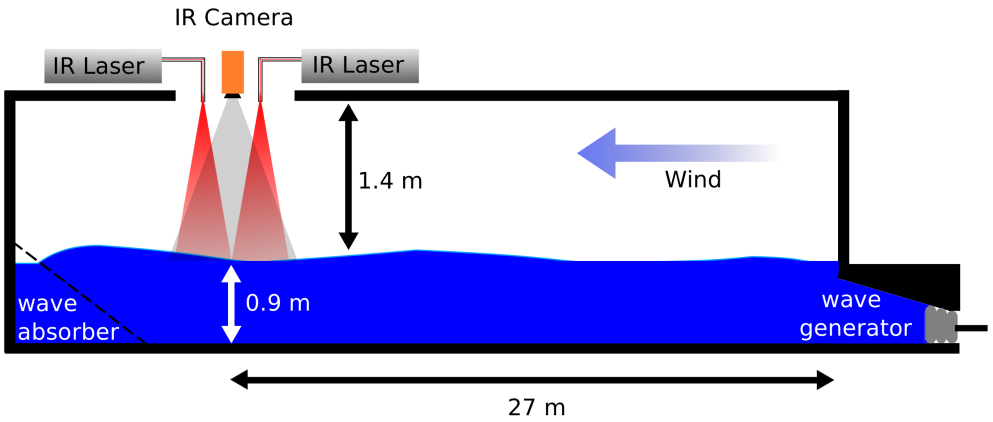

Figure 4.10.: Schematic representation of the experimental setup in the linear wind-wave facility in Marseille. Modified after Caulliez [14].

figure 4.10 schematically and figure 4.11 shows a photograph of the CO_2 lasers and the infrared camera mounted on the ceiling of Pytheas.
In Marseille a 25 mm lens was used for the IR camera. The spatial resolution is 1.9 mm/pixel. This lens has a fixed f-number of f/2.

4.2.2. Minimizing the Uncertainties of the Applied Heat Flux Density

In order to get one large area out of the two separate intensity profiles, there are mainly two possibilities. If both laser beams are sent down straight vertically

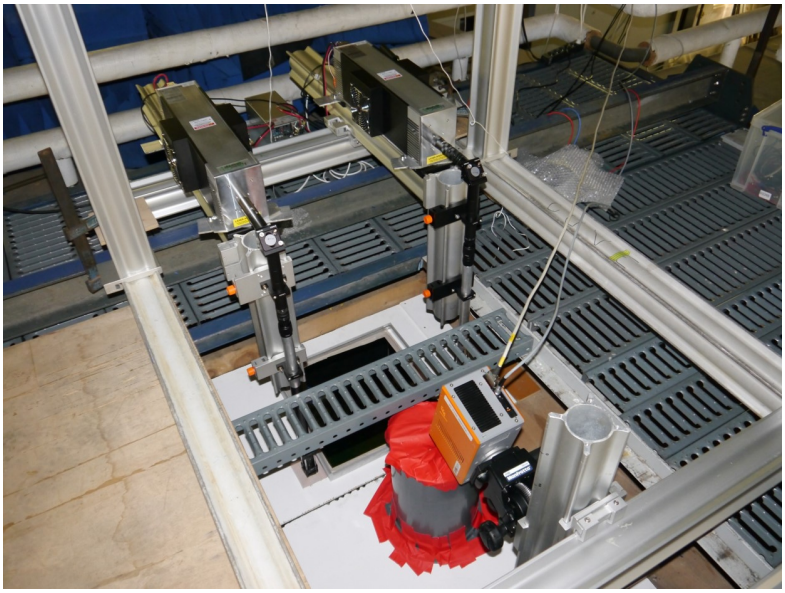

Figure 4.11.: Photo of the setup of the components used for the thermographic measurements in Marseille. The two lasers and the aluminium tubes, that are used to shield the laser beam for safety reasons, can be seen in the background. In the foreground the orange IR camera can be seen. The red tape is used to make the facility air tight, so that the simultaneously conducted gas transfer measurements are not disturbed.

onto the water surface, waves will affect the matching of the two profiles. If the profiles are mapped at a flat water surface, the profiles will overlap for the case of a wave trough and there will be a gap between the profiles for the case of a wave crest.
An alternative way to combine the two laser intensity profiles is to incline both diffractive beam homogenizers by half their opening angle. In this way one outer side of a single laser intensity profile will shine down straight vertically onto the water surface. If the two lasers are positioned in a way, that the two sides of the single laser intensity profiles are mapped next to each other, where the laser radiation is going straight down to the water surface, then the mapping is independent of waves. However, the single intensity profiles are then trapezes again, like discussed in section 4.1.3. Figure 4.12 shows the two possible ways to arrange the laser beams.

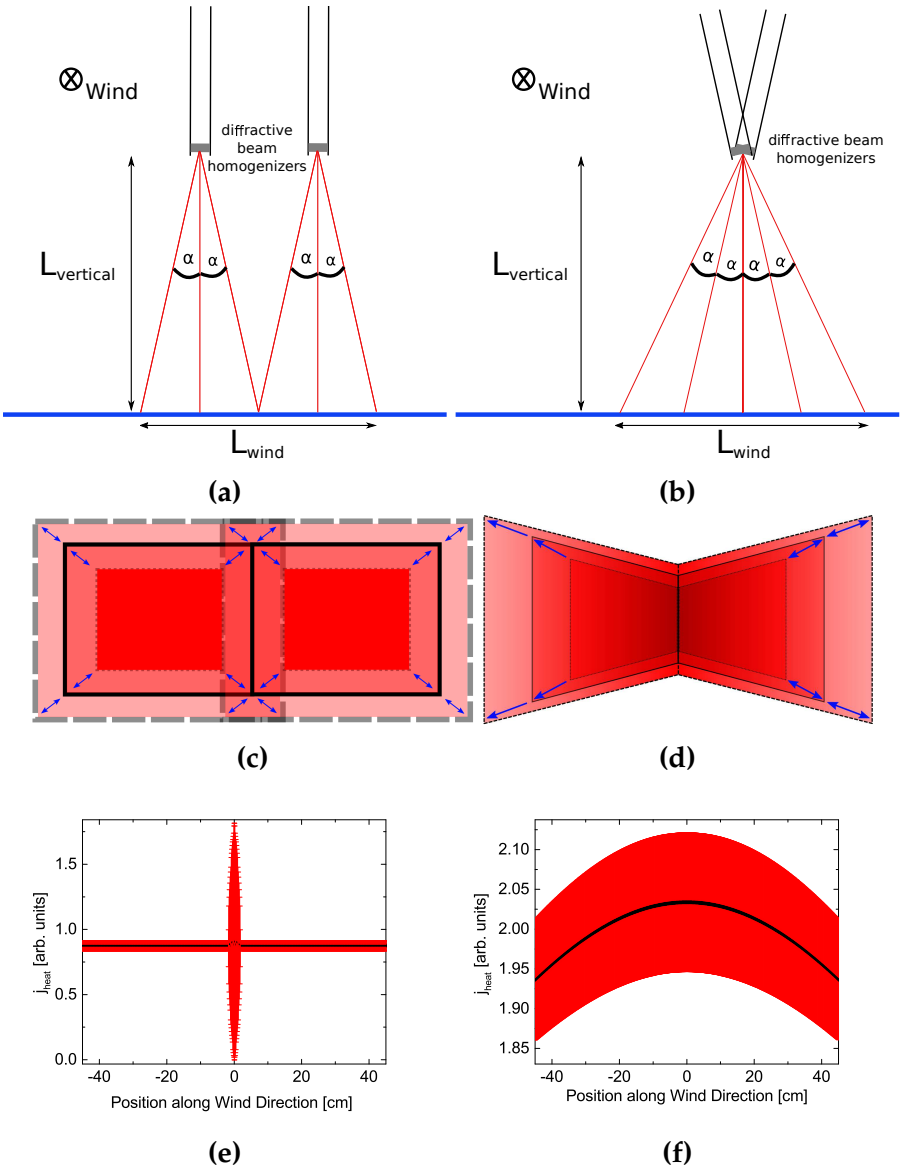

Figure 4.12.: Two possible ways to combine two separate laser intensity profiles from two diffractive beam homogenizers into one large intensity profile. (a) shows a method where both laser beams are sent down straight vertically onto the water surface, while (b) shows a solution with an inclination of both laser beams. The resulting intensity distributions on the water surface can be seen in (c) and (d) respectively. (e) and (f) show intensity profiles along the wind direction. The computation of these intensity profiles is explained in section A.2.

4.3. Calibration of the IR Camera

The infrared camera used for the measurements during this thesis is an IRCAM Velox 327k M. This device is a quantum detector with a NETD of 20 mK (c.f. section 3.1.1). The sensor consists of 640 x 512 pixels. The properties of the camera are summarized in table 4.1. Due to imperfect manufacturing processes

Table 4.1.: Specifications of the infrared camera used for the measurements. The listed values are taken from the data sheet of the manufacturer.

IRCAM Velox 327k M	
Detector Type	CMT Focal Plane Array
Format	640x512 Pixels
Spectral Range	3.4 to 5 µm
Maximal Frame Rate (Full Sensor)	207 Hz
Integration Time	50 µs - 12.75 ms
NETD	20 mK
A/D Resolution	14 Bit

not all of these pixels have the same sensitivity and the same offset. This causes inhomogeneities in the recorded images, as can be seen in figure 4.15. To correct for these inhomogeneities and to convert the measured intensities into temperatures, a calibration of the IR camera is needed. As the optical properties of the camera change with the used lens, a new calibration is needed for each lens.
The calibration procedure requires an object with a well known temperature and well known emissivity. A so-called black body target is used. This is a device that has a specially treated surface with an emissivity close to 1, i.e. nearly a perfect black body. The black body used for the calibration of the IR camera for this thesis is a SBIR 2006G. This device can be adjusted to temperatures between 10°C and 60°C with an accuracy of 0.01 K and features an emissivity of 0.985 ± 0.015 for wavelengths between 2 µm and 14 µm. A picture of the black body device is shown in figure 4.13. As all the measurements in this thesis were laboratory measurements, where room temperature was the predominant temperature regime, the camera was calibrated for a temperature range between 15 and 30 °C in 250 mK steps.
For each temperature step, 1000 images are recorded and the mean of these images is computed per pixel. In this way an average value per pixel and temperature step for the temperatures within the calibration range is obtained. Then for each pixel a least squares optimization with a quadratic function is calculated

Figure 4.13.: Photo of the black body calibration unit used to calibrate the IR camera. The inner black surface at the front is the area used for the calibration.

for an intensity vs. temperature plot. From the resulting quadratic function it is possible to assign a temperature to the measured intensity at each pixel. Figure 4.14 shows an example for such a least squares fit.

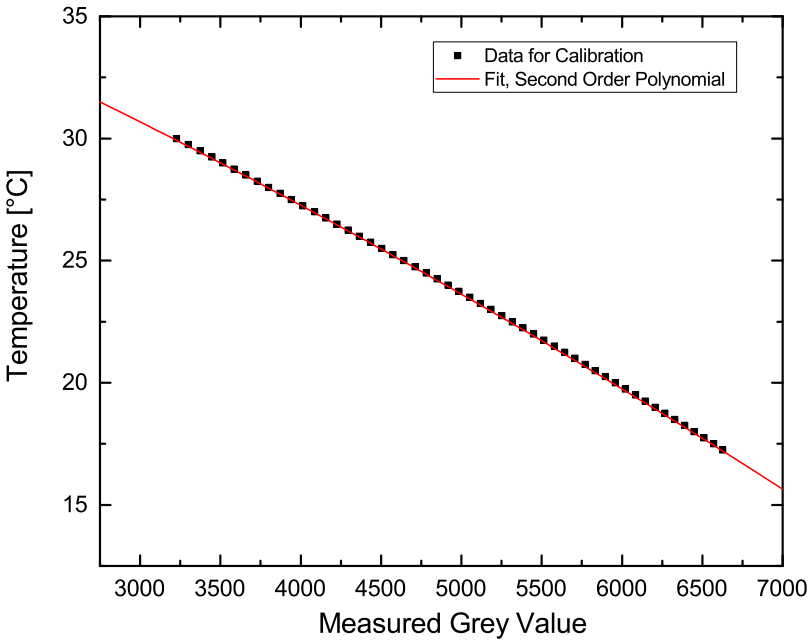

Figure 4.14.: Example for a quadratic fit, used to convert measured intensities into temperatures.

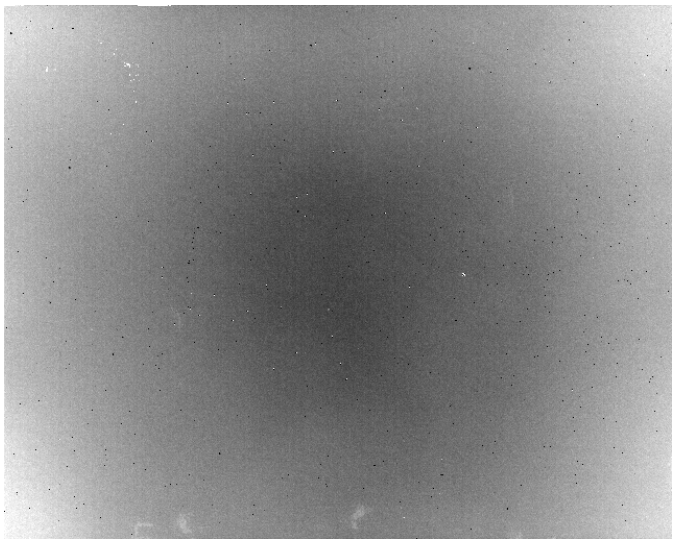

Figure 4.15.: Example of an uncalibrated image of the black body surface with a constant temperature of 22°C across the whole image. The inhomogeneity of the sensor can clearly be seen.

4.4. Characterization of the IR Lasers

Two different laser models have been used for the experiments that were carried out during this thesis. Both laser models are CO_2 laser operating at 10.6 µm. This is a very important property of the laser radiation, since at 10.6 µm the absorption in air is very low [50]. The Synrad Evolution 100 is a water-cooled laser. For the experiment in Marseille two Iradion Infinity 100 were bought: The Infinity 100 are air-cooled and therefore much more compact and easier to transport, as no chiller needs to accompany the lasers.
For the controlled flux technique mainly two properties of the IR laser are important. The first one is the output power of the laser and the stability of this output power and the second one is the shape of the beam profile. As the beam profiles of both lasers used for this theses were suitable for the use of diffractive beam homogenizers, the initial beam profiles of the lasers are no longer of importance to the actual measurement, as the intensity profile at the water surface is dominated by the performance of the diffractive beam homogenizers.
The output power of the laser, however, is crucial to the measurement, as it provides the heat flux density at the water surface. Thus it is important to know this quantity and also to know how much it is fluctuating. Figure 4.16 shows the results of the measurements of the optical output power of the two different laser models used for the experiments that were conducted within the scope of this thesis. It can be seen, that the Iradion lasers provide higher output power although they are air-cooled compared to the water-cooled Synrad laser.
According to the data sheets, the Synrad Evolution 100 has an output power fluctuation of less than 5%. The Iradion Infinity lasers fluctuate between 6 and 7% according to the manufacturer's specifications.
The higher output power, only slightly increased power fluctuation and the fact, that no chiller for water cooling is needed, make the Iradion Infinity 100 lasers ideal tools for field measurements, like for measurements from a ship.
The specifications of the two laser models are listed in table 4.2.

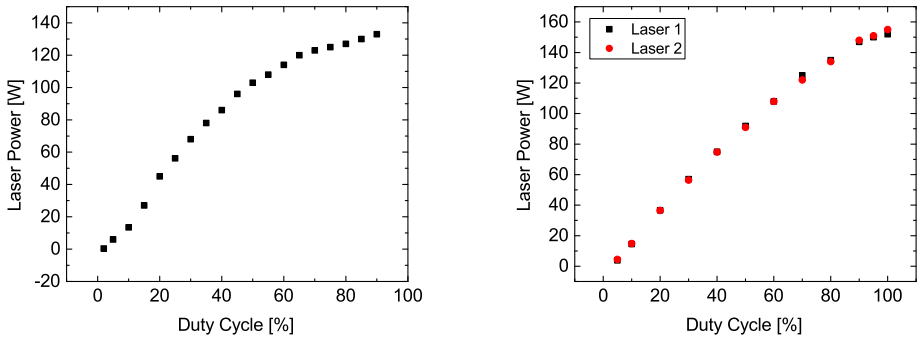

Figure 4.16.: Measured laser output power of all three lasers that have been used for the experiments of this thesis. In (a) the output power of the water-cooled Synrad Evolution 100 is shown. In (b) the output power of the two air-cooled Iradion Infinity 100 lasers can be seen. Note that the duty cycle that controls the laser power is independent of the duty cycle used for the excitation signal to heat the water surface (c.f. section 3.3.3).

Table 4.2.: Specifications of the CO_2 lasers used for the measurements. The listed values are taken from the data sheets of the manufacturers.

	Synrad Evolution 100	**Iradion Infinity 100**
Output Power [W]	100	100
Mode Quality	$M^2 < 1.2$	$M^2 < 1.2$
Beam Diameter [mm]	4	2.5
Beam Divergence [mR]	3.5	5.2
Wavelength [µm]	10.59	10.57 - 10.63
Power Stability from Cold	±5%	±6%
Polarization	Linear (Vertical)	Random
Cooling	Water-Cooled	Air-Cooled

4.5. Diffractive Beam Homogenizers

Two different diffractive beam homogenizers have been used for the experiments conducted during this thesis. The first one is a Holo/Or HM-271-A-Y-A, the second one a Holo/Or HH- 211-A-Y-A. The difference between the two homogenizers is, that the second one produces a higher homogeneity. It also significantly reduces the intensity at the zero diffraction order. The specifications of the two different homogenizer models are listed in table 4.3. The overall efficiency states

Table 4.3.: Specifications of the diffractive beam homogenizers. The listed values are taken from the data sheets of the manufacturer.

	Holo/Or HM-271-A-Y-A	**Holo/Or HH-211-A-Y-A**
Wavelength [µm]	10.6	10.6
Min. Beam Dia. [mm]	5	5
Beam Mode	SM or MM	SM or MM
Element Type	Window	Window
Material	ZnSe	ZnSe
Diameter [mm]	25.4	25.4
Clear Aperture [mm]	22.8	22.9
Thickness [mm]	3	3
Coating	AR/AR	AR/AR
Output Shape	Square	Square
Diffusion Angle [°]	19.92x19.92	19.92x19.92
Trans. Efficiency [%]	≈ 100	≈ 100
Overall Efficiency [%]	76	71

what amount of the incoming radiation ends up in the desired output intensity profile. The remaining fraction of the incoming power ends up in higher diffraction orders that are outside the target area. Images of the different intensity profiles of both homogenizer models can be found in section 7.1.1.

5 Experiments

In this chapter the different experiments conducted within the scope of this thesis are presented. The first section explains the measurements performed between May and August 2015 in the Aeolotron in Heidelberg. Those measurements were dedicated to investigate the influence of surface films and fetch on heat exchange across the aqueous boundary layer. The second section of this chapter details a measurement campaign with actual sea water from the North Sea, that was carried out during November 2014 in the Aeolotron in Heidelberg. The third section presents a measurement campaign conducted during September and October 2016 in the Aeolotron where unknown biological activity in the water influenced the measurements. The forth section is dedicated to explain the measurement campaign at the large linear wind-wave facility Pytheas in Marseille, France, that took place in June 2016. Details about the experimental setup at the Aeolotron and at the Marseille facility are given in chapter 4 and the concept behind the measurement technique is discussed in detail in chapter 3. The last section of this chapter thus focuses on the measurement procedure and especially on the actual implementation of the excitation scheme.

Note 1: In the tables listed in this chapter and in the corresponding graphs in chapter 7, u_{ref} always denotes the reference wind speed, as it was measured within the wind-wave facility. Due to faulty measurements by the wind sensors in the Aeolotron, not the individually measured wind speeds are listed, but averaged wind speed values. Small changes in the wind speed could not be resolved with certainty due to technical problems with the wind sensors at the Aeolotron.

Note 2: All listed friction velocities are water side friction velocities. The values for the friction velocity u_* have been estimated by Maximilian Bopp based on a momentum balance method [9]. For the measurements in Marseille, u_* values were provided by Guillemette Caulliez from MIO at the University of Marseille.

Note 3: The values for the mean square slope (mss) of the water surface were measured with the imaging slope gauge [61]. The values were taken from the

live evaluation that has been implemented by Daniel Kiefhaber and that has been validated by Proß [87]. mss values from the measurement campaign in Marseille were provided by Guillemette Caulliez from MIO at the University of Marseille.
Note 4: All values listed in the tables below are given with all digits as provided to the author. The number of digits behind the decimal point however does not necessarily represent the actual measurement accuracy.

5.1. Systematic Experiments at the Aeolotron with Controlled Boundary Conditions

These experiments are the ones with the most defined boundary conditions in this thesis, apart from the measurements in Marseille. By controlling the boundary conditions, it is possible to change only one parameter at a time and to see its influence on the heat exchange process. In this way, precise systematic studies are possible. The measurement campaign was divided into three parts. The first part was the investigation of heat exchange for a clean water surface for a wind speed range of 1.2 m/s to 11.3 m/s. The second part was the investigation of the fetch dependence of heat exchange. Measurements with a systematic variation of the fetch length from 1 m to 22.7 m for wind speeds between $u_{ref} = 2.9$ m/s and 7 m/s were carried out.
For the last part of the measurement campaign, three different concentrations of the surfactant Triton X-100 have been added into the Aeolotron to investigate the influence of surfactants on heat exchange. The individual measurement conditions are listed in tables 5.1, 5.2, 5.3, 5.4 and 5.5.

Triton X-100 Triton X-100 is a nonionic soluble surfactant with the chemical formula $C_{14}H_{22}O\,(C_2H_4O)_n$. It consists of an aromatic hydrocarbon group which is hydrophobic and of a polyethylene oxide group which is hydrophilic.

Table 5.1.: Clean water measurement conditions in the Aeolotron.

date	u_{ref} [m/s]	fetch [m]	c_{Triton}	mss	u_* [cm/s]
19.06.2015	1.2	∞	0g/18000l	0.005352	0.335 ± 0.021
19.06.2015	2.3	∞	0g/18000l	0.010922	0.441 ± 0.026
19.06.2015	3.8	∞	0g/18000l	0.018232	0.621 ± 0.038
19.06.2015	4.7	∞	0g/18000l	0.045032	0.810 ± 0.052
19.06.2015	7.2	∞	0g/18000l	0.104728	1.552 ± 0.097
19.06.2015	9.7	∞	0g/18000l	0.167363	3.164 ± 0.184
22.06.2015	1.7	∞	0g/18000l	0.008933	
22.06.2015	3.0	∞	0g/18000l	0.012295	0.519 ± 0.031
22.06.2015	3.8	∞	0g/18000l	0.016454	0.621 ± 0.038
22.06.2015	5.8	∞	0g/18000l	0.071888	1.079 ± 0.070
22.06.2015	8.5	∞	0g/18000l	0.142629	2.149 ± 0.140
22.06.2015	11.3	∞	0g/18000l	0.190462	3.983 ± 0.297

Table 5.2.: Measurement conditions in the Aeolotron with fetch variation.

date	u_{ref} [m/s]	fetch [m]	c_{Triton}	mss
15.07.2015	4.7	2	0g/18000l	0.044695
15.07.2015	4.7	4	0g/18000l	0.048688
15.07.2015	4.7	7	0g/18000l	0.055346
15.07.2015	4.7	12	0g/18000l	0.059303
15.07.2015	4.7	16	0g/18000l	0.057624
15.07.2015	4.7	20.7	0g/18000l	0.051756
16.07.2015	5.8	2	0g/18000l	0.062285
16.07.2015	5.8	4	0g/18000l	0.064905
16.07.2015	5.8	7	0g/18000l	0.068988
16.07.2015	5.8	12	0g/18000l	0.072187
16.07.2015	5.8	16	0g/18000l	0.078727
16.07.2015	5.8	20.7	0g/18000l	0.076316
16.07.2015	7.2	2	0g/18000l	0.076051
16.07.2015	7.2	4	0g/18000l	0.091512
16.07.2015	7.2	7	0g/18000l	0.095528
16.07.2015	7.2	12	0g/18000l	0.103455
16.07.2015	7.2	16	0g/18000l	0.114778
16.07.2015	7.2	20.7	0g/18000l	0.107174

Table 5.3.: Measurement conditions in the Aeolotron with fetch variation.

date	u_{ref} [m/s]	fetch [m]	c_{Triton}	mss
17.07.2015	3.0	2	0g/18000l	0.001596
17.07.2015	3.0	4	0g/18000l	0.007308
17.07.2015	3.0	7	0g/18000l	0.014808
17.07.2015	3.0	12	0g/18000l	0.024797
17.07.2015	3.0	16	0g/18000l	0.030943
17.07.2015	3.0	20.7	0g/18000l	0.034917
20.07.2015	3.8	2	0g/18000l	0.023918
20.07.2015	3.8	4	0g/18000l	0.028402
20.07.2015	3.8	7	0g/18000l	0.036121
20.07.2015	3.8	12	0g/18000l	0.04685
20.07.2015	3.8	16	0g/18000l	0.048552
20.07.2015	3.8	20.7	0g/18000l	0.03887
20.07.2015	3.0	16	0g/18000l	0.033633

Table 5.4.: Measurement conditions in the Aeolotron with Triton X-100.

date	u_{ref} [m/s]	fetch [m]	c_{Triton}	mss	u_* [cm/s]
11.08.2015	1.2	∞	0.6g/18000l	0.000946	0.159 ± 0.017
11.08.2015	2.3	∞	0.6g/18000l	0.004832	0.316 ± 0.020
11.08.2015	3.8	∞	0.6g/18000l	0.009797	0.537 ± 0.032
11.08.2015	4.7	∞	0.6g/18000l	0.019122	0.706 ± 0.044
11.08.2015	7.2	∞	0.6g/18000l	0.098903	1.478 ± 0.094
11.08.2015	9.7	∞	0.6g/18000l	0.163587	3.017 ± 0.184
12.08.2015	1.7	∞	0.6g/18000l	0.002045	0.227 ± 0.017
12.08.2015	3.0	∞	0.6g/18000l	0.00779	0.424 ± 0.025
12.08.2015	3.8	∞	0.6g/18000l	0.010284	0.539 ± 0.032
12.08.2015	5.8	∞	0.6g/18000l	0.062817	0.987 ± 0.064
12.08.2015	8.5	∞	0.6g/18000l	0.137669	2.074 ± 0.137
12.08.2015	11.3	∞	0.6g/18000l	0.182632	3.965 ± 0.282

Table 5.5.: Measurement conditions in the Aeolotron with Triton X-100.

date	u_{ref} [m/s]	fetch [m]	c_{Triton}	mss	u_* [cm/s]
13.08.2015	1.2	∞	3g/18000l	0.001074	0.159 ± 0.017
13.08.2015	2.3	∞	3g/18000l	0.001128	0.276 ± 0.019
13.08.2015	3.8	∞	3g/18000l	0.005943	0.504 ± 0.030
13.08.2015	4.7	∞	3g/18000l	0.006720	0.504 ± 0.030
13.08.2015	7.2	∞	3g/18000l	0.082631	1.333 ± 0.083
13.08.2015	9.7	∞	3g/18000l	0.162741	3.005 ± 0.168
14.08.2015	1.7	∞	3g/18000l	0.001011	0.187 ± 0.017
14.08.2015	3.0	∞	3g/18000l	0.003789	0.388 ± 0.023
14.08.2015	3.8	∞	3g/18000l	0.005729	0.502 ± 0.030
14.08.2015	5.8	∞	3g/18000l	0.019323	0.831 ± 0.053
14.08.2015	8.5	∞	3g/18000l	0.131217	2.011 ± 0.131
14.08.2015	11.3	∞	3g/18000l	0.185675	3.951 ± 0.281
19.08.2015	1.2	∞	15g/18000l	0.000957	0.139 ± 0.017
19.08.2015	2.3	∞	15g/18000l	0.001136	0.286 ± 0.019
19.08.2015	3.8	∞	15g/18000l	0.001049	0.444 ± 0.026
19.08.2015	4.7	∞	15g/18000l	0.00104	0.543 ± 0.032
19.08.2015	7.2	∞	15g/18000l	0.012961	0.973 ± 0.063
19.08.2015	9.7	∞	15g/18000l	0.153500	2.984 ± 0.188
21.08.2015	1.7	∞	15g/18000l	0.000934	0.185 ± 0.017
21.08.2015	3.0	∞	15g/18000l	0.001024	0.35 ± 0.021
21.08.2015	3.8	∞	15g/18000l	0.001548	0.442 ± 0.026
21.08.2015	5.8	∞	15g/18000l	0.004197	0.71 ± 0.045
21.08.2015	8.5	∞	15g/18000l	0.112596	1.98 ± 0.118
21.08.2015	11.3	∞	15g/18000l	0.177761	4.145 ± 0.363

5.2. Sea Water in the Aeolotron with Natural Surfactants

In November 2014, measurements with actual sea water were conducted in the Aeolotron in Heidelberg. The experiment was part of the German SOPRAN[1] project and there were several working groups from different institutes and three different countries involved in the experiment.
The research vessel Poseidon had collected 20 m^3 of sea water from the North Sea. The water had been collected at depths of 50 m and 5 m. Figure 5.1 shows the location of the origin of the sea water in the North Sea and the route the sea water has taken to reach Heidelberg. The sea water was delivered at the end of September 2014 and was stored in the cellar of the Institute of Environmental Physics in the storage tanks of the Aeolotron. The actual measurements took place during November 2014. No filtering or chemical treatment of the sea water took place, thus all biological components remained in the water.
This thesis is dedicated to the investigation of air-water heat transfer and therefore not the entire sea water experiment will be explained here, but only aspects that are important for the investigation of heat transfer are presented.
The biological activity still present in the sea water produced natural surface films. To be able to compare the measurements with Triton X-100 described above to the sea water measurements with natural surfactants, data provided by Mariana Ribas Ribas and her colleagues from Oliver Wurl's research group from the ICBM at the University of Oldenburg is used. They performed an analysis of the surface and bulk concentrations of surfactants and calculated Triton X-100 equivalent concentrations.
The individual measurement conditions are listed in tables 5.6, 5.7, 5.8 and 5.9.

[1] Surface Ocean Processes in the Antropocene, the German BMBF funded contribution to the SOLAS programme, http://sopran.pangaea.de/.

(a) (b)

Figure 5.1.: Origin and transportation of the sea water for the measurements in the Aeolotron in November 2014. (a) shows the transfer of the sea water from the research vessel Poseidon into a tanker lorry. Figure provided by Martin Sperling, GEOMAR Helmholtz Centre for Ocean Research, Kiel. (b) shows the positions where the sea water has been taken from the North Sea and the approximate route it has taken to reach Heidelberg. Figure provided by Kerstin Krall, Institute of Environmental Physics, Heidelberg University.

Table 5.6.: Measurement conditions of the first week with sea water in the Aeolotron.

date	u_{ref} [m/s]	fetch [m]	c_{Triton} [g/18000l]	mss	u_* [cm/s]
04.11.2014	1.2	∞	21.0 ± 6.7	0.0002926	
04.11.2014	2.3	∞	8.5 ± 0.8	0.0005729	
04.11.2014	3.8	∞	10.6 ± 0.4	0.000311	0.408 ± 0.024
04.11.2014	4.7	∞	8.2 ± 0.2	0.0003405	0.539 ± 0.032
04.11.2014	7.2	∞	17.3 ± 0.7	0.1026	1.44 ± 0.085
04.11.2014	9.7	∞	13.9 ± 1.3	0.168	2.858 ± 0.207
06.11.2014	1.7	∞	18.3 ± 0.7	0.0004318	0.224 ± 0.017
06.11.2014	3.0	∞	9.4 ± 0.8	0.0003283	0.356 ± 0.022
06.11.2014	3.8	∞	11.0 ± 1.0	0.000649	0.439 ± 0.026
06.11.2014	5.8	∞	6.9 ± 0.3	0.05299	0.976 ± 0.067
06.11.2014	8.5	∞	9.4 ± 0.1	0.1368	2.031 ± 0.131

Table 5.7.: Measurement conditions of the second week with sea water in the Aeolotron.

date	u_{ref} [m/s]	fetch [m]	c_{Triton} [g/18000l]	mss	u_* [cm/s]
11.11.2014	1.2	∞	34.7 ± 7.8	0.0003598	0.168 ± 0.017
11.11.2014	2.3	∞	12.3 ± 0.3		0.255 ± 0.018
11.11.2014	3.8	∞	10.5 ± 0.4	0.0003648	0.416 ± 0.025
11.11.2014	4.7	∞	9.2 ± 0.4	0.0004604	0.531 ± 0.031
11.11.2014	7.2	∞	9.0 ± 0.0	0.09395	1.442 ± 0.089
13.11.2014	1.7	∞	13.2 ± 0.4	0.0003367	0.181 ± 0.017
13.11.2014	3.0	∞	8.7 ± 0.6	0.0003679	0.303 ± 0.019
13.11.2014	3.8	∞	9.3 ± 0.6	0.0004171	0.402 ± 0.024
13.11.2014	5.8	∞	7.9 ± 0.4	0.05202	0.934 ± 0.059
13.11.2014	8.5	∞	10.5 ± 0.5	0.1299	1.993 ± 0.131
13.11.2014	9.7	∞	8.1 ± 0.6	0.1492	2.933 ± 0.195

Table 5.8.: Measurement conditions of the third week with sea water in the Aeolotron.

date	u_{ref} [m/s]	fetch [m]	c_{Triton} [g/18000l]	mss	u_* [cm/s]
19.11.2014	1.2	∞	13.5 ± 0.8		
19.11.2014	2.3	∞	10.6 ± 1.1	0.0003748	0.264 ± 0.018
19.11.2014	3.8	∞	11.5 ± 0.7	0.0004822	0.423 ± 0.025
19.11.2014	4.7	∞	10.3 ± 0.4	0.004466	0.529 ± 0.032
19.11.2014	7.2	∞	11.4 ± 1.6	0.08261	1.459 ± 0.090
19.11.2014	9.7	∞	9.0 ± 0.2	0.1267	2.964 ± 0.192
21.11.2014	1.7	∞	12.4 ± 0.9	0.0003635	0.173 ± 0.017
21.11.2014	3.0	∞	10.4 ± 1.0	0.0003796	0.309 ± 0.020
21.11.2014	3.8	∞	10.5 ± 1.1	0.0004227	0.386 ± 0.023
21.11.2014	5.8	∞	7.3 ± 0.7	0.05351	0.964 ± 0.060
21.11.2014	8.5	∞	5.4 ± 0.5		1.993 ± 0.128
21.11.2014	11.3	∞	4.8 ± 0.7		3.919 ± 0.306

Table 5.9.: Measurement conditions of the fourth week with sea water in the Aeolotron.

date	u_{ref} [m/s]	fetch [m]	c_{Triton} [g/18000l]	mss	u_* [cm/s]
24.11.2014	1.2	∞	8.1 ± 0.6	0.001324	0.152 ± 0.017
24.11.2014	2.3	∞	6.3 ± 0.5	0.003522	0.152 ± 0.017
24.11.2014	3.8	∞	6.0 ± 0.3	0.008953	0.46 ± 0.027
24.11.2014	4.7	∞	4.9 ± 0.3	0.01265	0.607 ± 0.037
24.11.2014	7.2	∞	6.4 ± 0.6	0.07715	1.479 ± 0.089
24.11.2014	9.7	∞	9.3 ± 1.0		3.04 ± 0.202
26.11.2014	1.2	∞	4.9 ± 0.4	0.0003135	0.158 ± 0.017
26.11.2014	2.3	∞	4.5 ± 0.1	0.0003263	0.279 ± 0.019
26.11.2014	3.8	∞	7.1 ± 0.6	0.0003998	0.435 ± 0.026
26.11.2014	4.7	∞	5.5 ± 0.3	0.0009757	0.539 ± 0.032
26.11.2014	7.2	∞	6.1 ± 0.4	0.07382	1.494 ± 0.090
26.11.2014	9.7	∞	6.0 ± 0.6	0.116	2.914 ± 0.209
29.11.2014	1.7	∞	5.6 ± 0.3	0.000313	
29.11.2014	3.0	∞	9.8 ± 0.6	0.0003336	0.308 ± 0.020
29.11.2014	3.8	∞	10.1 ± 1.0	0.0003477	0.39 ± 0.023
29.11.2014	5.8	∞	6.5 ± 0.4	0.05101	0.957 ± 0.060
29.11.2014	8.5	∞	9.0 ± 0.7	0.1096	2.029 ± 0.128
29.11.2014	11.3	∞	6.1 ± 0.6	0.1272	4.008 ± 0.307

5.3. Measurement Campaign 2016 at the Aeolotron with Unknown Biological Activity

An extensive measurement campaign with clean deionized water had been planned for September and October 2016 where all the presently available experiments in the Aeolotron should be combined.
However, during theses experiments, some form of bacteria started to proliferate in the water of the Aeolotron, despite the fact that deionized water had been used and that the pH value had been lowered to four for the boundary layer imaging technique (details about this technique can be found in Kräuter [63]). One possible explanation is, that the bacteria had been introduced to Heidelberg from the Marseille experiment in June 2016 (see section 5.4) through the tubes for the gas exchange measurements, which had been in constant contact with the water in the Marseille facility. The bloom of theses bacteria might have been initiated by the ammonia fluxes that are needed for the boundary layer imaging technique (BLI). Theses ammonia fluxes had been adjusted for the measurement campaign and were in part more than twice as high as the ammonia fluxes used by Kräuter in 2014 [63]. Ammonia might have served as nutrition for the bacteria and thus, they could thrive in the Aeolotron due to the steady supply of ammonia for the BLI measurements. These bacteria somehow influenced the water surface by producing jellylike particles, that accumulated at the water surface during the measurements and thereby influenced the roughness of the water surface. For this measurement campaign, however, no Triton X-100 equivalent concentrations of surface active material are available, as no water samples have been taken during the experiment.
The friction velocity values have not been evaluated yet and are thus not available for this thesis. However, values for the mean square slope (mss) of the water surface are available for some measurement conditions. Unfortunately, due to the measurement scheme for newly installed air flow measurements, the imaging slope gauge was occupied with data saving for times of up to 1.5 hours during the measurements. This made it impossible at some conditions to estimate mss values for the time period where the thermographic measurements took place. Apart from this systematic problem in the measurement scheme, the surface roughness and thus mss sometimes changed by a factor of two within an hour due to the biological activity in the water. This made it very challenging to estimate a value for mss that could be used for comparisons with other measurements.
Another problem was, that one LED line of the ISG was broken, which means, that the ISG could not operate accurately during some measurement conditions.

Table 5.10.: Measurement conditions with unknown biological activity in the Aeolotron.

date	u_{ref} [m/s]	fetch [m]	mss
12.10.2016	9.7	∞	
14.10.2016	3.8	∞	
17.10.2016	5.8	∞	0.08778
18.10.2016	8.5	∞	0.17341
19.10.2016	4.7	∞	0.03556
21.10.2016	3.0	∞	0.00926

On top of that, the thermographic measurement setup suffered from a laser failure after two weeks of measurements.
Due to the complications explained above, the author has selected a few conditions, where mss values are available for the time period, where the thermographic measurements have been conducted. Those conditions are listed in table 5.10. For the measurements performed on the 12th of October, no mss value is available, but at the wind speed of 9.7 m/s mss is expected to be stable and comparable to clean surface conditions, c.f. section 7.2.3. For the measurement performed on the 14th of October, also no mss is available, however, the condition appeared stable during the whole measurement time, as judged by the eye. As the number of conditions, where mss is available, is very limited for the measurement campaign at hand, the focus had been shifted to compare different thermographic measurement schemes including the newly developed multifrequency excitation (c.f. sections 7.1.3 and 3.3.3) for the conditions, where the wave field had been stable.

5.4. Measurement Campaign 2016 at the Large Wind Wave Facility in Marseille

In June 2016 a measurement campaign at the Pytheas facility in Marseille-Luminy, France, took place. Pytheas is a linear wind-wave facility. An advantage compared to the Aeolotron is the linear wave propagation, where no secondary currents are present that are caused by the curvature of the channel in the Aeolotron. At Pytheas, there is a mechanical wave generator, in the following also called paddle, that can be used to modulate the wave field in such a way, that

in the presence of higher wind speeds, there will be a lot of wave breaking in the facility. The purpose of the experiment in Marseille was thus to investigate gas and heat transfer under heavy wave breaking conditions and also to add butanol to the water for some conditions, which can be used to simulate sea water. If butanol is added to the water, the bubble sizes shrink significantly and the total number of bubbles is highly enhanced compared to fresh water [75]. The concentration of butanol used at Pytheas was roughly 55 ppmv.
A direct comparison between heat and gas transfer in the Marseille facility is difficult, as the heat transfer velocities are measured locally at a fetch length of 27 m while the gas transfer velocities are measured globally across the whole water surface, i.e. integrated over all fetch lengths.
Compared to the Aeolotron the maximum wave height at Pytheas is smaller, with maximum significant wave heights of 23 cm [96] at a fetch length of 27 m, where the heat transfer measurements took place. This is an advantage for the thermographic measurements, as the heat flux density will fluctuate less for smaller wave amplitudes (c.f. section 4.1.3).
The individual measurement conditions are listed in table 5.11. Note that values for the friction velocity u_* are only available for the conditions with purely wind driven waves.

Table 5.11.: Measurement conditions at Pytheas in Marseille.

only wind					
date	u_{ref} [m/s]	fetch [m]	paddle freq. [Hz]	mss	u_* [cm/s]
15.06.2016	2.5	27	0	1.12212	0.26879
16.06.2016	3.0	27	0	1.40772	0.34785
17.06.2016	4.0	27	0	1.77204	0.50596
14.06.2016	5.0	27	0	2.21233	0.64827
03.06.2016	10.0	27	0	6.542	1.51789
10.06.2016	12.0	27	0	8.13793	1.92899

paddle conditions with regular wave field				
date	u_{ref} [m/s]	fetch [m]	paddle freq. [Hz]	mss
08.06.2016	6.0	27	1.1	4.63
10.06.2016	12.0	27	0.9	7.656
10.06.2016	8.0	27	0.9	

paddle conditions with enhanced wave breaking				
date	u_{ref} [m/s]	fetch [m]	paddle freq. [Hz]	mss
21.06.2016	6.0	27	1.3	5.004
20.06.2016	10.0	27	1.3	7.571

paddle conditions with enhanced wave breaking and 55 ppmv of butanol				
date	u_{ref} [m/s]	fetch [m]	paddle freq. [Hz]	mss
22.06.2016	6.0	27	1.3	4.594
23.06.2016	10.0	27	1.3	7.492

5.5. Measurement Procedure

Before each measurement, the water surface was carefully cleaned with a skimmer. The skimmer is a device that removes dirt and surfactants from the water surface. For the measurements where surfactants have been added on purpose, of course no skimming took place before the measurements.
After cleaning the water surface, the wind speed was adjusted. Before the actual measurements started, 30 minutes had to elapse in order to achieve stable wind-wave conditions. Once an equilibrium state had established, the ISG (information about this device is given by Kiefhaber [60]) was started to measure the mean square slope of the water surface.
During the whole measurement time, the ambient parameters such as air and water temperature and air humidity were monitored. The wind speed was also measured and for the measurements in the Aeolotron, additionally the velocity of the water flow in the bulk was recorded. However as these parameters, except for the wind speed, are not necessary for the interpretation of the measurements at hand and no unexpected changes in e.g. temperature were detected during the measurements, those values are not listed in the tables.

5.5.1. Thermographic Measurements - Implementation of the Excitation Schemes

For the thermographic measurements, the frame rate of the IR camera was set to 100 Hz. The integration time was 2.5 ms. Depending on wind speed, different frequency ranges were chosen for the excitation with the CO_2 laser. The excitation pattern consisted of 9 or 10 different ground frequencies. The duty cycle of each frequency was 50% and the signal shape was a square function. The square shape yields the advantage, that not only the ground frequency but also the third and fifth harmonic are clearly visible in the spectrum. An exemplary spectrum of the excitation signal and the spectrum from an actual measurement is shown in figure 5.2. Thus, in total 27 to 30 frequencies were probed for each measurement condition.
The measurement started with the smallest ground frequency. For wind speeds up to $u_{ref} = 3$ m/s, the starting frequency was 0.012 Hz. For wind speeds between $u_{ref} = 3$ m/s and 5.8 m/s the starting frequency was 0.024 Hz. For all higher wind speeds, the measurements started with an excitation frequency of 0.049 Hz. The adjustment of the smallest ground frequency is needed, as the

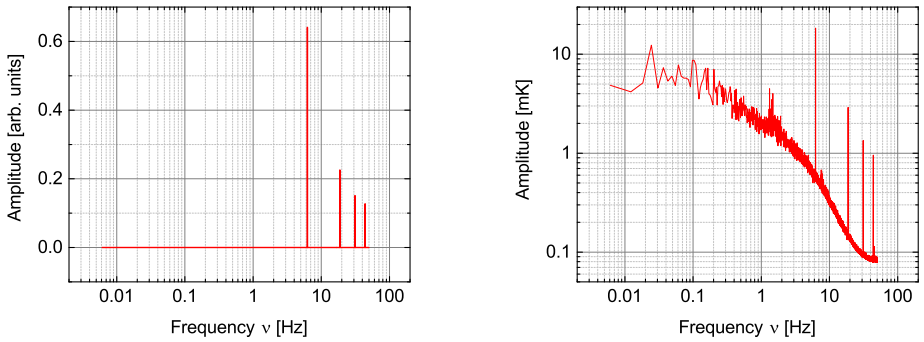

(a) **(b)**

Figure 5.2.: (a): Example of an excitation spectrum of a square function with a duty cycle of 50% and a frequency of 6.25 Hz. The third and fifth harmonic can clearly be seen. (b): Spectrum obtained from the measured temperature response of the water surface as a reaction to the excitation with the spectrum from (a) with the CO_2 laser.

exchange rate of heat is slower at low wind speeds. Thus, to obtain undamped temperature amplitudes, smaller excitation frequencies are needed at lower wind speeds (c.f. section 3.3.2).
The excitation pattern was designed in such a way, that exactly four cycles of the smallest ground frequency are recorded. Additionally, the number of images in a recorded sequence should always be a power of two. This yields a total of 32768 images per excitation frequency for small wind speeds, 16384 images for the intermediate wind speed range and 8192 images for the high wind speeds. Choosing the amount of images in a series to be a power of two ensures that doubling the frequency is possible and still integer numbers for the amount of images per period time of a single excitation cycle are given. Fitting the excitation cycle exactly into the total length of the recorded sequences is of advantage when applying the Fourier transform (c.f. section 6.3). No window function needs to be utilized due to the periodicity of the excitation that fits exactly into the recorded image sequence.
After the measurement with the starting frequency had finished, the ground frequency was multiplied by a factor of four. Then the measurement was repeated and the length of the recorded sequence was kept at 32768, 16384 or 8192 images, respectively. The idea behind this approach is to deposit equal amounts of energy onto the water surface for each excitation frequency. However, it also means that for smaller wind speeds, a measurement takes more time. In total for all probed frequencies, a measurement took 62 minutes for low wind speeds, 31 minutes

for intermediate wind speeds and 18 minutes for high wind speeds. For high wind speeds 18 minutes measurement time instead of 15 minutes measurement time resulted from the use of one additional excitation frequency. The IR camera and the IR laser were synchronized in order to avoid time drifts between the excitation series and the recorded image series during the measurements.
After each excitation frequency the ground frequency was multiplied by four until five frequencies have been measured. Then the first ground frequency (0.012 Hz, 0.024 Hz or 0.049 Hz depending on wind speed) was repeated to allow for the detection of long time drifts during the measurement.
Next, this frequency was doubled. After measuring with the doubled ground frequency, this doubled frequency was multiplied by four again. Then again after each measurement the ground frequency was multiplied by four. This was repeated until in total 10 frequencies were recorded for small and intermediate wind speeds and 11 frequencies were recorded for high wind speeds. Then the first ground frequency was repeated once more, before the measurement for a certain wind condition had finished. In this way, an interleaved excitation scheme was obtained, that could be split into two parts if needed. Splitting reduces the number of frequencies available, however, the measurement time is also cut in in half. Thus, it is possible to try and account for detected long time drifts. Table 5.12 summarizes the different excitation frequencies used for the different wind speed regimes.
Before and after such a series of different excitation frequencies, an offset image series of 2048 images was recorded, where the laser was switched off.
For the measurements in October 2016, additional multifrequency excitation measurements have been conducted after the measurement scheme described above. Two multifrequency excitation measurements per wind speed have been conducted, one with duty cycles of 50% per excitation frequency and one with duty cycles of 75% per excitation frequency (c.f. section 3.3.3). Table 5.12 shows an overview of the excitation frequencies used for each wind speed regime and highlights the excitation frequencies used for the multifrequency excitation measurements, that again depend on wind speed. However, for the multifrequency excitation measurements, 32768 images have been recorded for each wind speed to ensure enough statistics for the measurement, as two frequencies are probed at the same time.

Table 5.12.: Excitation scheme as used for the amplitude damping method. The frequencies used for the multifrequency measurements are marked in blue.

	excitation [#]	**low wind speeds** frequency ν [Hz]	**intermediate wind speeds** frequency ν [Hz]	**high wind speeds** frequency ν [Hz]
ν_1	1	0.012	0.024	0.049
$\nu_2 = 4\nu_1$	2	0.049	0.098	0.195
$\nu_3 = 4\nu_2$	3	0.195	0.391	0.781
$\nu_4 = 4\nu_3$	4	0.781	1.563	3.125
$\nu_5 = 4\nu_5$	5	3.125	6.25	12.5
repetition ν_1	6	0.012	0.024	0.049
$\nu_6 = 2\nu_1$	7	0.024	0.049	0.098
$\nu_7 = 4\nu_6$	8	0.098	0.195	0.391
$\nu_8 = 4\nu_7$	9	0.391	0.781	1.563
$\nu_9 = 4\nu_8$	10	1.563	3.125	6.25
$\nu_{10} = 4\nu_9$	11	not used	not used	25
repetition ν_1	12	0.012	0.024	0.049

6 Data Processing

In this chapter the workflow for the analysis of the infrared image sequences is described. An overview of the different steps of the data processing that are described in the next sections is shown in figure 6.1.

6.1. Selecting the Area of Interest

The pixel values of the recorded images already represent temperatures, as the camera has been calibrated before the measurements. In principle it is necessary to correct the measured temperatures for the emissivity of the objects that are recorded. However, for water the emissivity in the infrared is close to 1 (c.f. section 3.1.2) and the effect of the slightly smaller emissivity is not important for the analysis of the data.
As described in section 3.4 it takes a certain time for the water to heat up to an equilibrium temperature as it advances through the area heated by the IR laser. For the analysis only the equilibrium area is of interest. To select this area in a data sample, a discrete Fourier transform (built-in "FFT" function from MATLAB) is applied to the measured data. Then the temperature amplitude of the lowest laser on-off excitation frequency is chosen (c.f. section 5.5.1 for the exact frequencies used). All temperature amplitudes in cross wind direction are averaged and then a plot of the position in wind direction vs. the averaged cross wind temperature amplitudes is created. From this plot the equilibrium area is selected manually. An example for such a plot can be seen in figure 6.2. This procedure is carried out for each measurement condition.

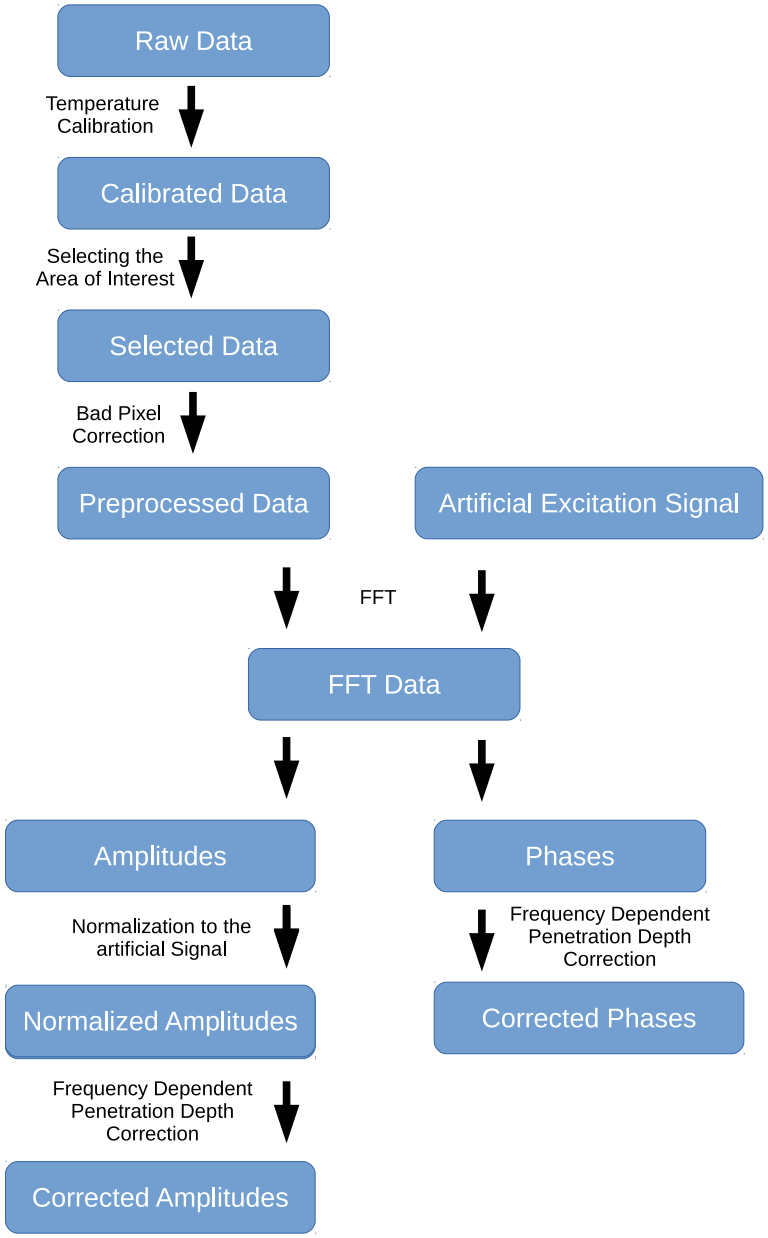

Figure 6.1.: Visualization of the work flow for data processing used to analyse the recorded data.

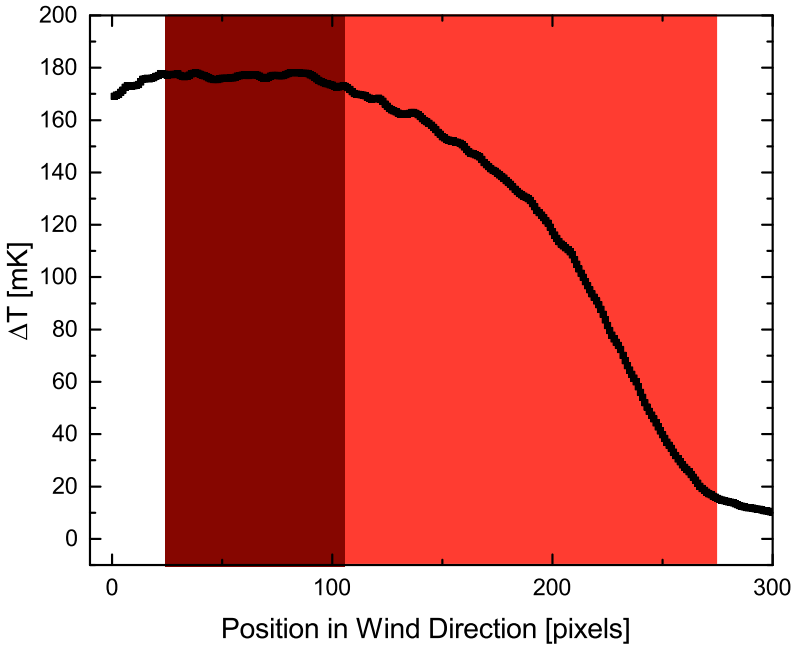

Figure 6.2.: An example for the estimation of the temperature equilibrium region. The data has been recorded at the Pytheas facility in Marseille in June 2016 for a purely wind driven water surface at $u_{ref} = 5$ m/s wind speed. The water surface drift is from the right to the left in the plot. The area that is illuminated by the IR laser is marked in light red. It can clearly be seen, that the water heats up as it travels through the heated area and that it reaches a stable temperature plateau at the end of this area, indicated in dark red. The physical size of the heated area is roughly 50 cm in wind direction. Behind the heated area the temperature decreases again.

6.1.1. Extrapolating to Thermal Equilibrium

Figure 3.14 shows that it takes a certain elongation of the heated area in wind direction in order to reach the thermal equilibrium. In nearly all measurements conducted within this thesis the thermal equilibrium was reached. However, during the sea water campaign for the lower wind speeds, the thermal equilibrium was not reached. In order to be still able to evaluate the data obtained from these conditions, an extrapolation scheme was introduced. A model function is used to describe the measured temperature increase along wind direction. This model function was provided by Clemens Haltebourg, within the scope of his PhD thesis [41]. The model function is

$$T(x) = T_0 + T_1 \exp\left(-\frac{x}{\tau u_0}\right). \tag{6.1}$$

This equation is based on the surface renewal model. The settling time τ and the drift velocity u_0 cannot be distinguished from this equation, but for a least squares fitting procedure with the aim of describing the temperature increase, it is sufficient to substitute the product of τu_0 with one variable ϵ:

$$T(x) = T_0 + T_1 \exp\left(-\frac{x}{\epsilon}\right). \tag{6.2}$$

Using equation 6.2 for a least square fit to the measured temperature increase with the position along wind direction within the heated area allows to estimate T_0, the equilibrium temperature.
Figure 6.3 shows different measurement conditions, where the thermal equilibrium was reached and a condition where it was not reached. For the case where thermal equilibrium was not reached, the fitted curve can be used to extrapolate the temperature increase until it reaches the predicted equilibrium temperature.

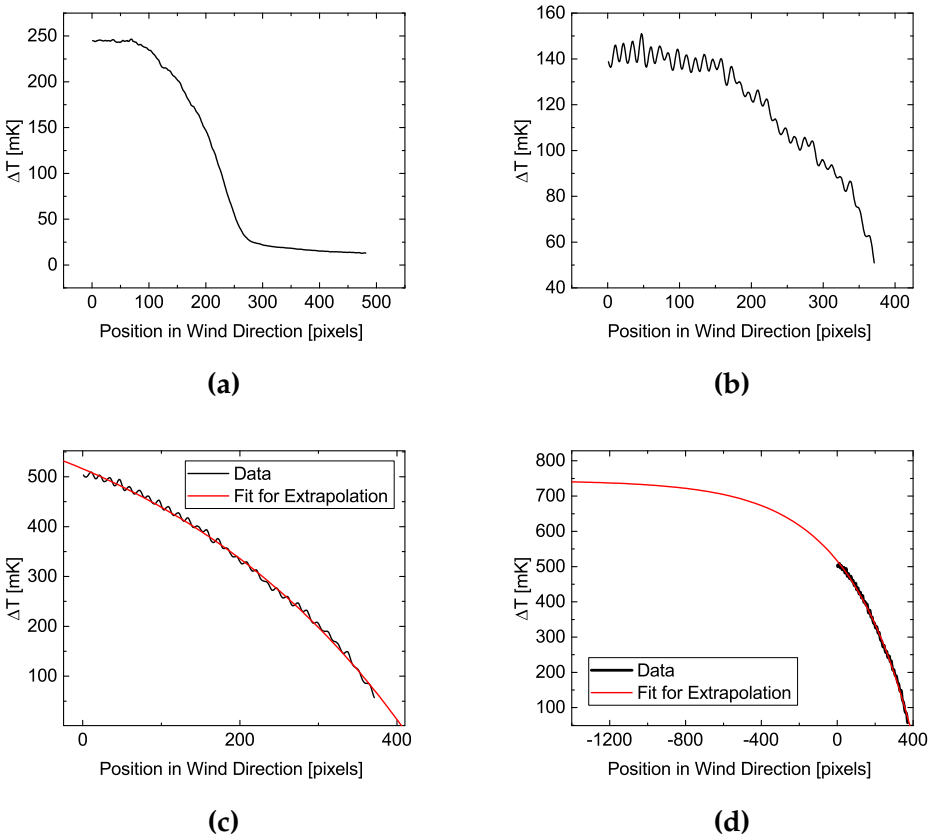

Figure 6.3.: Overview of the development of temperature with position along wind direction when moving through the area heated by the laser. (a) shows a condition where the thermal equilibrium is well reached. The condition was a purely wind driven condition with 4 m/s wind speed at the Marseille facility. Compare also for figure 6.2, to see the start and end position of the laser illumination. (b) shows the situation for a wind speed of 5.8 m/s in the Aeolotron during the sea water campaign in November 2014. At this high wind speed, the thermal equilibrium was reached. (c) shows another condition from the sea water measurement campaign at the Aeolotron, but with a wind speed of only 2.3 m/s. Here the thermal equilibrium clearly could not reached within the size of the heated area. (c) also shows the fit function used for the temperature extrapolation to estimate the equilibrium temperature. (d) shows the same as (c) only with larger range for the spatial coordinate to see, when thermal equilibrium would have been reached. In (b),(c) and (d) ripples are visible on the measured temperature profile. This corresponds to the homogenizer diffraction pattern, c.f. figure 7.2.

6.2. Bad Pixel Correction

The IR camera used for the experiments conducted within the scope of this thesis has many bad pixels. Figure 6.4 (a) shows this very clearly. Most of the dead pixels have either the lowest or the highest intensity value in the possible 16 bit range of the recorded temperature values. It is in principle simple to remove the dead pixels pixel wise, a procedure where the image is not smeared out and therefore keeps its sharpness. However, no structures are investigated within this thesis and small degree of smearing out is no problem, as many pixels are averaged for the analysis anyhow. Therefore the dead pixels are removed simply by applying a 5x5 median filter (built-in "medfilt2" from MATLAB) to the complete image, which removes the dead pixel spikes very efficiently and at the same time only smears out the image slightly. Figure 6.4 (b) show the results of this image smoothing. To apply only a single filter instead of the procedure to remove the dead pixels pixel wise, saves computation time, as a typical sequence consists of around 130000 images for one condition alone. The interested reader can find a description for the pixel wise bad pixel removal in section A.3.

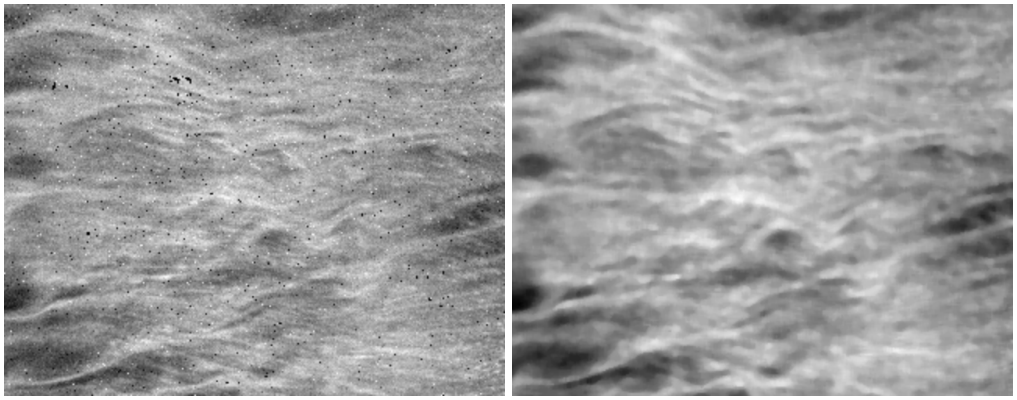

(a) (b)

Figure 6.4.: (a) shows the recorded image only with the temperature calibration applied. (b) shows the application of a 5x5 median filter. It can clearly be seen, that the bad pixels are removed. The decrease in sharpness does not matter for the analysis.

6.3. Analysis in the Fourier Domain

To analyse the temperature amplitudes and to investigate the phase shift between the excitation and the response of the water surface, a discrete Fourier transformation is performed. First the relevant pixels for the Fourier transform are selected as described in section 6.1. Then for each of those pixels the Fourier transform (MATLAB built-in function "FFT") is computed. The mean of the amplitudes and phases for the frequencies of interest is then calculated, as visualized in figure 6.5.

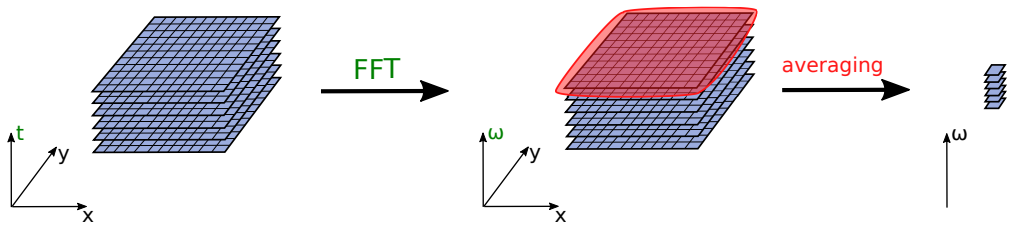

Figure 6.5.: Visualization of the image stack before and after the FFT and the averaging of pixels. Note that the pixels are all in the area of interest, i.e. in the area where thermal equilibrium has been reached for all pixels. The x direction corresponds to the wind direction, the y direction corresponds to the cross wind direction.

6.3.1. Amplitude Damping Analysis

For the amplitude analysis not only the excitation frequencies themselves are considered, but also the third and the fifth harmonic of the excitation frequencies. In this way there are three times more frequencies available for the analysis for the same measurement time. However it has to be taken into account, that the amplitude of the third harmonic is smaller than the amplitude of the ground frequency and that the amplitude of the fifth harmonic is smaller than the amplitude of the third harmonic. This behaviour must be considered for the analysis to prevent misinterpretations concerning the amplitude damping behaviour (c.f. 3.3.2). To correct for this effect, an artificial signal with the shape of the lasers's excitation signal is computed with an amplitude of one. Then the discrete Fourier transform of this signal is calculated along with the Fourier transform of the measurement data. The measured temperature amplitudes are then normalized by means of the amplitudes of the artificial signal's amplitudes at the different frequencies.
After the temperature amplitudes are computed, averaged and normalized, they can be used to obtain the heat transfer velocity. For each laser on-off excitation frequency the corresponding temperature amplitudes of the ground frequency, the third and fifth harmonic are selected. Then a fit is performed from these frequency vs. temperature amplitude sets to estimate the settling time τ for the penetration through the water sided boundary layer according to equation 3.26:

$$c(\omega) = c_0 \cdot (1 + (\omega\tau)^2)^{-\frac{1}{4}} \tag{6.3}$$

An example for such a fit can be seen in figure 6.6.

6.3.2. Analysis of the Phase Shift

To estimate the phase shift between the excitation signal and the temperature response of the water surface the phase of the artificial signal described above is calculated. The phase shift of this artificial excitation signal is then subtracted from the measured phase of the temperature response of the water surface.

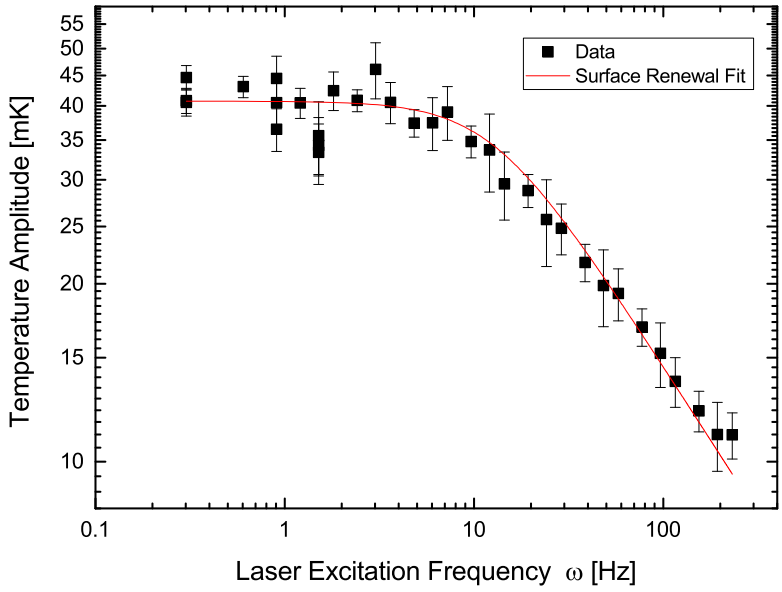

Figure 6.6.: Example for a surface renewal fit used to obtain the settling time. The data has been recorded at the Pytheas facility in Marseille in June 2016 for a purely wind driven water surface at $u_{ref} = 12$ m/s wind speed.

6.4. Correcting for the Penetration Depth of the IR Camera

The IR camera that is used for the experiments in this thesis is sensitive to radiation between 3.4 µm and 5 µm. As described in section 3.1.2 radiation at this wavelength has a certain non-zero penetration depth in water. Accordingly, the IR camera does not only detect radiation from the actual water surface but it measures an integrated signal over the radiation from water elements from the water surface and from water elements down to the penetration depth. By looking at figure 3.3 one can see, that the penetration depth in the wavelength regime from 3.4 µm and 5 µm varies by two orders of magnitude. For the analysis of the measurement data, a mean penetration depth is needed. Therefore the spectrum of a black body with a temperature of 20°C is calculated following Planck's radiation law (c.f. equation 3.1). Figure 3.1 shows such a spectrum for 300 K. The spectrum is normalized and the normalized values are then used as weights for averaging the penetration depth in the wavelength regime between

3.4 µm and 5 µm. The mean penetration depth for this wavelength interval obtained in this way is 39.57 µm.
Figure 6.7 shows a schematic drawing of the temperature profile with water depth, that results from the heating with the CO_2 laser. The temperature am-

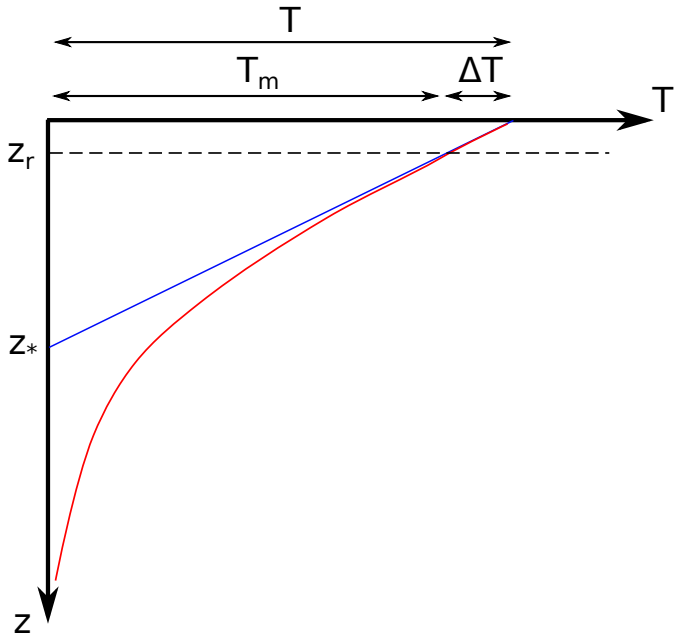

Figure 6.7.: Temperature profile with depth. The penetration depth of the IR camera z_r as well as the thickness of the boundary layer z_* is indicated. The IR camera integrates over all the temperatures from depth smaller than its penetration depth. Modified after Popp [85].

plitudes and the phases that are needed for the interpretation of the physical processes are those directly at the water surface. The temperature T at the water surface in figure 6.7, however, is larger than the temperature T_m measured by the IR camera. According to Popp [85], the measured temperatures can be corrected for the non zero penetration depth of the IR camera by:

$$T(\omega) = T_m(\omega) \cdot \left(1 + z_{pen}\sqrt{\frac{\omega}{D}}\right) \tag{6.4}$$

The corresponding correction for the phase shift is:

$$\phi(0) = \Phi_m \cdot \left(1 - z_{pen}\sqrt{\frac{\omega}{D}}\right) \tag{6.5}$$

Figure 6.8 shows the importance of the correction for the penetration depth in an example for the amplitude correction.

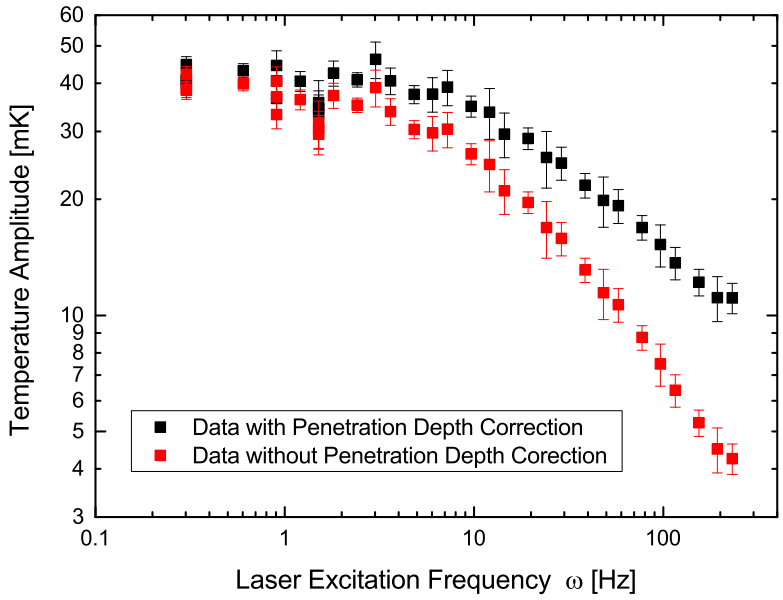

Figure 6.8.: Same data as in figure 6.6, but shown with and without the correction for the non zero penetration depth of the IR camera. The correction is especially important for higher excitation frequencies.

7 Results and Discussion

In the first part of this chapter, the progress concerning the measurement technique is presented and the improved experimental setup is characterized.
The second part is dedicated to the systematic measurements conducted in the Heidelberg wind-wave facility Aeolotron in Summer 2015.
The third part then presents the results obtained from measurements with actual sea water in the Aeolotron, before the fourth part shows the results from a measurement campaign with unknown biological activity in the Aeolotron. The results from the linear wind-wave facility in Marseille are explained in the fifth section. In the sixth section an attempt to differentiate between different gas exchange models with the amplitude damping method is outlined. Finally, a comparison between simultaneously measured heat and gas transfer velocities is discussed in the last section of this chapter.

7.1. Improvements of the Measurement Technique

One of the main subjects of this thesis was the improvement of an existing measurement technique with the focus on the estimation of heat transfer velocities. This section details the achievements, that have been realised in homogenizing the heat flux density through the introduction of diffractive beam homogenizers. The second part of this section discusses uncertainties of the measurement process. Finally, the new excitation schemes, which are only based on the use of two excitation frequencies, are analysed.

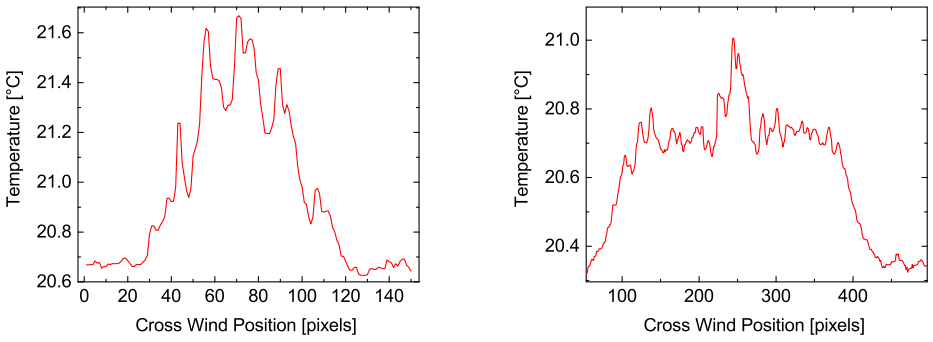

(a) **(b)**

Figure 7.1.: Comparison of two different ways of beam shaping. The intensity distribution in (a) is the result of broadening the initially Gaussian laser intensity profile with a cylindrical lens. (b) shows a much more homogeneous laser pattern, that is created with a diffractive beam homogenizer.

7.1.1. Homogeneity of the Applied Heat Flux Density

Figure 7.1 shows a comparison of the temperature changes at the water surface for different laser intensity profiles at the water surface. The image in (a) clearly shows a Gaussian like intensity distribution, while the image in (b) shows a pronounced plateau that is only interrupted by a small spike in the middle of the plateau. The Gaussian like profile is obtained with the old experimental setup from Popp [85] and Nagel [77] where the Gaussian like laser beam from the CO_2 laser is first broadened with a cylindrical lens and then moved forwards and backwards by means of a moving mirror perpendicular to the extension of the broadened laser line. Thus the Gaussian intensity profile is still present, as the beam has simply been broadened and not reshaped. Homogeneity of the resulting intensity distribution is consequently only given in the scanning direction of the moving mirror. However, for the intensity distribution as shown in figure 7.1 (b), the homogeneity is given in two dimensions. Figure 7.2 shows an image of the two dimensional intensity distribution at the water surface as recorded with the IR camera for a calm water surface. The bright spot in the middle can be recognized directly. This corresponds to the intensity peak in the middle of the right profile shown in figure 7.1. This bright signature is the remaining intensity excess of the zero diffraction order of the diffractive beam shaping process, that is not completely suppressed with this diffractive beam homogenizer model (Holo/Or HM-271-A-Y-A, c.f. section 4.5). Additionally, the diffraction pattern can be seen in figure 7.2. The intensity distribution is

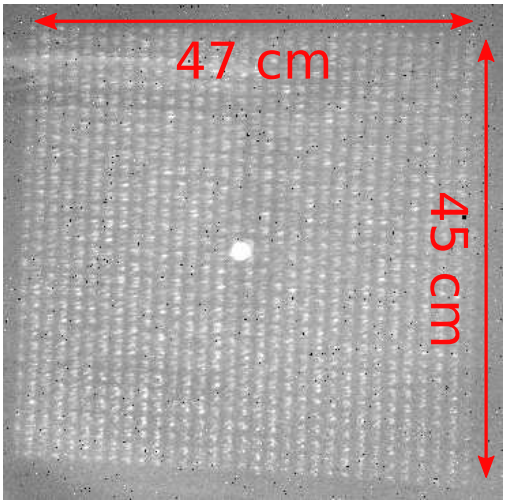

Figure 7.2.: Intensity distribution on the water surface as created with the diffractive beam homogenizer Holo/Or HM-271-A-Y-A. The diffraction pattern is clearly visible. The bright spot in the middle is the 0^{th} diffraction order that is not suppressed completely.

thus not perfectly uniform, but it is symmetric. By looking again at the right profile in figure 7.1, ripples can be seen along the intensity plateau. The data for this profile was taken for a water surface that is only moving slowly. The diffraction pattern as seen in figure 7.2 then smears out due to the water surface drift and only those ripples remain as artefacts in the data. In this way the influence of the remaining features from the diffraction pattern don't affect the measurement significantly. Anyway, the homogeneity is further improved by another diffractive beam homogenizer model, the Holo/Or HH-211-A-Y-A. The intensity distribution at the water surface for this model is shown in figure 7.3. It can clearly be seen, that the intensity distribution looks much more random and that the intensity peak from the zero diffraction order is now suppressed.
The symmetry of the intensity distribution is important, is the water surface drift does not run perfectly parallel to the alignment of the applied heat flux density pattern. In the case of Popp's and Nagel's setup a water flow that does not run parallel to the scanning axis of the moving mirror would mean that the water experiences different heat flux densities along its way through the intensity profile. This can easily cause variations of 50% due to the Gaussian intensity distribution. In a linear wind-wave facility like Pytheas at Marseille (c.f. section 4.2), this might not be a problem. For field measurements with more complex flow patterns it is very challenging if not impossible to assign a distinct heat flux density to a measured temperature increase for a Gaussian intensity distribution. Thus, the introduction of diffractive beam homogenizers

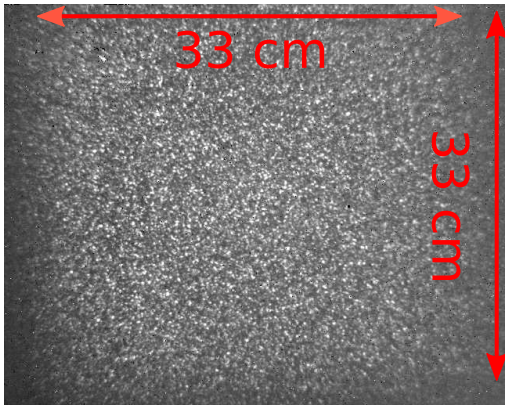

Figure 7.3.: Intensity distribution on the water surface as created with the diffractive beam homogenizer Holo/Or HH-211-A-Y-A. In comparison to the Holo/Or HM-271-A-Y-A (c.f. figure 7.2) no intensity spike from the 0^{th} diffraction order is visible. Additionally, the intensity distribution is much more random and no clear diffraction pattern is visible.

is an important improvement for the application of the measurement in future field campaigns, but it is also beneficial in the Aeolotron where the surface drift of the water surface runs on a curved track due to the geometry or the facility (c.f. section 4.1).

7.1.2. Measurement Uncertainties and Error Discussion

There are mainly two types of uncertainties that have to be considered for the thermographic measurements at the air-water interface: temporal and spatial uncertainties.
Spatial errors are primarily caused by inhomogeneities in the applied heat flux density. The improvements to minimize these inhomogeneities in the present experimental setup are explained above (c.f. section 7.1.1). For the experiments at the Aeolotron another source for a spatial error is given by the gradient in the applied heat flux density j_{heat} along wind direction (c.f. 4.1.3). However, the influence of this gradient on the measured temperature differences ΔT is difficult to quantify. If ΔT can adapt quickly to the gradual changes in j_{heat}, then the error is smaller than the total gradient of the heat flux density along the complete intensity profile as calculated to be approximately 10% in section 4.1.3. Spatial errors caused by the inhomogeneity of the heat flux density due to the remaining diffraction pattern at the water surface can be quantified by calculating the

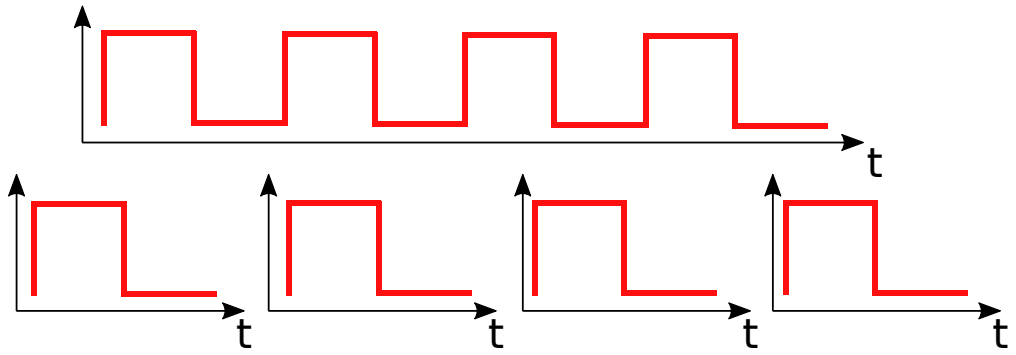

Figure 7.4.: Comparison of different excitation schemes. The upper case probes the water surface four times within one continuous image sequence. The lower case shows four individual image sequences that only contain one excitation cycle each.

standard deviation of the temperature amplitudes between neighbouring pixels in the recorded images.
The most relevant temporal errors are power fluctuations of the laser that provides the heat flux density and of waves that modulate the distance between the diffractive beam homogenizer and the water surface and thereby modulate the effective heat flux density locally. The latter effect is again difficult to quantify. In section 4.1.3 it is estimated that the heat flux density changes only by 1% for the complete cycle of a sinusoidal wave. However, it is also shown that extreme variations of up to 48% can be reached for extreme amplitudes of the waves.
In section 5.5.1 the implementation of the amplitude damping excitation scheme is described. For each frequency one continuous sequence of exactly four complete cycles of the excitation is applied. This approach yields the advantage of a better frequency resolution, as the smallest frequency that can be resolved in a measurement ν_{min} is given by the duration of the recorded sequence $T_{measurement}$:

$$\nu_{min} = \frac{1}{T_{measurement}} \tag{7.1}$$

Thus ν_{min} is smaller if four cycles of the excitation signal are recorded in one sequence than if four individual sequences containing only one excitation period are recorded. The difference of the two excitation schemes is visualized in figure 7.4. However, the drawback is that no standard deviation between individual excitation cycles can be calculated and thus no temporal variation can be quantified. In order to find out how strong the lack of this temporal error affects the measurement accuracy an exemplary sequence from the measurements conducted in October 2016 with a wind speed of 4.7 m/s was analysed. The recorded sequences of each excitation frequency were split into four parts to

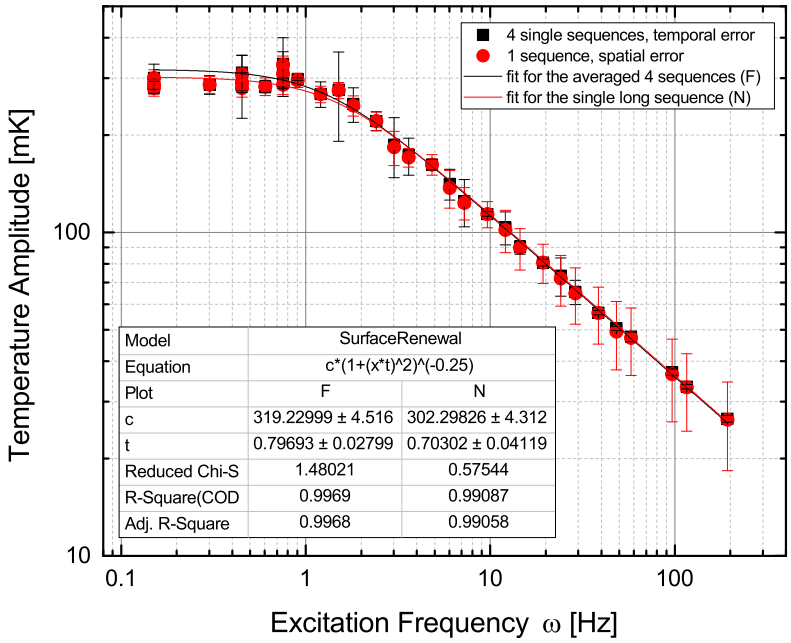

Figure 7.5.: A comparison of the amplitude damping analysis for the spatial and the temporal error. It can be seen that the temperature amplitudes at high excitation frequencies are stronger affected by the spatial error than the temperature amplitudes at low excitation frequencies. On the other hand the temperature amplitudes at high excitation frequencies are very insensitive to temporal uncertainties.

achieve a situation comparable to four individually measured sequences. Figure 7.5 shows the differences between this approach and the approach with one long sequence. The error for the single long sequence is given by the standard deviation between the temperature amplitudes of pixels in the area where the thermal equilibrium is established (c.f. section 3.4). It therefore mainly represents spatial uncertainties. The error for the four shorter sequences is given by the standard deviation between the temperature amplitudes of the individual sequences and thus represents the temporal fluctuations during the measurement. Note that for each sequence the mean of the temperature amplitude for all pixels in the thermal equilibrium area has been computed and that the temporal standard deviation is thus the temporal error of the spatial mean of the four sequences. A close look at figure 7.5 reveals that the spatial error becomes increasingly important the higher the excitation frequency. In contrary temporal errors are more relevant for lower

frequencies, although not all small frequencies in figure 7.5 are equally affected by the temporal fluctuations. Applying a fitting procedure according to section 6.3.1 to the data in figure 7.5 yields heat transfer velocities of 151 ± 3 cm/h and 161 ± 5 cm/h for four single sequences and one long sequence, respectively. But looking at the line representing the fitted curve in figure 7.5 it is obvious, that at high frequencies the spatial error does not affect the measurement accuracy, as there are many measurement points for the damped frequency regime. In this regime molecular diffusion is the dominant process. It has been shown in section 3.3.2 that independent of the exchange model used, the slope in the damped amplitude regime is given by $\omega^{-1/2}$. Since all the data points in the damped regime lie on a curve with the same curvature, the error of individual data points does not affect the overall accuracy of the fitting procedure much. The difference between the transfer velocities listed above for the analysis of four single sequences and for one long sequence is relatively small and it is hard to tell which one is correct. For the measurements conducted within the scope of this thesis the advantage of the better frequency resolution was thus chosen and the approach with one long sequence per excitation frequency was applied for the measurements. It can also be argued that a temporal error - at least for high frequencies - is accounted for by the fact that the individual frequencies are not recorded at the same time and thus temporal fluctuations between different frequencies are given for the damped amplitude regime.
Figure 7.6 explains why temperature amplitudes for higher excitation frequencies are stronger affected by spatial inhomogeneities than excitations with low frequencies. The figure shows the temperature development along the area on the water surface that is heated by the laser. The water flows from right to left in the image and heats up as it flows through the heated area. For the case shown in (a) and (b) a low excitation frequency of 0.024 Hz is applied. The water can travel through the heated are within the half cycle of the excitation where the laser is turned on. It thus heats up steadily and the small ripples from the diffraction pattern smear out and become of minor importance compared to the overall temperature increase. In (c) and (d) the same situation with a higher excitation frequency of 6.25 Hz is shown. In this case the water surface does not heat up constantly, but heats and cools periodically due to the high frequency during its journey through the heated area (c.f. section 3.3.2). As a result the temperature distribution shown in figure 7.6 (c) is a smeared out snapshot of the laser intensity distribution shown in figure 7.3. The local intensity fluctuations are much stronger in this case as the total temperature increase is significantly lower than for low excitation frequencies. As the heating time is much shorter for the high excitation frequencies, also the influence of individual intensity spikes is much stronger, because not many of them are averaged within the half cycle of

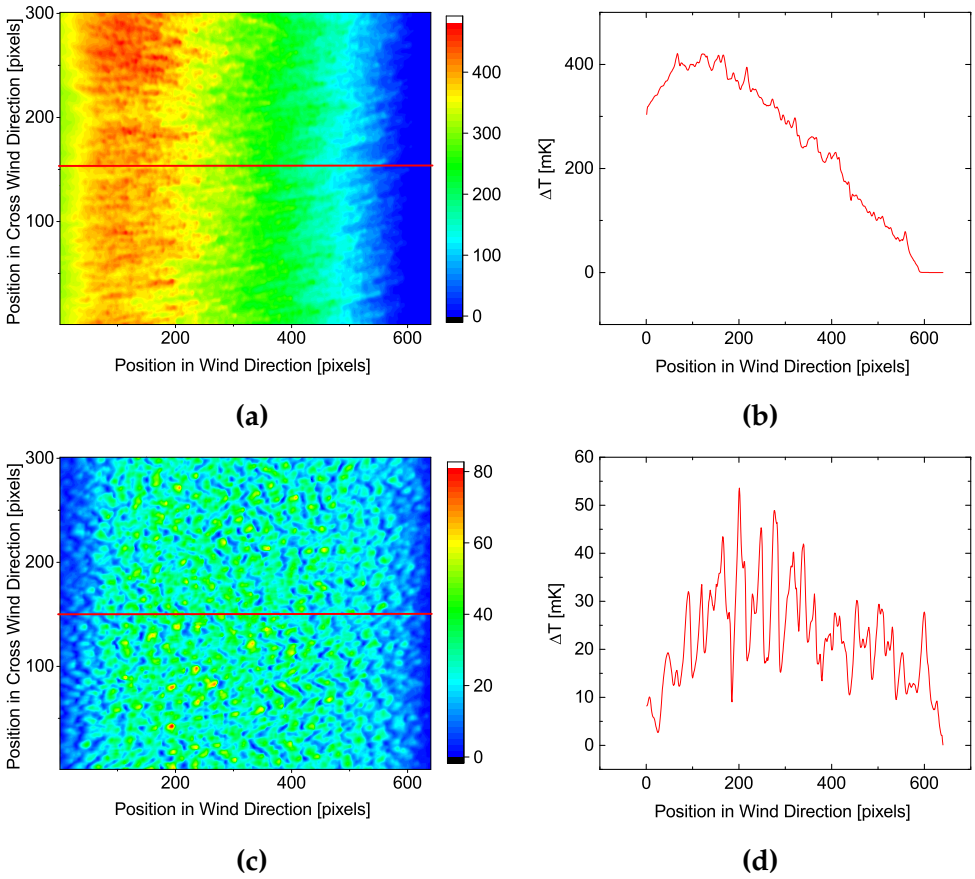

Figure 7.6.: Different influence of spatial inhomogeneities in the laser intensity profile at the water surface for the temperature amplitudes obtained for a low (a) and a high (c) excitation frequency. (b) and (d) show corresponding intensity profiles along the x direction (wind direction) of the two dimensional intensity distributions in (a) and (c), as indicated by the red lines. It can clearly be seen that the temperature amplitudes at high excitation frequencies are effected stronger by spatial inhomogeneities of the heat flux density. For low excitation frequencies the overall temperature increase is larger and small variations in the heat flux density only cause small ripples in the temperature profile.

the excitation where the laser is turned on. As described above the spatial error only slightly affects the measurements with the amplitude damping approach, as there are many data points available in the damped frequency regime. However, for the new excitation schemes the strong spatial variation is a problem, since only one frequency in the damped regime is used and thus only one data point is available. Anyway, spatial inhomogeneities of the diffractive beam homogenizer are not the subject of investigation in this thesis, but rather the transport of heat through the aqueous boundary layer. Looking again at figure 7.6 (d) a slight increase of the temperature along the complete heated area is visible and averaging over neighbouring pixels can be used to smoothen this increase and to reduce the ripples in the profile. This average temperature increase is precise enough for the estimation of the transfer velocity since the spatial resolution for low excitation frequencies is lower anyway, as can clearly be seen from figure 7.6 (a) and (b). The temperature amplitude at the high frequency for the new excitation schemes is needed for the estimation of the heat flux density (c.f. section 3.3.1). As only an average temperature amplitude is available for the estimation of j_{heat} as just described, the error of the heat flux density is estimated by the power fluctuations of the used laser as given by the manufacturers data sheets listed in section 4.4.
Figure 5.2 already showed a temperature amplitude spectrum from a measurement. It is clearly visible in the spectrum, that the measured signal not only contains a signal from the excitation due to the laser but that there is also a noise signature in the spectrum. Short offset sequences containing 2048 images, where the laser is turned off have been recorded for each measurement condition. However, in order to have the same frequency resolution as for the image sequences with laser excitations, a part of the unheated water surface, next to the area illuminated by the IR laser, was selected in order investigate the influence of the offset spectrum carefully. Figure 7.7 shows the temperature amplitudes for these offset sequences and different wind speeds for clean water conditions at the excitation frequencies. It can be seen, that there is a lot of scatter in the data even for a fixed wind speed. To compare the amplitudes of the noise with the measurement signal from actual excitations with the IR laser, as an example figure 7.8 shows a comparison of temperature amplitudes from a measurement with a wind speed of 2.3 m/s with the noise amplitudes subtracted and without subtraction of the noise amplitudes. Analysing the deviation of the amplitudes with noise subtraction shows that over all excitation frequencies used in this example, the amplitudes with noise subtraction area on average only $(2 \pm 1)\%$ smaller than the amplitudes without noise subtraction. Additionally, the uncertainty of the amplitudes caused by the laser excitation, as in indicated by the error bars in figure 7.8, is much larger than the offset signal. In order to

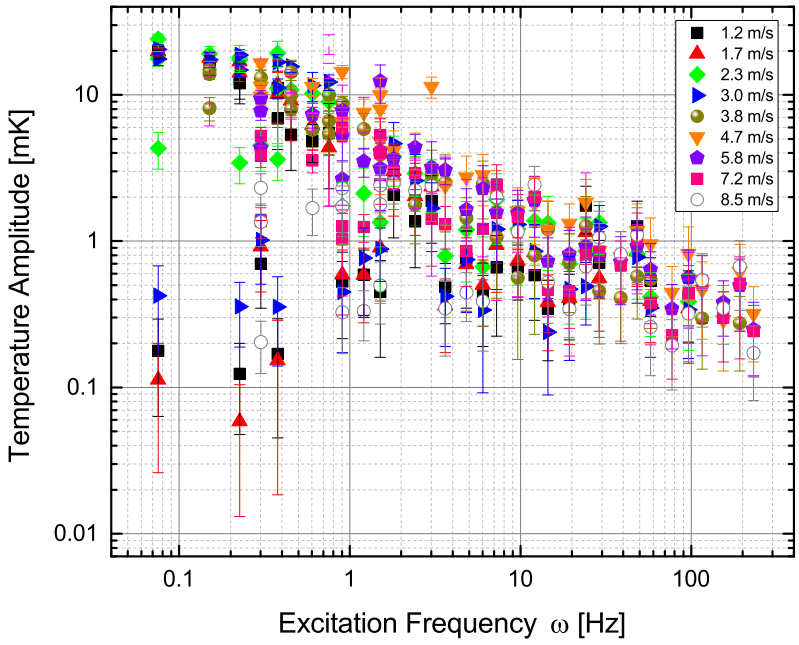

Figure 7.7.: Temperature amplitudes for excitation frequencies obtained from offset sequences where the laser is constantly turned off. The image sequences were recorded for different reference wind speeds. It can clearly be seen, that there is a lot of scatter in the measured temperature amplitudes even for a fixed wavelength and wind speed.

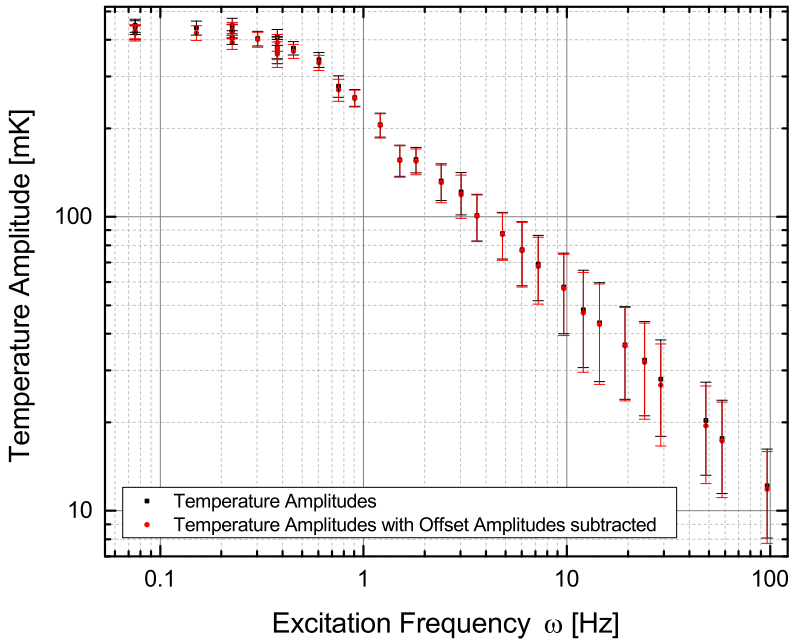

Figure 7.8.: Comparison of temperature amplitudes with and without subtraction of the offset temperature amplitudes. Data obtained from clean water conditions and a reference wind speed of 2.3 m/s. The error bars are much larger than the difference between offset corrected temperature amplitudes and temperature amplitudes without offset correction.

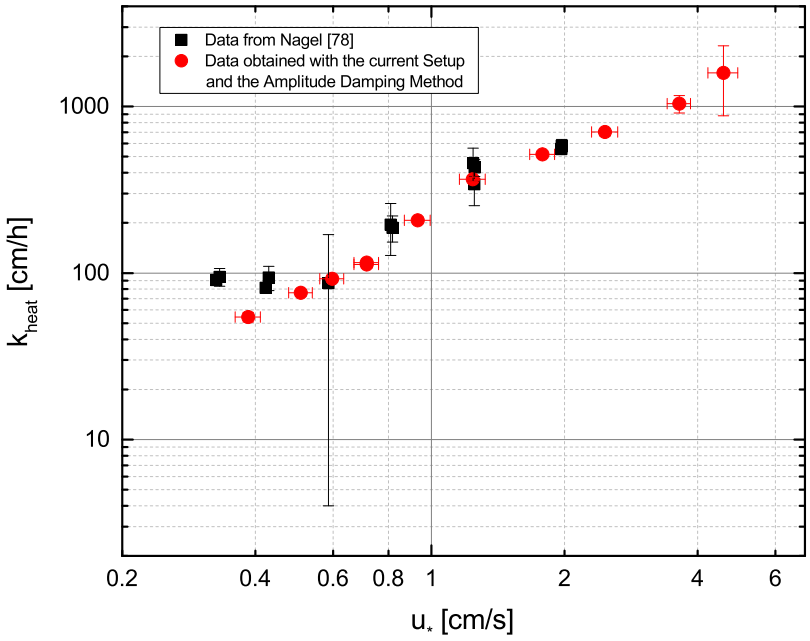

Figure 7.9.: Heat transfer velocities for different friction velocities. The measurements with the actual setup with a diffractive beam homogenizer are shown in red, while the measured values from the old setup from Nagel [78] are shown in black. It can be seen, that both measurements are in agreement with each other, for friction velocities u_* larger than 0.5 cm/s and that the measurement error of the current setup is smaller than the measurement error from Nagel's experiments.

save memory and computation time the subtraction of the noise amplitudes has therefore been neglected for the analysis of the measured data.
Figure 7.9 shows a comparison of the results obtained with the actual experimental setup and the error estimation according to the arguments given above and the results obtained with the earlier version of the experimental setup as used by Nagel [78]. The improved measurement accuracy can clearly be seen by the smaller error bars. The deviations between the two measurements for low friction velocities is explained in section 7.2.1.

7.1.3. New Excitation Pattern

The improvement of the homogeneity of the heat flux density and the accompanying improvement in the accuracy of the amplitude damping method allows for the first time to do the analysis via the ΔT method, as described in section 3.3.1. Only two frequencies are analysed, a high frequency to determine the heat flux density and a low frequency to determine the temperature difference between the unheated water and the heated water in the thermal equilibrium region of the heated area (see section 6.1.1).
In section 5.5.1 the excitation scheme has been presented. For the analysis of the recorded image sequences with the ΔT method two frequencies have been selected from the measured image sequences of the amplitude damping method. Following the classification of frequencies given in table 5.12, frequencies ν_1 and ν_5 have been used, i.e. for low wind speeds 0.012 Hz and 3.125 Hz, for intermediate wind speeds 0.024 Hz and 0.049 Hz and for high wind speeds 0.049 Hz and 12.5 Hz. Figure 7.10 shows a comparison of the results obtained with the amplitude damping analysis and with the ΔT analysis for the clean water conditions in the Aeolotron in 2015. Figure 7.11 shows a direct comparison of the results from both methods. As can be seen from the linear fit in figure 7.11, the results from the ΔT method and from the amplitude damping method are in perfect agreement, with a deviation of $(0.3 \pm 0.5)\%$. The data underlying figure 7.10 was taken during controlled laboratory conditions with constant wind speed and clean water surface (see section 5.1). The data is also listed in table 7.1.
The measurement time for the ΔT method is already significantly reduced compared to the amplitude damping method, but still the two excitation frequencies are probed consecutively. As mentioned earlier, this can cause biases in the data, if the boundary conditions are rapidly changing. The temperature difference ΔT and the heat flux density j_{heat} are then measured for different boundary conditions. To overcome this disadvantage the new multifrequency excitation introduced in section 3.3.3 was implemented and tested. The measurement time was set to five minutes for one continuous image sequence independent of the wind speed. Depending on wind speed, however, different excitation frequencies were chosen, as highlighted in table 5.12. For some conditions of the measurements carried out in October 2016 (c.f. section 7.4) at the Aeolotron in Heidelberg a comparison of all measurement schemes presented in this thesis was conducted. Temperature amplitude spectra obtained from the multifrequency excitation with duty cycles of 50% and 75% for the excitation frequencies are shown in figure 7.12. The theoretical spectra of the signals that control the IR laser are shown in figures 3.12 and 3.13. In section 3.3.3 a slight increase of the amplitudes for both, the high and the low excitation frequency, have been

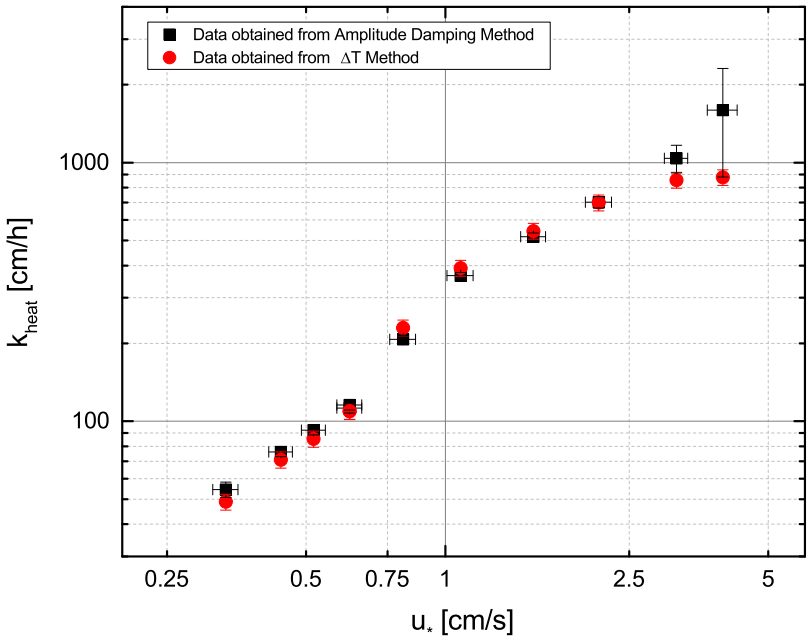

Figure 7.10.: Comparison of the results obtained with the amplitude damping method and the ΔT method. Data recorded during clean water conditions in the Aeolotron. For all friction velocities a good agreement between the two measurement schemes is given.

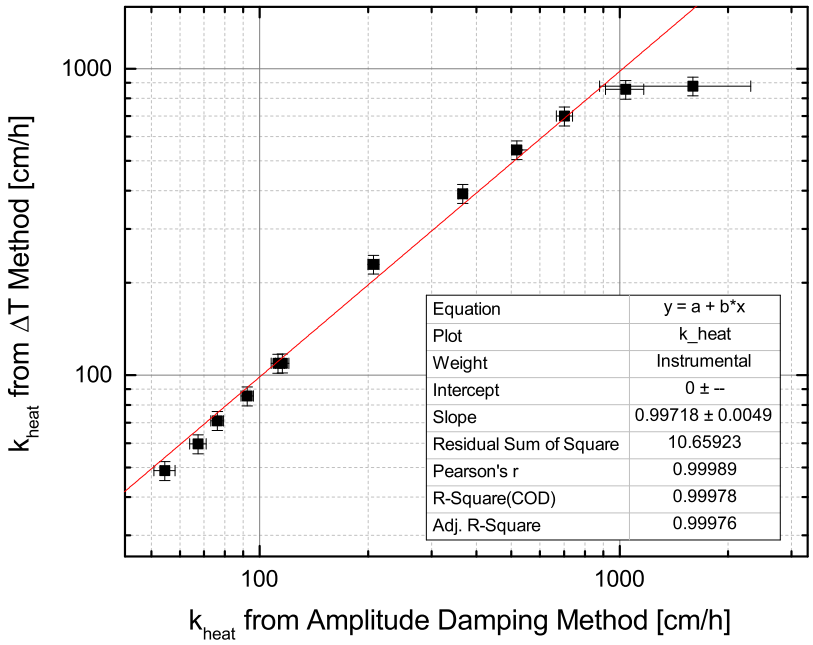

Figure 7.11.: Comparison of the results obtained from the amplitude damping method and ΔT method. The underlying data was taken during clean water conditions in the Aeolotron. The linear fit reveals deviations of only $(0.3 \pm 0.5)\%$ between the two measurement schemes.

Table 7.1.: Comparison of the results from the ΔT method and the amplitude damping method for clean water conditions.

date	u_{ref} [m/s]	u_* [cm/s]	k_{heat} [cm/h] Amp. damping	k_{heat} [cm/h] ΔT method
19.06.2015	1.2	0.335 ± 0.021	54 ± 4	49 ± 3
19.06.2015	2.3	0.441 ± 0.026	76 ± 3	71 ± 5
19.06.2015	3.8	0.621 ± 0.038	112 ± 5	109 ± 8
19.06.2015	4.7	0.810 ± 0.052	207 ± 7	230 ± 16
19.06.2015	7.2	1.552 ± 0.097	517 ± 17	543 ± 38
19.06.2015	9.7	3.164 ± 0.184	1039 ± 127	856 ± 60
22.06.2015	1.7		67 ± 4	60 ± 4
22.06.2015	3.0	0.519 ± 0.031	92 ± 4	85 ± 6
22.06.2015	3.8	0.621 ± 0.038	115 ± 5	109 ± 8
22.06.2015	5.8	1.079 ± 0.070	366 ± 10	391 ± 28
22.06.2015	8.5	2.149 ± 0.140	703 ± 36	700 ± 49
22.06.2015	11.3	3.983 ± 0.297	1596 ± 717	877 ± 61

calculated for a duty cycle of 75% in comparison to a duty cycle of 50%. From the measurement an increase of 9% for the frequency of 0.049 Hz and an increase of 6% for the frequency of 25 Hz are obtained. Table 7.2 shows a detailed comparison of the different measurement schemes. The table lists the different values obtained for the equilibrium temperature increase of the ΔT method, and for the two different multifrequency implementations with different duty cycles of 50% and 75% for each excitation frequency (c.f. section 3.3.3). Note that the measured heat flux densities are larger than the heat flux densities estimated from geometrical considerations in section 4.1.3. This is due to the fact that for the measurements in October 2016 the size of the laser intensity profile was reduced by means of a spherical focusing lens in order to fit into the field of view of the IR camera, that used a 50 mm lens instead of the 28 mm lens used for all other experiments in the Aeolotron (see also figure 7.2 and figure 7.3 for the extensions of the intensity profile at the water surface). By comparing the results in table 7.2 it can be seen, that the results obtained by the amplitude damping method are in good agreement with the other methods. Although the measurement error and therefore the accuracy of the amplitude damping method is slightly better compared to the other measurement schemes, the difference is not large. In contrast to the advantage of a slightly better measurement accuracy, the measurement duration of the amplitude damping method is worse by a factor of

Table 7.2.: Comparison of the different measurement schemes.

Parameters as estimated by the ΔT Method			
u_{ref} [m/s]	ΔT [mK]	j_{heat} [W/m^2]	k_{heat} [cm/h]
3.8	544 ± 5	1351 ± 95	107 ± 8
4.7	357 ± 3	1430 ± 100	173 ± 12
5.8	145 ± 4	1389 ± 97	413 ± 29
Parameters as estimated by the multifrequency method with 50% duty cycle			
u_{ref} [m/s]	ΔT [mK]	j_{heat} [W/m^2]	k_{heat} [cm/h]
3.8	276 ± 8	688 ± 48	107 ± 8
4.7	193 ± 10	742 ± 52	166 ± 12
5.8	74 ± 5	671 ± 47	391 ± 28
Parameters as estimated by the multifrequency method with 75% duty cycle			
u_{ref} [m/s]	ΔT [mK]	j_{heat} [W/m^2]	k_{heat} [cm/h]
3.8	290 ± 9	717 ± 50	106 ± 8
4.7	198 ± 13	765 ± 54	166 ± 12
5.8	81 ± 5	710 ± 50	378 ± 27

Comparison of the results obtained with the different measurement schemes				
u_{ref} [m/s]	Amp. Damp. [cm/h]	ΔT Method [cm/h]	Multifreq. 50% [cm/h]	Multifreq 75%[cm/h]
3.8	115 ± 4	107 ± 8	107 ± 8	106 ± 8
4.7	161 ± 5	173 ± 12	166 ± 12	166 ± 12
5.8	375 ± 15	413 ± 29	391 ± 28	378 ± 27

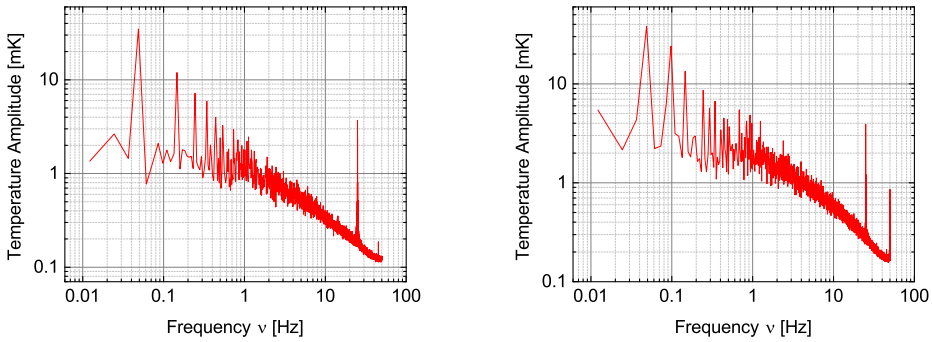

Figure 7.12.: Measured amplitude spectra for the multifrequency excitation scheme. The theoretical spectra of the excitation signal are shown in figure 3.12 and figure 3.13. The excitation spectrum in (a) corresponds to a duty cycle of 50% for the excitation signal and the spectrum in (b) corresponds to a duty cycle of 75% of the excitation signal.

4 to 12, depending on wind speed, compared to the multifrequency excitation schemes. For all the results listed in table 7.2 the measurement duration for the multifrequency scheme was five minutes. An amplitude damping measurement at a wind speed of 3.8 m/s lasted for roughly one hour, for a wind speed of 4.7 m/s the measurement took 31 minutes. For a wind speed of 5.8 m/s the measurement was completed within 18 minutes (c.f. section 5.5.1).

7.2. Systematic Study of Heat Transfer Rates under Controlled Conditions

Many measurements were conducted for this thesis. To compare them and to find out, which effects can be attributed to which environmental circumstance a very thorough study with many different boundary conditions was carried out between June and August 2015 under carefully controlled laboratory conditions. The results from these measurements serve as the basis for comparison with more complex experimental conditions, where for example biological activity is involved.
For all systematic measurements conducted within the scope of this thesis, the amplitude damping method was used, except for the measurements with sea

water. For the sea water measurements additional corrections were needed, that can be implemented more effectively for the ΔT method (c.f. section 6.1.1). These corrections and the necessity for their application are explained in section 7.3.

7.2.1. Clean Water over an Extended Wind Speed Range

The measurements with deionized water and no added surfactants serve as a comparison with old measurements of the heat transfer velocity from Nagel [77, 78], to check if the boundary conditions in the Aeolotron have changed since the last measurements. This is important, as any comparison with data from former measurements from the Aeolotron are based on the assumption that the environment has not changed. However, the wind speed range has been extended for the measurements of this thesis compared to Nagel's measurements. Nagel used reference wind speeds of 1.5 to 8.65 m/s for her measurements. For the measurements for this thesis, wind speeds between 1.3 to 11.3 m/s were used.
As mentioned in section 4.1, environmental parameters like air and water temperature and air humidity can be measured in the Aeolotron. This was also done for the present measurements. However, since the temperatures for air and water are nearly the same and are close to the room temperature of 20°C and the air humidity in the closed Aeolotron is always close to 100%, these values will not be listed in the following sections.
Figure 7.10 shows the measured heat transfer velocities against the different friction velocities. The development of k_{heat} with wind speed is shown in figure 7.17 and will be discussed in section 7.2.3. Figure 7.13 shows the correlation between the heat transfer velocity and the mean square slope (mss) of the water surface. In this double logarithmic representation the slope of k_{heat} with mss does not change, except for the highest wind speeds. This means, that in the case of a clean water surface, mss might be a suitable parameter for parametrizing the heat transfer. However, this is not the case for a water surface that is contaminated by surface active material (see section 7.2.3).
The comparison with Nagel's measurements is shown in figure 7.9. The data points from Nagel's experiments and from the present study are in good agreement except for the lowest wind speeds, which correspond to friction velocities smaller than 5 cm/s in the figure. The heat transfer velocities from Nagel's measurements for these low wind speeds stay constant and don't decrease any further with wind speed or friction velocity. A potential explanation is given by Nagel herself [78]. From equation 3.20 it can be seen directly, that the heat transfer velocity will be overestimated if the temperature increase is estimated

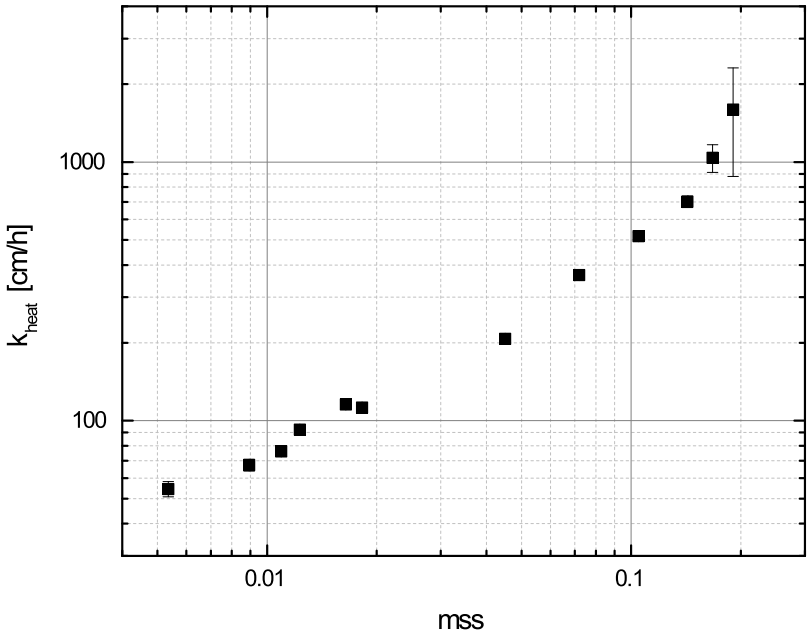

Figure 7.13.: Measured heat transfer velocities against the simultaneously measured mean square slope values for clean water conditions in the Aeolotron.

too small from the measurement. This happens, when the size of the area on the water surface, that is heated, is too small (c.f. section 3.4).
The extension of the measurement to higher wind speeds showed that k_{heat} continues to increase with the friction velocity. According to equation 2.57 the correlation between the friction velocity u_* and the heat transfer velocity k_{heat} is given by

$$k \propto \frac{u_*}{\beta} Sc^{-n}. \tag{7.2}$$

The slope is thus given by

$$\frac{1}{\beta} Sc^{-n}. \tag{7.3}$$

From the present measurement it cannot be concluded if a change in slope is caused by a change in the Schmidt number exponent n or by changes in the dimensionless momentum resistance β. However, it is possible to detect when the slope changes as a whole. In figure 7.9, a change in slope is only observed in an intermediate wind speed range for friction velocities between 0.8 cm/s

and 1.2 cm/s. As the figure is plotted double logarithmically, a change in slope in equation 7.2 is visible as a line with constant slope but shifted offset in the figure. This corresponds roughly to the transition zone defined by Schnieders [94], where microscale wave breaking starts to emerge and waves start to grow. This can also be seen in figure 7.14, where the mean square slope increases strongly at these friction velocities.

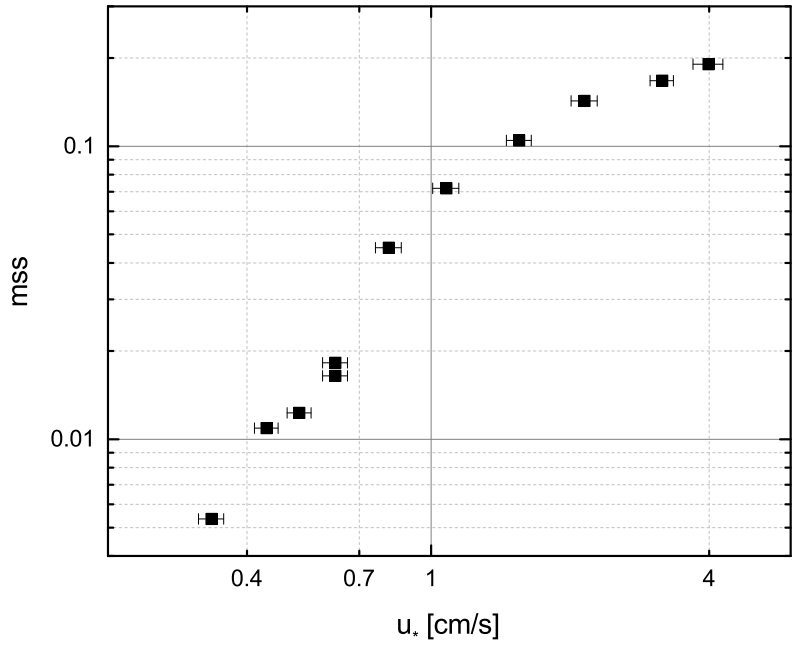

Figure 7.14.: Mean square slope of the water surface against the friction velocity for clean water conditions in the Aeolotron.

7.2.2. Fetch Dependency of Heat Exchange

The fetch dependency is a very important subject of research. It affects all measurements of gas exchange in linear facilities, as the fetch in such a facility is limited. On top of that, a measurement in a linear facility averages over many different fetches, so that it is important to know how the exchange velocity varies with fetch. For gas exchange this dependency is at the moment impossible to measure, however, for heat exchange it can be done quite well with the controlled

flux method (c.f. chapter 3).
Details about the fetch variation in the Aeolotron can be found in section 4.1.1. For most of the conditions it was possible to achieve an accuracy of ±10 cm for the fetch length.
The momentum balance method from Bopp [9] estimates the global friction velocity across the whole water surface in the Aeolotron. The friction velocity that can be calculated by Bopp's momentum balance method therefore cannot distinguish between different fetch lengths. Other measurements to estimate the friction velocity locally exist, see Garbe [37] and there are plans to implement them in future measurement campaigns. For the measurements at hand, these local measurements were not available.
Figure 7.15 shows the measured heat transfer velocities for different fetch lengths and different wind speeds. The corresponding mean square slope values are shown in figure 7.16.

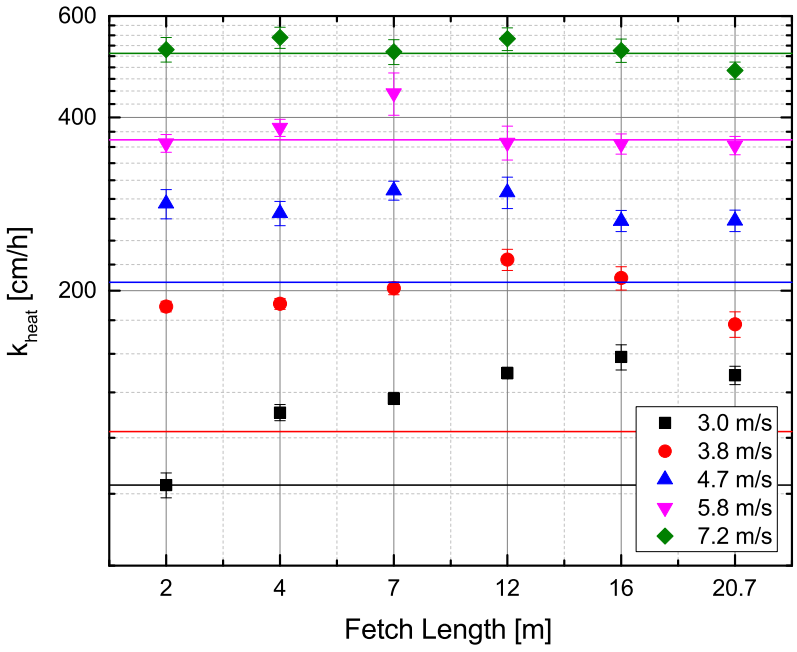

Figure 7.15.: Local heat transfer velocities against different fetch lengths as measured in the Aeolotron for different reference wind speeds. The solid lines represent the heat transfer velocities measured for an infinite fetch (c.f. section 7.2.1).

A similar behaviour of both mss and k_{heat} is observed for $u_{ref} = 3.8$ m/s. First

they increase with fetch length and then they both decrease for fetches larger than 12 m. For mss the same is true for a wind speed of 4.7 m/s, however at this wind speed, k_{heat} starts to remain constant for increasing fetch lengths. At 3.0 m/s no decrease in mss is visible for larger fetch lengths, but the curvature of the increase in mss suggests that the maximal mss value has been reached for a fetch length of 20.7 m.

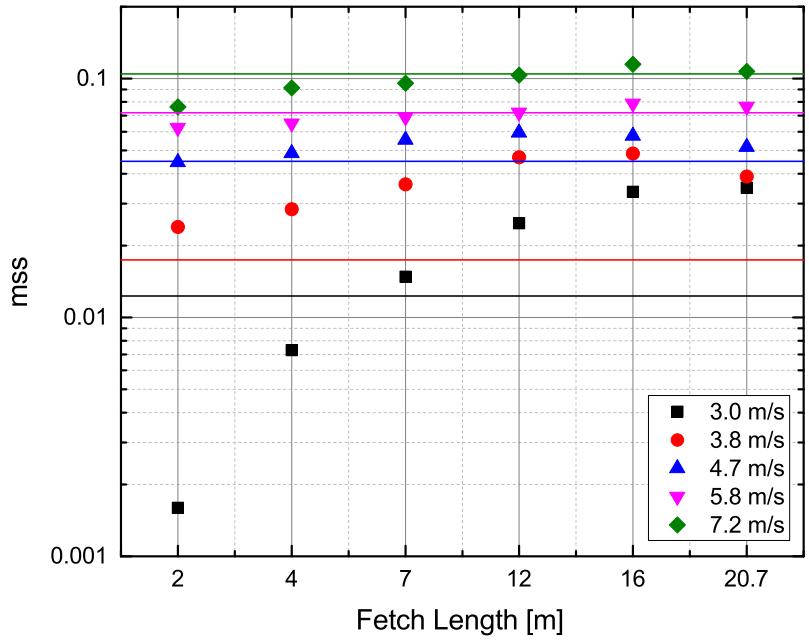

Figure 7.16.: Local mean square slope of the water surface against different fetch lengths as measured in the Aeolotron for different reference wind speeds. The solid lines represent the mean square slope values measured for an infinite fetch (c.f. section 7.2.1).

While k_{heat} and mss show the same qualitative behaviour for lower wind speeds (except for the missing decrease in mss for a wind speed of 3.0 m/s for large fetch lengths), the correlation between the heat transfer velocity and mss vanishes for high wind speeds. While mss still increases slightly with an increasing fetch length, until a fetch of 12 m is reached, and decreases again for larger fetch lengths, the heat transfer velocity remains more or less constant for the entire fetch range at these wind speeds. Similar observations have already been made by Jähne [55].
By taking a look at figure 7.15 again, it can be seen that for a wind speed of 3.0

m/s the heat transfer velocities measured with fetch limitation are up to 20% larger than the heat transfer velocity for an unlimited fetch. For a wind speed of 3.8 m/s this effect is even stronger with a difference of up to 80% in the measured heat transfer velocities. For 4.7 m/s the difference can be up to about 25%. At higher wind speeds the heat transfer velocities for fetch limited conditions are about the same as the heat transfer velocity measured for infinite fetch. In the figure a decrease of the transfer velocity for larger fetch length and smaller wind speeds is visible. This suggests that the transfer velocity converges towards the transfer velocity at infinite fetch. Thus for low fetch length no equilibrium state is reached and the heat transfer velocity is strongly fetch dependent, at least for low wind speeds. Similar observations are made for the mean square slope values measured for the fetch limited conditions as shown in figure 7.16. However for 3.0 m/s mss is lower for fetch length of 2 m and 4 m than mss for infinite fetch, while k_{heat} is never significantly smaller for limited fetch than for infinite fetch. The relative differences for mss between fetch limited and non fetch limited conditions can be up to 100%.
These observations have consequences for all transfer measurements from linear facilities, as the present measurements clearly show that for low wind speeds, the fetch length has am important influence on the transfer velocity.

7.2.3. The Influence of Surfactants on Heat Exchange

Frew et al. [31] used a heat flux measurement to get first evidence for the importance of surfactants on heat transfer in a field experiment. They conducted an experiment off the coast of New England for low wind speeds and measured inside and outside of a naturally occurring slick. Heat transfer was found to be significantly lower inside the slick.
In order to better quantify the effect of surfactants on heat exchange three measurement series were conducted at the Aeolotron in Heidelberg for unlimited fetch. For each series a different amount of the artificial and soluble surfactant Triton X-100 (c.f. section 5.1) was added into pure deionized water. Figure 7.17 gives an overview over the gained results of heat transfer velocities for different wind speeds. It can clearly be seen, that the amount of Triton X-100 causes a reduction of heat transfer velocities in the intermediate wind speed range between 5 and 9 m/s. At lower wind speeds, the concentration of the surfactant seems to have no effect on heat transfer. From the figure it becomes obvious that a parametrization for heat transfer that is based on wind speed along cannot include the influence of surfactants accurately.
Figure 7.18 shows an overview of the evolution of the mean square slope (mss)

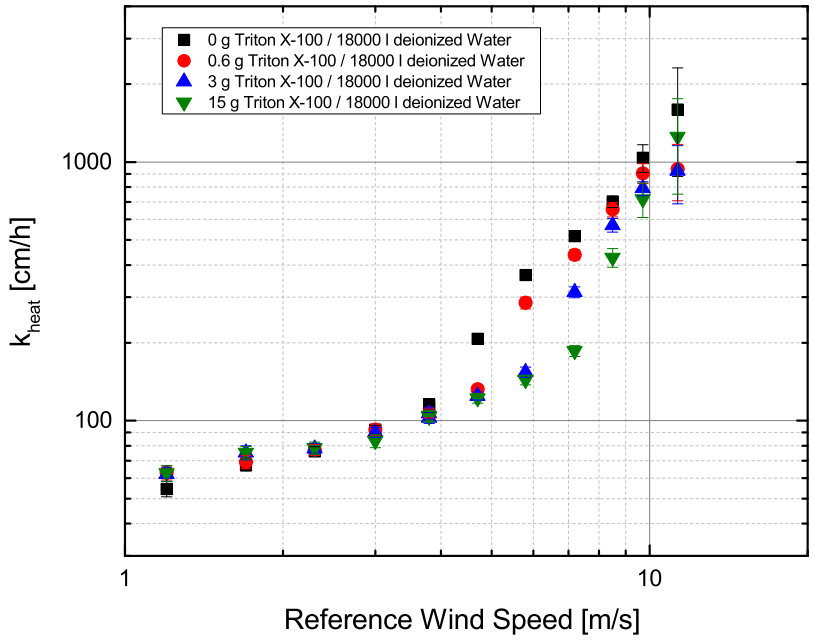

Figure 7.17.: Heat transfer velocities against the reference wind speed in the Aeolotron for four different concentrations of the surfactant Triton X-100. It can clearly be seen, that the increase of the transfer velocity with wind speed becomes steeper at a certain critical wind speed. This critical wind speed is shifted to higher wind speeds with increasing concentration of Triton X-100.

of the water surface and the friction velocity u_* with the reference wind speed u_{ref}. Figure 7.19 and figure 7.21 contain the development of the heat transfer velocity with mss and u_*, respectively. Compared to the heat transfer velocity, the mean square slope of the water surface is much more sensible to changes in the surfactant concentration, even at low wind speeds (figure 7.18 (a)). The friction velocity (figure 7.18 (b)) is also affected by the presence of a surface film at low wind speeds, according to the measurements. However, the exact concentration does not seem to matter a lot. The main difference for the friction velocity is observed between the situation with a clean water surface, where no surfactant is present and the case where a surfactant is present, independent of its concentration. However, the large difference for wind speeds of 1.2 m/s and 2.3 m/s between the friction velocity for a clean water surface and the friction velocity of a surfactant covered water surface arises suspicion. According to

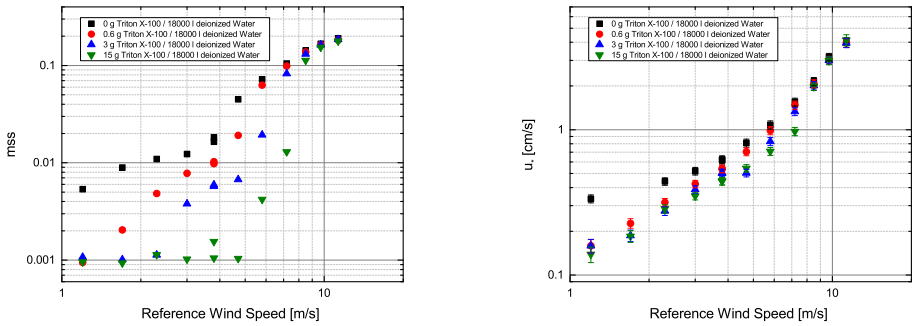

(a) **(b)**

Figure 7.18.: Relation of the mean square slope (mss) of the water surface (a) and of the friction velocity u_* (b) with the reference wind speed for four different concentrations of the artificial surfactant Triton X-100.

earlier friction velocity measurement for clean water conditions, the friction velocity at those two wind speeds is given as 0.20 ± 0.01 cm/s and 0.36 ± 0.02 cm/s instead of 0.34 ± 0.02 cm/s and 0.44 ± 0.03 cm/s [11, 10]. Thus, those two data points should be viewed with caution and the sensitivity of u_* to surfactants becomes less significant without these two data points.
The development of the heat transfer velocity with the friction velocity (figure 7.21) is comparable to the clean water case if the two suspicious data points for the friction velocity at a clean water surface mentioned above are omitted. Recalling once more equation 2.57 shows that the proportionality between the transfer velocity and the friction velocity is given by

$$k \propto \frac{u_*}{\beta} Sc^{-n} \tag{7.4}$$

with the slope

$$\frac{1}{\beta} Sc^{-n}. \tag{7.5}$$

In contrast to the clean water conditions the change in slope according to equation 7.4 happens at larger friction velocities for larger concentration of Triton X-100. While for a clean water surface the slope increases at $u_* = 0.8$ cm/s, this increase shifts to 1 cm/s for 3 g and 15 g Triton X-100 in 18000 l of water. Mind again that all plots are double logarithmic plots and that changes in the slope in equation 7.4 correspond to lines with the same slope but shifted offset in figure 7.21. The transition zone defined by Schnieders [94] already mentioned in section 7.2.1 is also described to shift to higher friction velocities in the presence of sur-

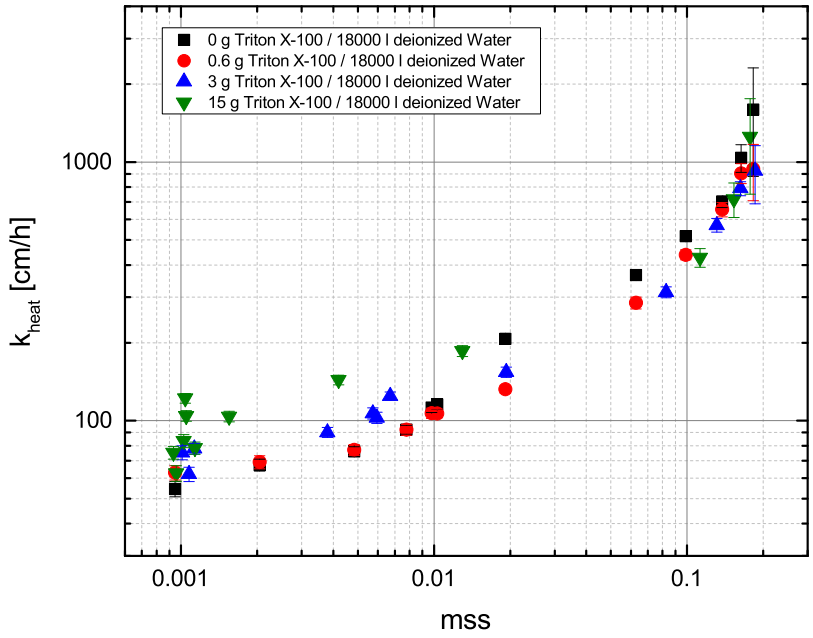

Figure 7.19.: Heat transfer velocities against the mean square slope of the water surface for four different concentrations of Triton X-100 and different wind speeds.

factants. Thus, it can be concluded that both, the change of the slope of the heat transfer velocity given by equation 7.4 and the change in dominant turbulent mechanisms, shift to higher friction velocities with an increasing concentration of Triton X-100.
Following the argumentation in section 7.2.1 it could also be claimed that the heat transfer velocity for the conditions with surfactants are estimated too high, because a thermal equilibrium was not reached. Figure 7.20 shows the temperature evolution with the position along wind direction in the field of view of the IR camera for the lowest wind speed of 1.2 m/s for a clean water surface and for the three cases with different concentrations of Triton X-100 dissolved in the water. Indeed, for the surfactant conditions the equilibrium temperature regions are smaller compared to the clean water case and it is legitimate to argue that the equilibrium temperature has not entirely been reached. However, it is hard to imagine that a further increase of the temperature, as indicated by the curvature of the temperature increase with the position along wind direction in figure 7.20, would lead to an increase of the water surface temperature of 25%.

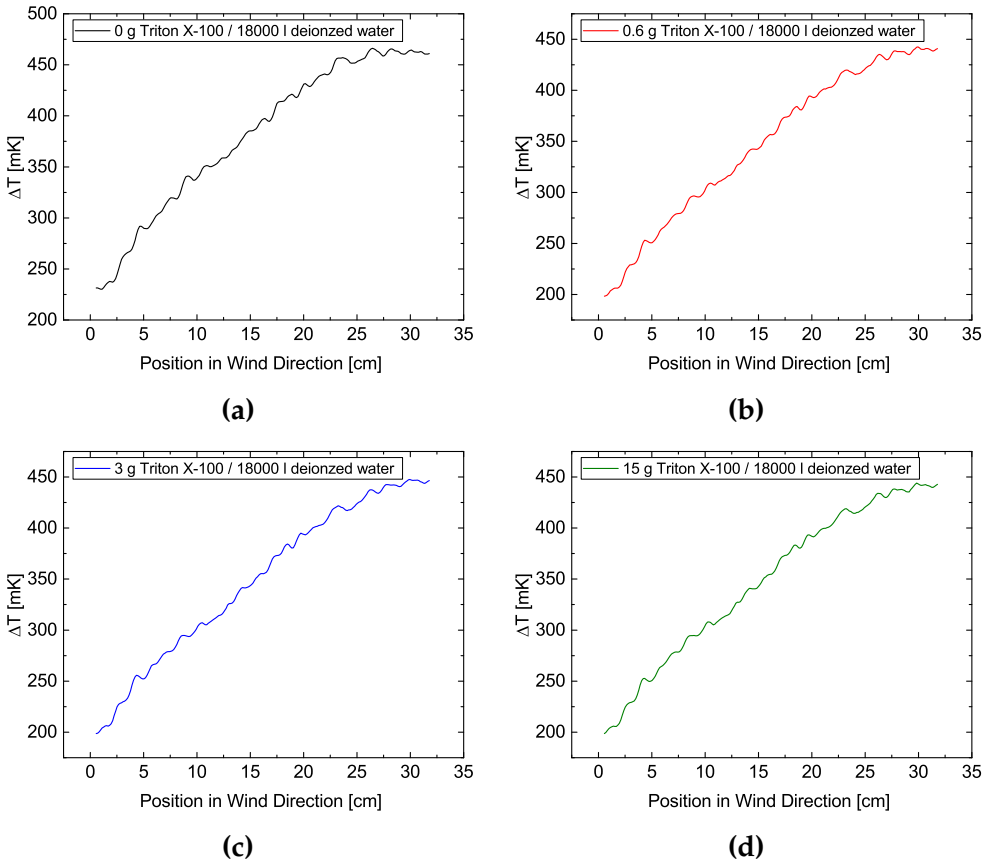

Figure 7.20.: Development of the water surface temperature with position in wind direction as the water drifts through the area heated by the laser (c.f. 3.4). The water flows from left to right in the plots. It can be seen that for all concentrations of Triton X-100 the equilibrium temperature has been reached.

This increase is needed to explain the differences in the heat transfer velocity for a clean water surface and for surfactant covered water surfaces at friction velocities around 0.3 cm/s in figure 7.21. Thus, it is concluded that the measured heat transfer velocities are accurate and that the deviations can be attributed to uncertainties in the estimation of the friction velocity. The finding that heat

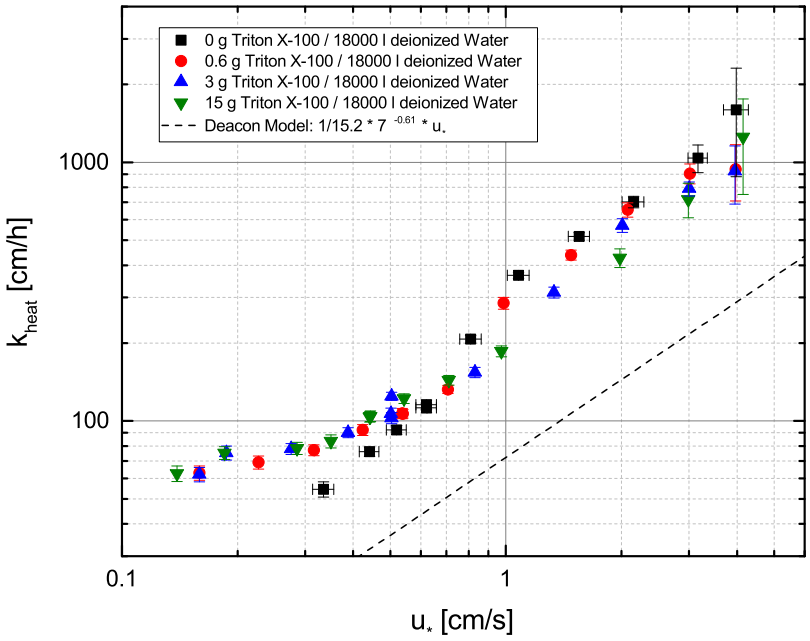

Figure 7.21.: Heat transfer velocities against the friction velocity for four different concentrations of Triton X-100 and different wind speeds. The dashed line shows the prediction of the transfer velocity according to the Deacon model (c.f. section 2.3 and equation 2.46). The measured transfer velocities lie clearly above the transfer velocities predicted by the model.

transfer at low wind speeds and friction velocities does not depend significantly on the concentration of surface active material contradicts observations by Krall made for gas transfer measurements [62]. Already for wind speeds of 1.5 m/s deviations in the transfer velocity of N_2O for clean water conditions and different concentrations of Triton X-100 have been measured. Measurements from Krall [62] also show, that below wind speeds of 2.5 m/s to 4 m/s, depending on the surfactant concentration, the Schmidt number exponent does not change. The deviations in the transfer velocity of N_2O for lower wind speeds should thus be

attributed to changes in the dimensionless momentum resistance β (c.f. section 2.3 and equation 7.4). Therefore, it can be concluded, that for heat transfer β does not change significantly for different surfactant concentrations. Also shown in figure 7.21 is the model curve according to Deacon's model (c.f. section 2.3). It can clearly be seen, that the measured heat transfer velocities lie significantly above the transfer velocities predicted by the model according to equation 2.46. However, for gas transfer measurements Deacon's description holds for low wind speeds and a surfactant covered water surface and can be used as a lower limit for the estimation of transfer velocities [62]. For heat transfer this does not seem to be the case, according to the present measurements.
The development of the heat transfer velocity with the mean square slope of the water surface shows a gradual change in its slope (figure 7.19). Interestingly, the heat transfer velocity at low mss values is higher for higher concentrations of Triton X-100 for a constant mss value. In figure 7.18 (a) it can be seen, that at low wind speeds, mss is always larger for smaller surfactant concentrations. As the heat transfer velocity for mss between 0.001 and 0.01 varies by around 40% between different concentrations of Triton X-100 at a certain fixed mss value, this suggests, that the suppression of small capillary waves by surface films is stronger than the reduction of heat transfer. Whereas at high wind speeds the correlation of the heat transfer velocity and the mean square slope of the water surface seems good, at low wind speeds, a parametrization of k_{heat} with mss would thus not incorporate the influence on surfactants adequately. Similar observations have been made for gas transfer measurements [62].

7.3. Sea Water in a Laboratory Environment

The sea water experiment was carried out in November 2014. Actual sea water from the North Atlantic, that had been brought to Heidelberg in September 2014, was filled into the Aeolotron in order to come as close to natural boundary conditions as possible in a laboratory.
The sea water was not filtered or chemically treated before it was filled into the Aeolotron. This means, that apart from the fact, that instead of deionized water salt water was used, there were also bacteria in the water.
For this experiment the ambient illumination in the Aeolotron was optimized by installing a series of white high power LEDs, in order to be able to simulate day and night for the bacteria.
The exact background of the biological activity aside, the bacteria produced surface active material, that affected the wave field. Effects of phytoplancton

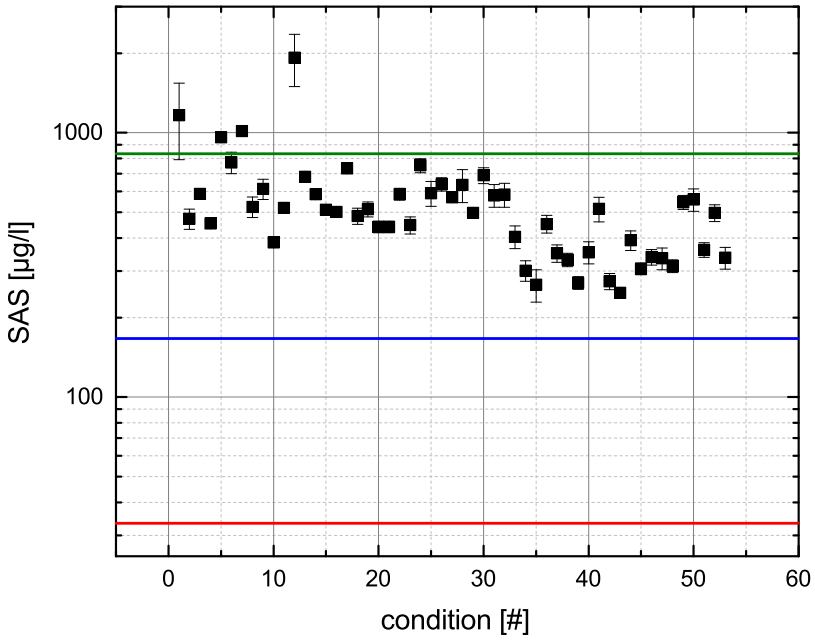

Figure 7.22.: The surface active substances (SAS) in Triton X-100 equivalent concentrations over time during the different measurement conditions (c.f. table A.6 and table A.7) of the measurement campaign in November 2014. The green line shows the concentration of 15 g Triton X-100 for the 18000 l of water in the Aeolotron as used for the systematic studies with artificial surfactants (c.f. section 7.2.3). The blue line corresponds to 3 g per 18000 l concentration and the red line to 0.6 g per 18000 l.

generated surfactants on the an air-sea gas exchange have for example been investigated by Frew 1997 [29], who found a significant reduction of oxygen transfer rates of up to 50%. To quantify the surface active material in the present experiment, the amount of surface active material is given as Triton X-100 equivalent concentrations, that have kindly been provided by Mariana Ribas Ribas and her colleagues from Oliver Wurl's research group from the ICBM at the University of Oldenburg. In this way it is possible to compare the measurement conditions from the sea water measurement campaign to the measurements with artificially added Triton X-100 (see section 7.2.3). The Triton X-100 equivalent concentration of surface active substances (SAS), measured during the sea water campaign, can be seen in figure 7.22.
The optical properties of sea water are slightly different than those of pure water. However, the differences are very small and should not affect the heat transfer measurements. Therefore they are neglected for the analysis of the obtained data. More details about the optical properties of fresh water and sea water can be found in section 3.1.2.
Many measurement conditions were investigated during the measurement campaign, summarized in table A.6 and table A.7. However, mainly there were two sets of wind speeds run in alternating order on the measurement days. Both sets include nearly the full wind speed range possible in the Aeolotron, but the individual wind speeds from the different wind speed sets are slightly shifted against the wind speeds from the other wind speed set in order to maximize the total amount of investigated wind speeds. There is one intermediate wind speed of 3.8 m/s that is included in both wind speed sets. This condition can be used for a cross checks to see if the boundary conditions have changed between the measurement days.
Figure 7.23 shows the results for the heat transfer velocity for different friction velocities u_* obtained during the measurement campaign. From the figure it can be seen, that there are two distinct regions, that differ in the development of the heat transfer velocity with u_*. One region for the lower wind speeds and correspondingly lower friction velocities of up to approximately $u_* = 0.7$ cm/s and one region for the higher friction velocities of $u_* > 1.0$ cm/s. Between those two regimes, there is a transition zone, where the heat transfer velocity increases suddenly in a step-like behaviour. This transition region corresponds to the break up of the surface film in the experiment, as no such sudden increase of the heat transfer velocity is observed for a clean surfactant free water surface (c.f. figure 7.9).
This effect is even stronger pronounced for the mean square slope of the water surface, as can be seen in figure 7.24. A quasi bi-modal behaviour of the mean square slope is visible. The water surface is basically flat for $u* < 0.5$ cm/s,

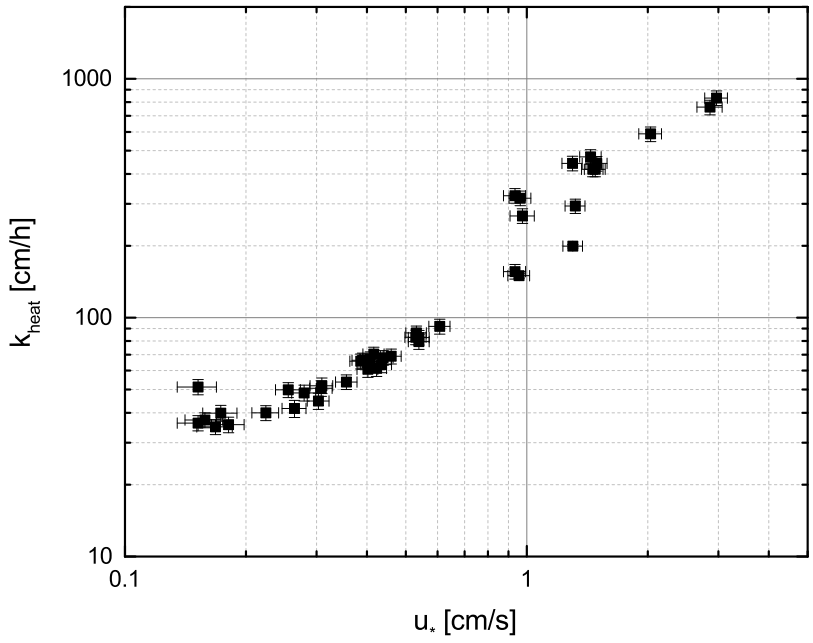

Figure 7.23.: Measured heat transfer velocities against the friction velocity u_* for all measurement conditions of the sea water measurement campaign conducted in the Aeolotron in November 2014.

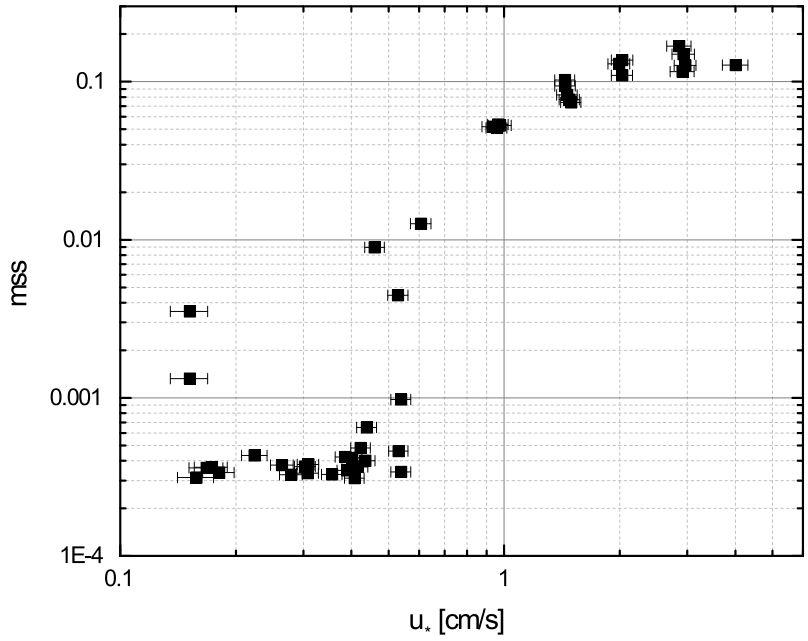

Figure 7.24.: Mean square slope (mss) of the water surface against the friction velocity u_* for all measurement conditions of the sea water measurement campaign conducted in the Aeolotron in November 2014.

as mss values below 0.001 cannot be resolved with the given accuracy of the ISG. For higher friction velocities the break up of the surface film increases mss significantly, until a saturation of mss occurs at around $u_* > 2$ cm/s. However, this corresponds to the highest wind speeds in the Aeolotron and at these conditions a lot of wave breaking occurs, which is accompanied by massive bubble entrainment. The presence of bubbles strongly affects the wave slope measurements, that are based on refraction at the water surface, so that the mss values measured for the highest wind speeds are not very reliable.
As can be seen from figure 7.22, the Triton X-100 equivalent concentration of the surface active material varies between the concentration of 3 g and 15 g Triton X-100 per 18000 litre in the Aeolotron. Figure 7.25 shows the comparison of the heat transfer velocities obtained during the sea water measurement campaign and the measurements from 2015 with artificially added Triton X-100 (c.f. section 7.2.3). Except for low wind speeds, i.e. $u_* < 0.8$ cm/s, the natural surfactants from the sea water seem to influence heat transfer equally as the artificial surfactant Triton X-100. The difference at the small friction velocities might be an effect of

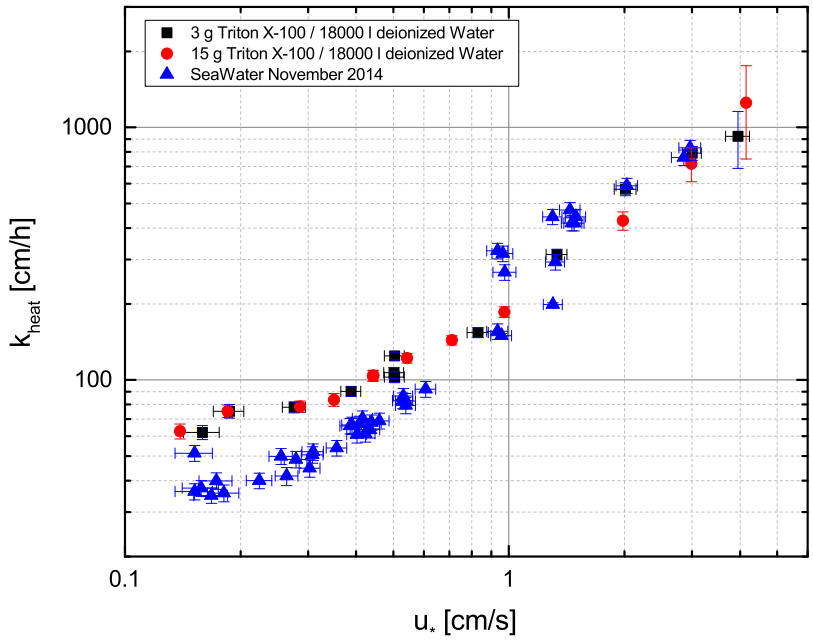

Figure 7.25.: Comparison of the heat transfer velocities obtained from the sea water measurement campaign in November 2014 in the Aeolotron and the measurements with artificially added Triton X-100 from 2015.

the equilibrium temperature extrapolation, that was necessary for the evaluation of the sea water data (see section 6.1.1). As described in section 3.4, it take a certain time until a water surface element that flows through the area on the water surface that is heated by the laser, has heated up to a temperature, where an equilibrium between the incoming energy from the laser and the outgoing energy of heat, that is transported down into the water bulk, is reached. If the area illuminated by the laser is too small, then the temperature difference ΔT that is measured appears too small. From equation 3.20 it can easily be seen, that this leads to an overestimation of the heat transfer velocity:

$$k_{heat} = \frac{j_{heat}}{\rho c_p \Delta T} \tag{7.6}$$

Due to problems with a focusing cylindrical lens, that was positioned in from of the diffractive beam homogenizer, and that rotated due to vibrations during the sea water measurement campaign, the effective area on the water surface, that was heated homogeneously, was smaller, than initially intended. The consequence was, that the equilibrium temperature had not been reached for many conditions of the sea water campaign. To correct for this circumstance, an extrapolation of the temperature increase of the water flowing through the laser illumination area is applied, as described in section 6.1.1. In section 6.1.1 also an example from the sea water campaign is shown in figure 6.3 (c) and (d). However, if this extrapolation predicts too high temperature differences ΔT for the equilibrium, this could explain the deviation of the heat transfer velocities for the sea water case compared to the measurements with artificial surfactants, as observed in figure 7.25.

As mentioned above, the aim of the experiment was to come as close as possible to a field study as it is possible inside a laboratory. Therefore the results obtained during this measurement campaign are compared to field studies done by Nagel [77], which are the most recent heat transfer field studies available to the knowledge of the author. Nagel conducted two measurement campaigns on-board the German research vessel FS Alkor and one measurement campaign on the Finish research vessel RV Aranda. All three measurement campaigns were carried out in the Baltic Sea. Results of the first measurement campaign with the FS Alkor can also be found in Schimpf 2011 [93]. Figure 7.26 shows the comparison between the sea water data obtained in the Aeolotron and the field studies from Nagel and Schimpf. It should be noted, that the wind speed used for the comparison is the wind speed u_{10} measured in 10 meters height above the water surface. The values u_{10} from the Aeolotron of course cannot be measured directly, given the height of 1.5 m of the air space in the Aeolotron, but need to be calculated from the measured friction velocities. Details about this calculation

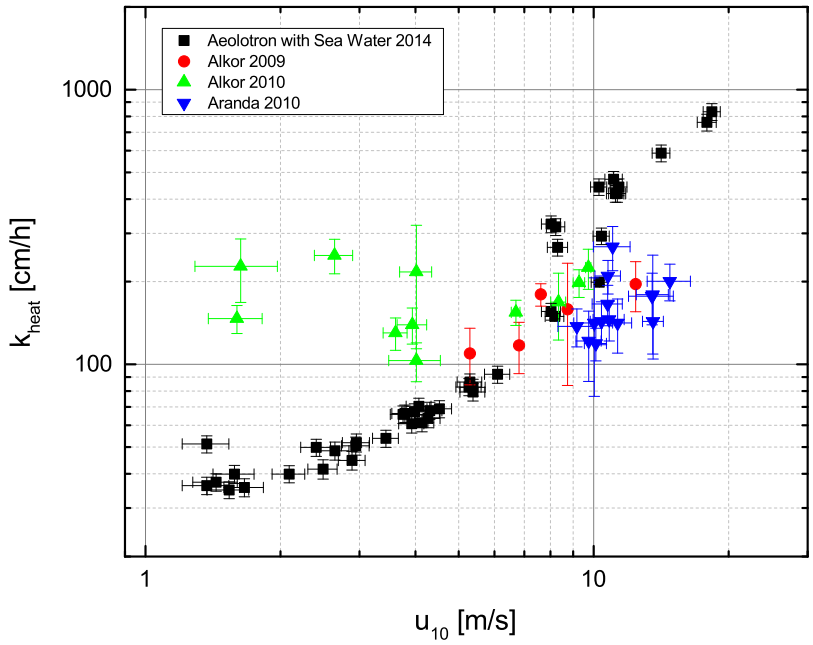

Figure 7.26.: Compilation of the results from the measurement campaign with sea water conducted in the Aeolotron in November 2014 and three different field campaigns from Nagel [77].

are given by Bopp [11]. While most of the data from the measurements done on-board the FS Alkor in 2009 are in agreement with the laboratory data, the field measurements done in 2010 deviate from the laboratory data. However, as already stated by Nagel in her PhD thesis [77], the data from the cruise on FS Alkor in 2010 contained a lot of calm conditions with very low wind speeds. For these conditions the thermal equilibrium was not reached within the heated area, which leads to heat transfer velocities that are too high, as already explained earlier. As no temperature extrapolation correction was applied, the direct consequence can be seen in figure 7.26, where the Alkor 2010 data for low wind speeds shows much higher heat transfer velocities at low wind speeds compared to the measurements at the Aeolotron. This shows the advantage of the temperature extrapolation procedure, although this is still an experimental technique, that needs further theoretical justification (see section 6.1.1).
The measurements conducted on RV Aranda in contrary show smaller heat transfer measurements than the laboratory study from the Aeolotron. Nagel suggests in her thesis, that this might be due to fetch limitations, as most measurements had to be done close to the shore due to stormy weather. However the systematic fetch dependency study conducted within the scope of this thesis shows, that heat transfer at high wind speeds is not affected strongly by fetch variations (compare for figure 7.15).
For the data points from the 11th and 13th of November 2014 simultaneous gas transfer measurements are available for the sea water measurement campaign. From these gas transfer measurements also the Schmidt number exponent could be derived, which is provided by Kerstin Krall. Given the Schmidt number exponent, it is possibly to apply Schmidt number scaling and to convert the measured heat transfer velocities to gas transfer velocities of e.g. CO_2 at 20°C for fresh water with a Schmidt number of 600. For the scaling a Schmidt or Prandtl number of 7 was used for heat. Applying the same scaling to a directly measured gas transfer velocity allows for a direct comparison of heat and gas transfer. Such a direct comparison is presented in section 7.7. Here the scaled heat transfer velocities are compared to empirical gas exchange models commonly used. Figure 7.27 shows that the data obtained in the laboratory lies completely within the range covered by the empirical models. This is remarkable, as the wind speed u_{10} is estimated from the friction velocity and not measured directly, and especially as the equilibrium temperature extrapolation had to be applied to the measured data, as the thermal equilibrium was not reached during many measurement conditions. Only the data point at $u_{10} = 11.08$ m/s and one data point at 8 m/s are larger than predicted by the empirical models. However, it should be mentioned that the models themselves deviate quite strongly from

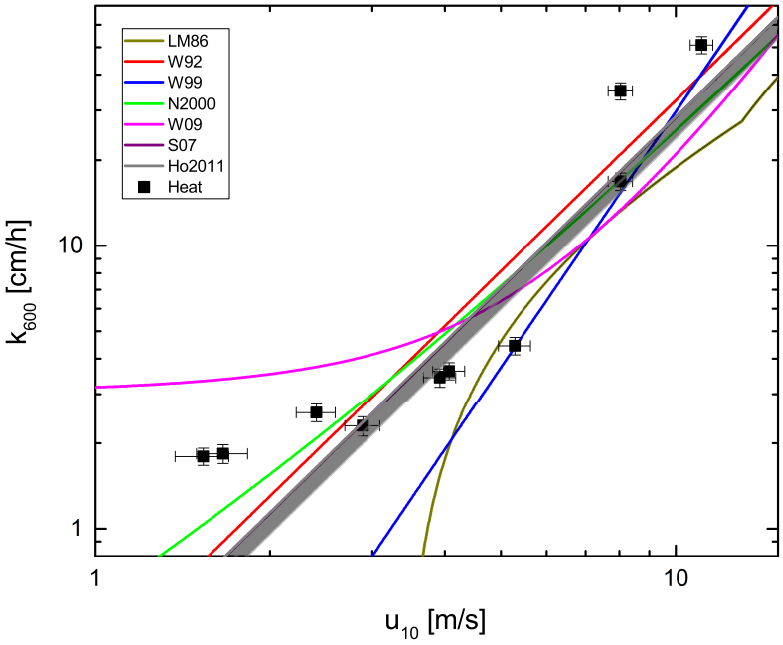

Figure 7.27.: The heat transfer velocities from the 11th and 13th of November 2014 have been scalled to k_{600} and compared to empirical models: LM86 denotes Liss and Merlivat 1986 [70], W92 denotes Wanninkhof 1992 [102], W99 stands for Wanninkhof and McGillis 1999 [103], N2000 et al. is Nightingale 2000 [80], S07 represents Sweeney et al. 2007 [98],W09 is Wanninkhof et al. 2009 [104], Ho2011 represents Ho et al. 2011 [46].

each other and that no single parametrization is fully in accordance with the measured data.

7.4. Aeolotron with Unknown Biological Activity

The measurement campaign in October 2016 at the Aeolotron was initially planned to be run with clean water without any surfactants. However, at the beginning of the measurements some form of bacteria started to thrive in the water channel. As the exact nature of these bacteria or the amount and influence of jellylike particles produced by the bacteria that accumulated at the water

surface during the measurements could not be estimated, this measurement campaign mainly serves as a test setting for the new excitation schemes (see section 7.1.3). In this section the results obtained with the amplitude damping method for the few experimental conditions that were stable are presented. Stable conditions are characterized by constant mean square slope values during the hole time of both heat and gas transfer measurements in this context. Note that for comparing different heat transfer measurement schemes mss does not need to be constant for as long as for a complete gas transfer measurement that can last for 10 hours or more. This is the reason for different conditions shown here and in table 7.2. Also for the highest wind speeds of 8.5 m/s and 9.7 m/s and for a wind speed of 3 m/s only amplitude damping measurements are available due to technical problems with the Arduino used to create the multifrequency excitation pattern. At the time of printing of this thesis, no data for the friction velocity or detailed evaluation of the mean square slope of the water surface was available, so only the reference wind speed can be used as a parameter for heat exchange. The results of the measurements are shown in figure 7.28. The figure also shows the data for the clean water conditions in the Aeolotron measured in June 2015. An increase of the heat transfer velocities with the wind speed can be seen and except for a wind speed of 4.7 m/s the data is in agreement with the heat transfer velocities for clean water condition. However, due to the lack of other parameters, no further interpretation is possible. It should also be mentioned that only for the intermediate and high wind speed regimes data is available and thus no comparison with the clean water case for low wind speeds is possible. In section 7.7 the heat transfer velocity values are compared with simultaneously measured gas transfer velocities.

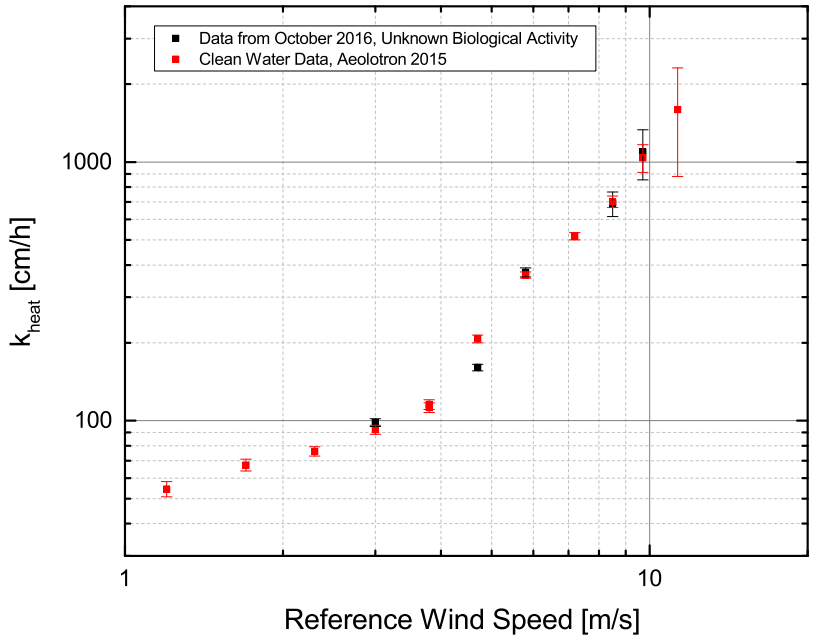

Figure 7.28.: Results from the measurement campaign with unknown biological activity in the Aeolotron in 2016. All conditions except for the lowest wind speed ($u_{ref} = 3\frac{m}{s}$) were stable conditions, i.e. the mean square slope of the water surface was nearly constant for the whole measurement duration.

7.5. Results from the Linear Wind Wave Facility in Marseille

The main purpose of the measurement campaign in Marseille was to investigate the influence of breaking waves on heat and gas transfer. As no salt water can be used in the Marseille facility, butanol was used to create bubble size and number distributions comparable to salt water (more details about this effect can be found in Mischler [75]). Unfortunately, due to technical problems with one CO_2 laser and finally failure of this laser, not for all conditions investigated heat transfer data is available. The conditions, where heat transfer velocity data is available, are summarized in figure 7.29. In general, there were conditions, where the waves in the Pytheas facility were purely generated by wind. Then

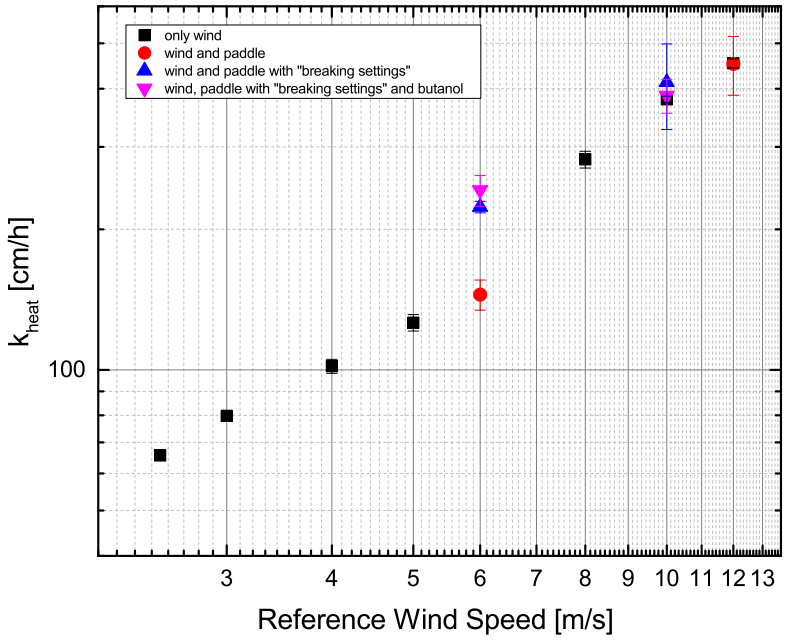

Figure 7.29.: Overview of the results gained in the Marseille wind wave facility for all conditions that could be evaluated. "paddle" means that a mechanical wave generator has been used and was adjusted for a regular wave field. "breaking settings" indicates that the mechanical wave generator was used to create a wave field where a lot of wave breaking happened. The frequencies used for the mechanical wave generator can be found in table 5.11.

there were conditions where the mechanical wave generator, also referred to as paddle (c.f. section 4.2.1), was used to create a very regular and stable wave field. The mechanical wave generator was also used to generate a wave field that was optimized to have as much wave breaking events as possible in the water channel. In addition to the latter conditions with the enhanced wave breaking, there were conditions with added butanol to simulate the breaking case for salt water.
By looking at figure 7.29 it becomes apparent, that unfortunately at a wind speed of 6 m/s there is no data available for the purely wind driven case. From figure 7.29 it can also be seen, that there is a constant increase of the heat transfer velocity with wind speed until at a wind speed of 6 m/s this increase changes suddenly. This effect is observed for breaking waves for both cases, fresh water

with and without butanol. For the case with the mechanically generated waves that are optimized for wave breaking, the heat transfer velocity at a wind speed of 6 m/s is 54% larger than for mechanical waves optimized for a regular wave field. Due to the lack of data for mechanically generated regular waves between 6 m/s and 10 m/s wind speed, it is not clear, at what wind speed the increase of the heat transfer velocity happens for this kind of wave field. However, from the data available it seems, that breaking waves enhance heat transfer for a wind speed of 6 m/s. At higher wind speeds in contrast, enhanced wave breaking does not seem to play a role for heat transfer.

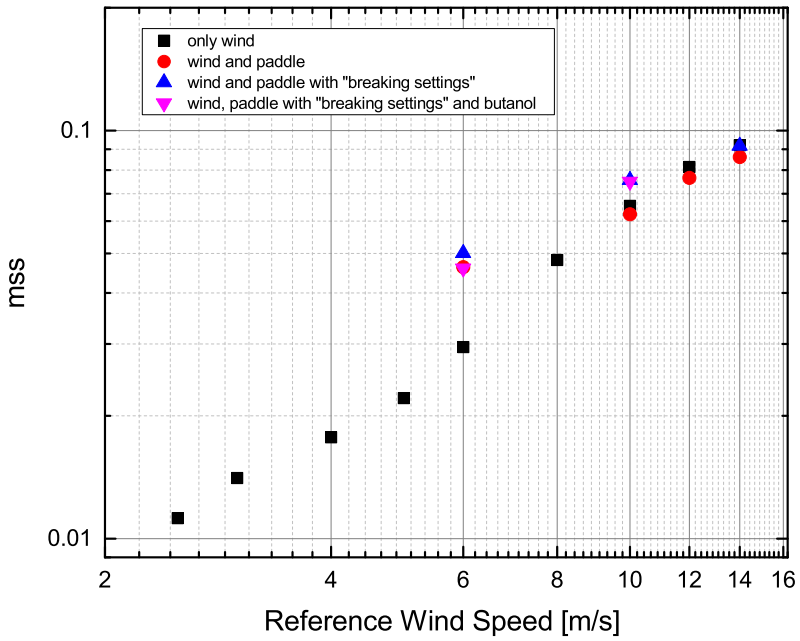

Figure 7.30.: Dependence of the mean square wave slope on the reference wind speed at Pytheas. "paddle" means that a mechanical wave generator has been used and was adjusted for a regular wave field. "breaking settings" indicates that the mechanical wave generator was used to create a wave field where a lot of wave breaking happened. The frequencies used for the mechanical wave generator can be found in table 5.11.

Figure 7.30 shows the mean square slope (mss) of the water surface against the wind speed in the facility. In the figure it can be seen that similar to the development of the heat transfer velocity there is a sudden change of mss at a wind speed at of 6 m/s. However, the increase of mss also happens for the

regular waves and not only for those optimized for wave breaking.

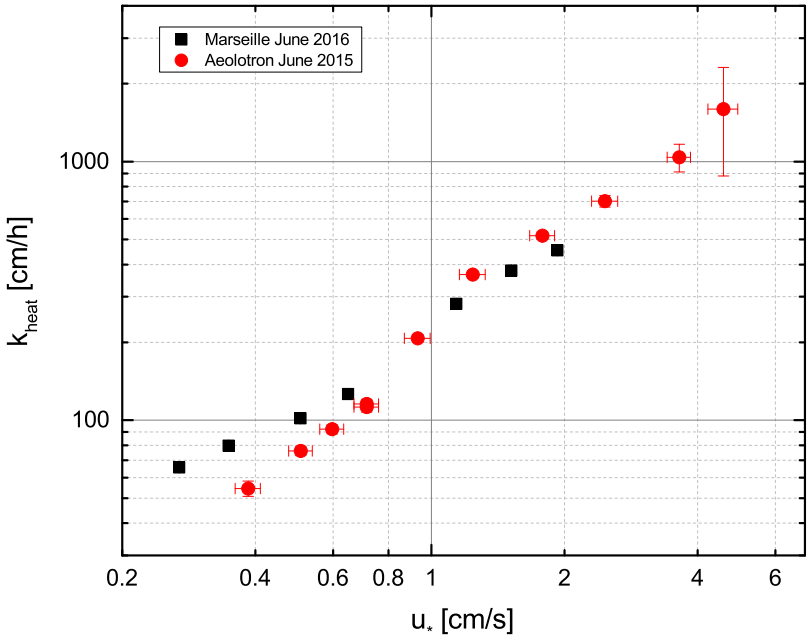

Figure 7.31.: Comparison of the dependence of the heat transfer velocity on the friction velocity for the Marseille facility and for the Heidelberg Aeolotron for purely wind driven waves.

The friction velocity u_* is used to compare the measurements of the heat transfer velocities at Pytheas and at the Aeolotron. Pytheas and the Aeolotron are two entirely different facilities, the first one being a linear facility with a limited fetch and the latter one being circular with infinite fetch (c.f. section 4.1 and section 4.2). As described by Bopp [10], the wind field is not perfectly homogeneous in the Aeolotron, because it is generated locally at two spots by wind turbines (c.f. section 4.1). The resulting spatial inhomogeneities in the wind field are accompanied by a difference in the global friction velocity and the local friction velocity at the optical section, where the heat transfer measurements take place. As done by Nagel [78] and based on the results of Bopp [10] the global friction velocities are multiplied by a factor of 1.15 to get an estimate for the local friction velocities at the location of the heat transfer measurements in the Aeolotron for the comparison with the local friction velocities in the Marseille facility. Figure 7.31 shows the comparison of heat transfer velocities measured in both facilities for purely wind generated waves for fresh water without butanol or

surfactants. In general the heat transfer velocities are in a good agreement and show similar developments with the friction velocity. However, at low friction velocities the heat transfer velocities measured in the Aeolotron are smaller than those measured at Pytheas. The reason for this might be the limited fetch in the Marseille facility. The heat transfer velocity at a friction velocity of 0.5 cm/s in figure 7.31 corresponds to a wind speed of 3 m/s in the Aeolotron. This is the lowest wind speed used for the fetch measurements in the Aeolotron (c.f. section 7.2.2). k_{heat} for infinite fetch for this condition is 92 ± 4 cm/h. For a fetch length of 20.7 m, the longest limited fetch length that can be investigated in the Aeolotron, the heat transfer velocity is 143 ± 5 cm/h. For $u_* = 0.5$ cm/s the heat transfer measured in Marseille is 102 ± 3 cm/h (all numerical results can be found in section A.1). As suggested in section 7.2.2 for a wind speed of 3 m/s k_{heat} seems to decrease further with increasing fetch for fetches longer than 20.7 m/s. The fetch length in Marseille is 27 m and thus longer than the 20.7 m in the Aeolotron. This could explain the heat transfer velocity measured in Marseille, that is in between the 92 ± 4 cm/h for the infinite fetch and the 143 ± 5 cm/h for 20.7 m fetch, measured in the Aeolotron. However, as already mentioned in section 7.2.3, the two data points with the lowest friction velocities from the measurements at the Aeolotron should be viewed with caution. Earlier measurements with similar conditions list the friction velocities at those points to be 0.2 ± 0.01 cm/s and 0.36 ± 0.02 cm/s instead of 0.34 ± 0.02 cm/s and 0.44 ± 0.03 cm/s [11, 10]. This is an alternative explanation for the difference between the measurements from the Marseille facility and the Aeolotron shown in figure 7.31. In this case it could be concluded, that at 27 m fetch the heat transfer velocity has nearly converged towards the heat transfer velocity for infinite fetch.

7.6. Phase Analysis - An Attempt to Differentiate Between Gas Exchange Models

As described in section 3.3.2 the amplitude damping method can be used to investigate the phase shift between the excitation signal and the temperature response of the water surface. Figures 7.32 and 7.33 show the measured phase shifts for the lower and higher wind speeds for the measurement campaign with clean water without surfactants (c.f. section 7.2.1).
The figures also include the theoretical predictions for the film and surface renewal model and the phase shift of $\pi/4$ for large dimensionless frequencies

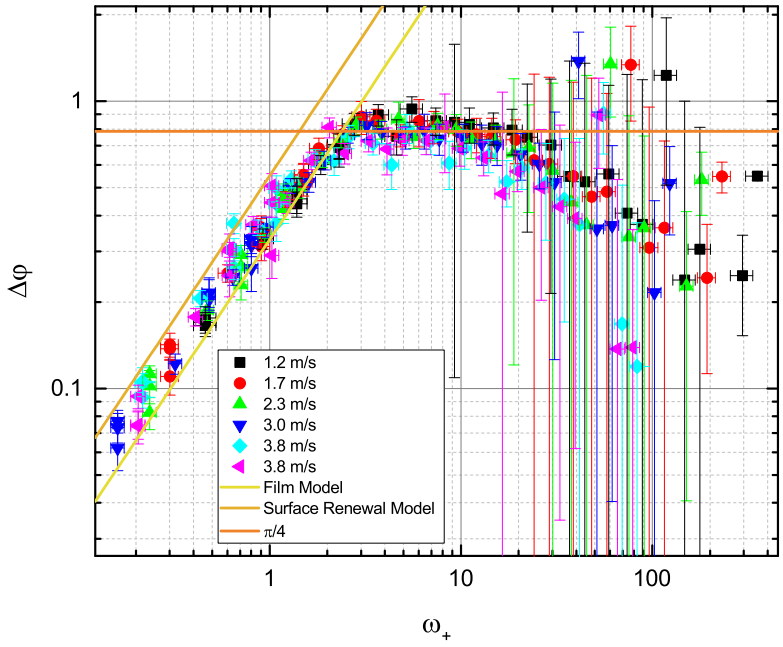

Figure 7.32.: Results from the measured phase shifts for the lower wind speeds investigated. The straight lines indicate the expected phase shifts for low ω_+ given by the surface renewal and the film model, as well as the constant phase shift of $\frac{\pi}{4}$ for large frequencies ω_+ that is expected for both models.

ω_+, that is expected for all models. For low frequencies ω_+ the slope of the phase shifts from the model predictions differs for the different models. Comparing the predicted slopes with the measured phase shifts for the low to intermediate wind speeds (figure 7.32) shows that the slope of the measurement points lies within the range predicted by the film and the surface renewal model. However it can also be seen, that the measurement accuracy does not allow for a distinct differentiation between the two models. Another feature in the figure is the deviation from the phase shifts predicted by the models for high ω_+. The phase shifts seem to decrease again. However, for high ω_+ the uncertainty in the estimated phase shifts is large. At high wind speeds (figure 7.33) the measurements exceed the predicted phase shifts by as much as a factor of 10 for small ω_+. A potential explanation for this effect lies in the statistical nature of

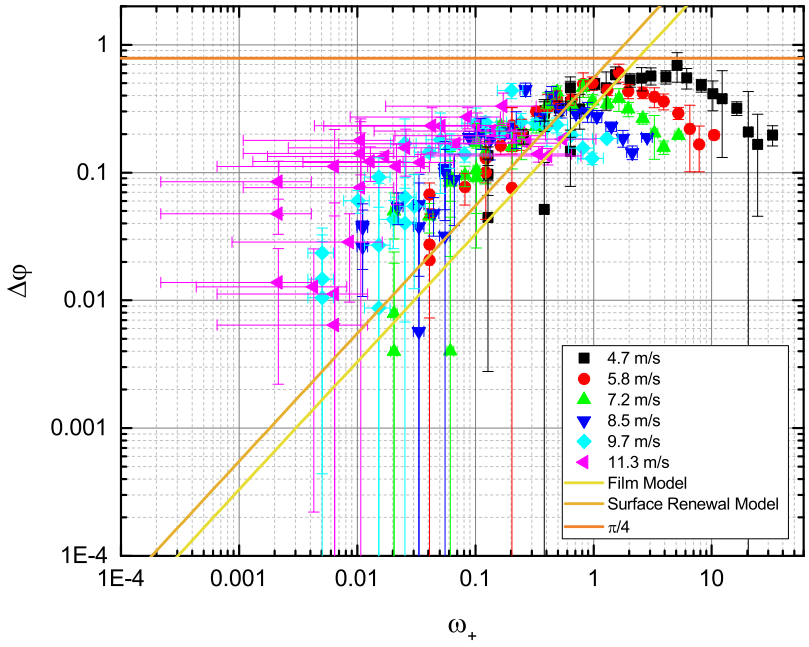

Figure 7.33.: Results from the measured phase shifts for the higher wind speeds investigated. The straight lines indicate the expected phase shifts for low ω_+ given by the surface renewal and the film model, as well as the constant phase shift of $\frac{\pi}{4}$ for large frequencies ω_+ that is expected for both models.

the exchange process and has been proposed by Popp [85] and Jähne [57]. During a measurement of the transfer velocity averaging occurs:

$$\bar{k} = \overline{\left(\frac{j}{\Delta c}\right)} \neq \frac{\bar{j}}{\overline{\Delta c}} \tag{7.7}$$

Assuming that different transfer velocities k_i appear with likelihoods p_i at different locations i at the water surface, leads to a total transfer velocity of

$$k = \sum_i p_i k_i \tag{7.8}$$

with

$$\sum_i p_i = 1. \tag{7.9}$$

The phase shift at the water surface predicted by the film model and the surface renewal model has been presented in section 2.5. For low frequencies, the formulas listed there can be simplified to

$$\phi(0) = \kappa\omega t_* = \kappa\omega\frac{D}{k^2} \tag{7.10}$$

where κ is a constant, that depends on the actual model description [85]. Inserting equation 7.8 yields

$$\phi(0) = \kappa\omega D\sum_i \frac{p_i}{k_i^2}. \tag{7.11}$$

In equation 7.11 the inverse of the quadratic transfer velocity is averaged. Following the bi-modal approach from Jähne [57] two types of areas are defined: the first type corresponds to a fraction α of the total surface area, that has an transfer velocity, that is changed by a factor f. The other type of area then makes up for $(1-\alpha)$ of the total water surface and has a transfer velocity of $g \cdot k$, where k is the transfer velocity. Due to the normalization constraint given by equation 7.9

$$\alpha f + (1-\alpha)g = 1. \tag{7.12}$$

It follows

$$g = \frac{1-\alpha f}{1-\alpha}. \tag{7.13}$$

For the averaging part in equation 7.11 this yields

$$\sum_i \frac{p_i}{k_i^2} = \frac{\alpha}{f^2k^2} + \frac{1-\alpha}{g^2k^2} = \left(\frac{\alpha}{f^2} + \frac{1-\alpha}{g^2}\right)\frac{1}{k^2} = \epsilon\frac{1}{k^2} \tag{7.14}$$

with ϵ the factor of increase in the phase shift due to averaging, which is a consequence of the intermittency of the exchange process. Following the estimation from Popp [85] a factor γ is introduced as

$$f = \frac{\gamma}{\alpha} \tag{7.15}$$

The increase factor ϵ thus becomes

$$\epsilon = \frac{\alpha^3}{\gamma^2} + \frac{(1-\alpha)^3}{(1-\gamma)^2} \tag{7.16}$$

If the fraction α of the water surface is small, equation 7.16 simplifies to

$$\epsilon = \frac{1}{(1-\gamma)^2} \tag{7.17}$$

If now $\gamma = 3/4$ is assumed, then the increase of the phase shift would already be a factor of 16, which is even larger than the observed difference between the model predictions and the measurements in figure 7.33.

7.7. Comparing Heat and Gas Exchange

The comparison of heat and gas exchange is of great interest, as heat transfer can be measured in the field with a temporal and spatial resolution that exceeds any other measurement technique available (c.f. section 2.5.3 and section 3.3). However, scaling heat transfer velocities to gas transfer velocities is controversial. After Haußecker [43] had introduced his implementation of the controlled flux technique (c.f. section 3.3), others adapted this technique and made their own measurements (see for example [115, 3, 6]). All these measurements observed a difference between measured gas transfer rates that are scaled to a transfer velocity of a gas with a Schmidt number of 600 (which corresponds to the Schmidt number of CO_2 at 20°C for fresh water) and measured heat transfer rates that are scaled to k_{600}. The observed trend is that the k_{600} values obtained from the heat transfer measurements are a factor of two larger than those k_{600} values obtained from the gas transfer measurements [3]. Given these observations from the measurements and the fact that the diffusion constants of heat and carbon dioxide in water differ by two orders of magnitude, it is unclear, if both tracers are equally effected by changes in turbulence and if their transfer velocities can be linked by a simple concept like Schmidt number scaling (see section 2.5.3).
An alternative way to describe heat transfer has been proposed by Asher in 2005 [2], where he proposed the use of a surface penetration model, that incorporates the different penetration depths that are due to the different diffusion constants of heat and CO_2. However, this conceptual model does not allow for a better scaling method of heat transfer velocities to gas transfer velocities.
As mentioned in section 3.3, Haußecker's implementation of the controlled flux technique [43] relies on model assumptions. The equation for the transport problem that he used for his work is based on the surface renewal model (see section 2.3). A comparative study of heat and gas exchange that does not rely on model assumption, but uses the original concept of the controlled flux method

as proposed by Jähne [55] has been conducted by Nagel [78, 77]. She concludes, that heat and gas transfer velocities that are scaled to k_{600} are in good agreement, if the Schmidt number exponent is well known.

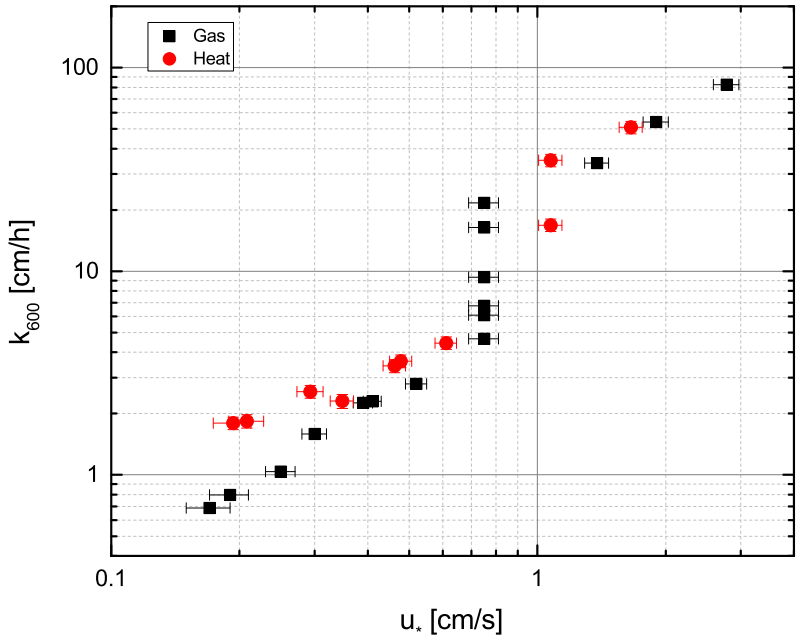

Figure 7.34.: Comparison of heat and gas transfer for the sea water experiment conducted in November 2014. The transfer velocities of heat and of N_2O have both been scaled to the transfer velocity of a gas with Schmidt number 600 for comparison. Gas transfer data and Schmidt number exponents have been provided by Kerstin Krall.

Nagel's study was a laboratory experiment with deionized water and without any surfactants on the water surface. For this thesis, a comparative study of heat and gas transfer was performed within the framework of the SOPRAN sea water experiment, that took place in November 2014 in the Aeolotron in Heidelberg (c.f. sections 5.2 and 7.3). This means that this experiment is also a laboratory experiment, but it comes as close to a field study as possible in a laboratory environment, as actual sea water from the North Sea was used that was not filtered or chemically treated and still contained biological activity producing natural surface active material. On the other hand it benefits from the controlled boundary conditions of a laboratory, where the wind speed etc. can be kept constant for the whole measurement duration that is needed for gas transfer

measurements. Due to technical difficulties with the gas transfer measurements during the sea water experiment, there is only comparative data available for the 11th and 13th of November 2014, provided by Kerstin Krall. Only on these days the Schmidt number exponent could be estimated from the measured gas transfer velocities of N_2O and pentafluoroethane. Details about the derivation of the Schmidt number exponent can be found e.g. in Krall [62]. Without knowledge about the Schmidt number exponent a scaling of transfer velocities is not possible. Figure 7.34 shows the results from the comparative measurements of heat and gas transfer velocities. Note that the data points for heat and gas transfer have different friction velocities at the same wind speeds. This is due to the fact, that the gas transfer measurements integrate globally over the whole water surface in the Aeolotron, while the heat transfer measurements measure locally at one segment of the Aeolotron (see section 4.1). As already described in section 7.5, the globally estimated friction velocities are multiplied by a factor of 1.15 to correct for the spatial inhomogeneities of the wind field in the Aeolotron and to account for a larger wind speed at the measurement position for the heat transfer measurements [10, 78]. For all other results shown in this thesis except for the comparison between the clean water measurements from the Aeolotron and Pytheas (c.f. section 7.5), the globally estimated friction velocities were used, because Bopp [10] only measured at two wind speeds and data that confirms his findings of the strength of the wind speed increase at the section of the Aeolotron, where the heat transfer measurements are done, for other wind speeds is not available. However, for a direct comparison between heat and gas transfer the influence of the locality of the heat transfer measurement should be taken into account and a comparison to the measurements done by Nagel should be given. Thus this correction is applied here.
From figure 7.34 it can be seen, that there are two regimes: for friction velocities u_* smaller than 0.7 cm/s the transfer velocities are significantly smaller than for $u_* > 0.9$ cm/s. Between 0.7 cm/s and 1.0 cm/s the transfer velocity increases step like by an order of magnitude. This step corresponds to the break up of the surface film. This break up is accompanied by a measured change of the Schmidt number exponent from 2/3 to 1/2.
For the high wind speeds the k_{600} values from the heat and gas transfer measurements are in good agreement. However, for the lowest wind speeds used during the experiments, i.e. friction velocities smaller than 0.3 cm/s, heat transfer estimates higher transfer velocities. Unfortunately it cannot be excluded here that this is an artefact from the heat transfer measurements. As explained in section 7.3 the thermal equilibrium (c.f. section 3.4) was not reached and a temperature extrapolation (see section 6.1.1) was used to estimate heat transfer velocities. From equation 3.20 it becomes obvious, that k_{heat} will be estimated too high, if

the extrapolated ΔT is too small. This means, that the deviation between heat and gas transfer for small friction velocities could also be attributed to problems with the equilibrium temperature extrapolation. Interestingly, bubbles do not seem to have a strong effect on the gas transfer velocity, as heat transfer is not sensitive to bubbles and does not deviate significantly from gas transfer at the higher wind speeds in figure 7.34. The used trace gases N_2O and pentafluoroethane have dimensionless solubilities of only 0.59 [113] and 0.184 [112], respectively, and are therefore expected to be influenced by bubbles, especially in salt water, where the number of bubbles is significantly increased compared to fresh water [75]. It should be mentioned, that the gas transfer velocities are preliminary results and have not been completely evaluated and validated yet. Additionally, it should be noted that due to some calibration issues with the measurement devices needed for the gas transfer measurements, these measurements might suffer from yet unquantified uncertainties.

In October 2016 comparative heat and gas transfer measurements were conducted in the Aeolotron with deionized water (c.f. section 7.4). In principle the measurement conditions correspond to those of Nagel [78]. The only intended difference was to expand the wind speed range up to higher wind speeds. However, during the beginning of the experiment some sort of bacteria started to thrive in the water channel of the Aeolotron. This bacteria somehow influenced the water surface and affected the wave field. In this way a unique - unfortunately also unknown - experimental setting was given for the comparison between heat and gas transfer. Figure 7.35 shows the results from this comparison. It should be mentioned, that the gas transfer velocities and Schmidt number exponents obtained from N_2O and pentafluoroethane, that are again provided by Kerstin Krall, are still preliminary. As not all experiments have been evaluated yet, there are no friction velocity values available at the time this thesis is printed and only reference wind speeds can be used. This means, that the spatial inhomogeneities of the wind field in the Aeolotron are not taken into account as for the sea water case. However, the difference between heat and gas transfer, shown in figure 7.35 is roughly a factor of two, while the inhomogeneities in the wind field of the Aeolotron are only around 15% as described above.

The surface conditions were not constant during all measurement conditions. For the higher wind speeds, the water surface did not change a lot, because the influence of surface films is very small for these conditions, as can be seen in figures 7.17 and 7.21 from the systematic measurements with known amounts of surface film. Except for the smallest wind speed of 3 m/s in figure 7.35 the chosen conditions were relatively stable, as already explained in section 7.4. The 3 m/s wind speed condition was measured during a whole weekend for the gas transfer, while the heat transfer measurement was conducted within one

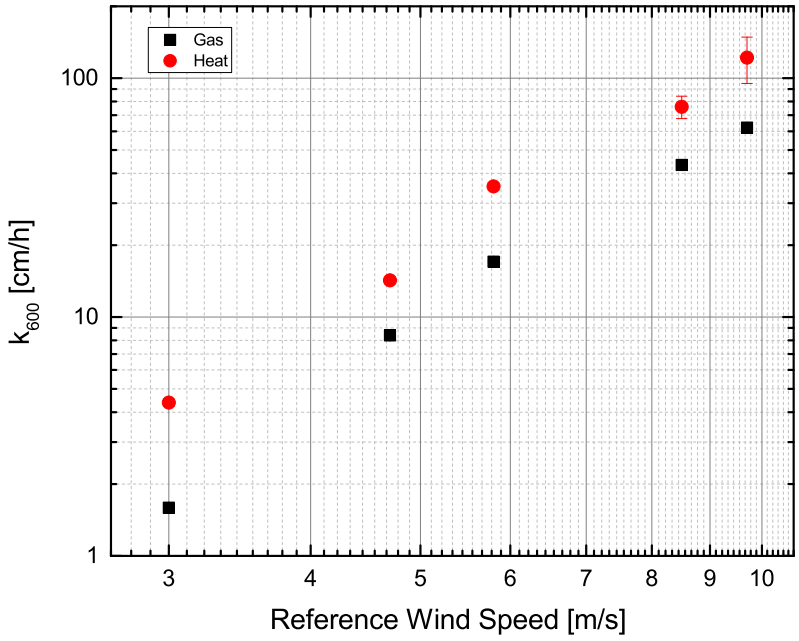

Figure 7.35.: Comparison of heat and gas transfer for the Aeolotron experiment with unknown biological activity conducted in October 2016. The transfer velocities of heat and of N_2O have both been scaled to the transfer velocity of a gas with Schmidt number 600 for comparison. Gas transfer data and Schmidt number exponents have been provided by Kerstin Krall.

hour on the Friday before the weekend. As mss decreased during the weekend, this means, that the gas transfer measurement has integrated over the different water surface conditions, while the heat transfer measurement measured under a nearly constant condition with a rougher water surface.
The nearly constant difference between heat and gas by a factor of two is remarkable. From these measurements this difference seems independent of the wind speed and therefore of the degree of turbulence present in air and water, respectively. The difference is also observed at high wind speeds, where the influence of surfactants in negligible and heat and gas transfer measurements should not be affected differently by surface films that develop over time due to the different measurement times. As mentioned before, a difference between heat and gas transfer velocities of a factor of two has already been observed in earlier measurements [115, 6], and also in field measurements [3]. However, the

results from the measurements at hand should be seen critically, as the whole experimental environment is not characterized. It is unknown what kind of bacteria was present and in what way it influenced the water surface. On top of this it cannot be completely excluded that the bacteria's metabolism influences the gas exchange measurements. Indications for biological enhancement of gas transfer have for example been observed for methane by Upstill-Goddard et al. [99].
The measurements from this thesis combined with those from Nagel [78, 77] reveal that there are certain differences between heat and gas exchange. For a rough water surface without any surfactants, heat and gas exchange are in good agreement, when scaled to a gas with the same Schmidt number. If surfactants are present, gas exchange is significantly affected for low and intermediate wind speeds, up to friction velocities of 1.5 cm/s [62]. Heat transfer in comparison only shows an influence of surface films for an intermediate wind speed regime, that corresponds to friction velocities of roughly 0.8 cm/s to 2 cm/s. For low wind speeds, the presence of surfactants does not influence heat exchange (c.f. section 7.2.3). The Deacon model (c.f. section 2.3) is only in accordance with the gas exchange velocities measured for low wind speeds and with surfactant coverage. Thus the Deacon model can only be used to estimate a lower boundary for gas exchange, but not for heat exchange. Interestingly, the measurements with sea water and natural surface films show indications of heat transfer reduction at low wind speeds, which is not the case for the measurements with Triton X-100. However, it has been mentioned above that the measured heat transfer velocities at low wind speed for the sea water conditions rely on an extrapolation for the estimation of the equilibrium temperature increase (c.f. 6.1.1). Those heat transfer velocities should therefore be viewed with caution. However, even if the extrapolation described in section 6.1.1 would not reproduce the actual temperature increase completely, the fact that the thermal equilibrium has not been reached and that the heat transfer velocities therefore are overestimated without a correction remains. The example shown in figure 6.3 indicates an extrapolated temperature increase of roughly a factor of 1.5. Even if the temperature would only increase by a factor of 1.3, a tendency for lower heat transfer velocities for the natural surfactants compared to the Triton X-100 conditions would remain. At the same time the gas transfer measurements for the natural surfactant conditions are in accordance with the measured gas transfer velocities from Krall for Triton X-100 conditions [62], indicating that here no further reduction of the gas transfer velocity takes place.
In conclusion, heat and gas transfer behave similar in an intermediate to high wind speed regime, but significant differences are found for low wind speeds. At those low wind speeds the variation of gas transfer velocities can be up to 300%

[62] depending on the surfactant concentration, while heat transfer velocities only agree with the highest measured gas transfer velocities, i.e. those for a clean water surface. The measurements conducted in the Aeolotron in October 2016 in addition find differences for heat and gas exchange also for intermediate and high wind speeds. Heat transfer velocities are found to be twice as large as heat transfer velocities when scaled to a gas with the same Schmidt number. All observations described above lead to the conclusion that heat transfer measurements cannot directly be scaled to gas transfer velocities without uncertainties. However, heat transfer velocities can be used to estimate an upper boundary for gas transfer velocities, at least for the complete wind speed range investigated within the scope of this thesis.

8 Conclusion and Outlook

8.1. Conclusion

Two main objectives have been set for this thesis: the first one was the advancement of an existing measurement technique designed for the estimation of air-water heat transfer velocities. The second objective was to conduct systematic studies of heat exchange across the aqueous boundary layer.

8.1.1. Advancement of the Measurement Technique

The measurement concept of the controlled flux method (c.f. section 3.3) is based on the precise control of a locally applied heat flux density at the water surface. The energy for heating the water surface is provided by one or two 100 W CO_2 lasers. The beam shaping procedure needed to achieve a rectangular intensity profile at the water surface was fundamentally altered by the introduction of diffractive optical elements. The homogeneity of the heat flux density at the water surface was improved significantly through this change in the experimental setup. The better homogeneity improved the accuracy of the measurements noticeably (see section 7.1.1).
Given the new homogeneity, the use of the ΔT method became possible (c.f. section 3.3.1). Compared to consecutive measurements with many different laser on-off excitation frequencies, as used for the amplitude damping method (section 3.3.2), heat transfer velocities can be obtained from only two excitation frequencies with this technique. The obtained results are in accordance with the results from the established amplitude damping analysis (c.f. section 7.1.3).
A new approach with a multifrequency excitation scheme (c.f. section 3.3.3)

has successfully been implemented and tested. This excitation scheme avoids biases in the measurement of two consecutively measured excitation frequencies during changing boundary conditions. The results of the new approach show nearly the same measurement accuracy as the amplitude damping method, but reduce the measurement time by a factor of 4 to 12 depending on wind speed (see section 7.1.3).

8.1.2. Systematic Study of Heat Exchange

Systematic laboratory measurements of the heat transfer velocity k_{heat} under a variety of conditions have been conducted for this thesis.

Clean Water

For clean deionized water recent measurements of Nagel [77, 78], could be confirmed. Only at small wind speeds deviations were found. These deviations have likely been caused by the experimental setup of Nagel and a detailed explanation for the found differences is given in section 7.2.1. The extension of the measurements to higher wind speeds did not reveal any unexpected phenomena and heat transfer velocities continue to increase with friction velocity.

Fetch Dependency

At low wind speeds k_{heat} increases with fetch length and shows a good correlation with the mean square slope (mss) of the water surface. At a certain fetch length both quantities start to decrease. The heat transfer velocities at low fetches are higher than those measured for infinite fetch. At higher wind speeds, both, k_{heat} and mss become increasingly insensitive to changes in the fetch length (see section 7.2.2). These observations have profound importance for all measurements conducted in linear wind-wave facilities.

Influence of Surfactants

Different concentrations of the artificial and soluble surfactant Triton X-100 have been added to deionized water in order to investigate the influence of surfactants on heat exchange (c.f. section 7.2.3). For very low wind speeds the presence of a surface film does not play an important role for heat transfer which stands in contrast to observations made for gas transfer. The insensitivity of heat transfer on surfactant concentration also holds true for high wind speeds. In an intermediate wind speed regime the onset of increased turbulence and wave development seems to be delayed as can be clearly seen by the significant reduction of the mean square slope of the water surface for a fixed wind speed if a surfactant is present. In this intermediate wind speed regime the slope $\beta^{-1}Sc^{-n}$ in the relationship $k_{heat} \propto u_* \beta^{-1}Sc^{-n}$, predicted by model descriptions (c.f. section 2.3), increases. For higher concentrations of the surfactant this change in slope shifts to higher friction velocities u_*. However, while in the intermediate and also in the high wind speed regime the correlation between mss and k_{heat} is good, at the lowest wind speeds the variation of k_{heat} for a nearly constant mss value can be as large as 40%. This suggests that mss is a suitable parameter for heat exchange only if waves are already present and not for the case of a completely smooth water surface.

8.1.3. Heat Exchange under Laboratory Sea Water Conditions

Heat transfer velocities measured during a measurement campaign with actual sea water from the North Sea in the Heidelberg Aeolotron are in agreement with the range of transfer velocities covered by common empirical wind speed parametrizations (c.f. section 7.3). The correlation between k_{heat} and mss is good, as soon as the water surface becomes rough. The natural surfactants potentially reduce heat transfer velocities slightly stronger than comparable concentrations of Triton X-100 at low wind speeds, although this cannot be concluded with certainty due to the necessity to correct the measured data for low wind speeds with an experimental procedure in the data analysis (see section 6.1.1). For intermediate and high wind speeds the difference vanishes.

8.1.4. Measurement Campaign in Marseille

At Pytheas in Marseille, the influence of breaking waves on heat transfer has been investigated. Breaking waves increase heat transfer velocities in an intermediate wind speed regime while at higher wind speeds the breaking does not enhance k_{heat} further (c.f. section 7.5).
Comparison of the development of k_{heat} with the friction velocity between the Marseille facility and the Heidelberg Aeolotron yields a good conformity.

8.1.5. Differentiating Gas Exchange Models

As originally proposed by Jähne [55] when introducing the controlled flux method, the measurement scheme with the amplitude damping can also be used to measure phase shifts between the laser's excitation signal and the temperature response of the water surface, as explained in section 3.3.2. This approach in theory allows for the differentiation of different gas exchange models. However, even with the improved homogeneity of the heat flux density in the present experimental setup no improvements in comparison to the measurements of Popp [85] could be achieved (c.f. section 7.6). His results were confirmed. A differentiation between gas exchange models from the controlled flux method seems impossible due to the intermittent character of the exchange process. However, a simple bi-modal description can explain the deviation between the phase shifts predicted by models and the actual measurement.

8.1.6. Comparison of Heat and Gas Exchange

Comparative measurements of heat and gas transfer have been conducted during the sea water measurement campaign (c.f. section 7.7). Those measurements found a general accordance of heat and gas transfer velocities scaled to the transfer velocity of a gas with the same Schmidt number. Small deviations at low wind speeds are attributed to systematic problems in the measurement setup. However, another series of comparative heat and gas transfer measurements conducted in October 2016 in the Aeolotron with an unidentified contamination of biological activity showed a deviation between the scaled transfer velocities of an astonishingly constant factor 2 independent on wind speed, where transfer velocities gained from heat transfer measurements are larger. This suggests that

under certain conditions heat and gas transfer behave differently (see section 7.7).

8.2. Outlook

8.2.1. Quantitative Comparison of Locally Measured Heat and Gas Exchange

Recent comparison between heat and gas transfer has either focused on comparing transfer velocities [78, 3] or on comparing structures caused by turbulence [63]. The drawback of the comparison of transfer velocities is that they compare locally measured heat transfer velocities with gas transfer velocities that are either measured globally across the whole water volume of a laboratory environment or on much larger spatial scales for field measurements. The comparison of images obtained from visualizations of local heat and gas transfer, however, lacks quantitative information about the amount of heat or gas exchanged, while it is good at investigating turbulent structures. With the new experimental setup a device for precise measurements of local heat transfer velocities with high temporal resolution is now available. Continuing recent experiments by Kräuter [63], Christine Kräuter and the author have conducted simultaneous and co-located measurements with the new thermographic setup during the clean water and fetch measurement conditions at the Aeolotron in summer 2015 (c.f. section 5.1). This data is currently analysed within the scope of another PhD thesis.
An additional series of simultaneous experiments is scheduled for the summer of 2017 where the boundary layer imaging technique will be extended by the use of oxygen as a second trace gas. Oxygen quenches the fluorescence of a ruthenium complex. This can be used to gain additional visual information about processes at the air-water interface. The oxygen quenching method has already demonstrated its capabilities for measuring concentration profiles, e.g. Friedl [33].
Combining the information gained from the pH indicator method used by Kräuter and the oxygen quenching technique, new ideas exist that are based on experiments conducted by the author [67] to extract actual gas exchange rates from the images. If this concept worked, it would be possible to compare not only turbulent structures but also transfer velocities for both, heat and gas, locally. The Schmidt number scaling procedure (c.f. section 2.5.3) also allows to extract the Schmidt number exponent if two transfer velocities of tracers with

different Schmidt numbers are measured. This could be exploited to derive the dependency of the Schmidt number exponent on fetch. Additionally, a method for the estimation of the local friction velocity from Garbe [37] is currently improved within the scope of a bachelor thesis, co-supervised by the author, and should complement the next series of experiments.

8.2.2. New Thermographic Setup as a Powerful Tool for Field Campaigns

The new experimental setup offers a measurement accuracy at a temporal and spatial resolution unprecedented by any other measurement technique available dedicated at measuring heat or gas transfer rates. The use of the new air-cooled CO_2 lasers also makes it a very compact device, as there is no more need for a large water cooling system, compared to the setup of Nagel [77]. Thus the new experimental setup provides an ideal tool for future field campaigns.

Bibliography

[1] W. Alpers and H. Hühnerfuss. "The damping of ocean waves by surface films: A new look at an old problem". In: *Journal of Geophysical Reseach* 94.C5 (1989), pp. 6251–6265. DOI: 10.1029/JC094iC05p06251.

[2] W. E. Asher, M. A. Atmane, and A. T. Jessup. "An Application of a Surface Penetration Model to Air–Water Gas Transfer". In: *37th International Liege Colloquium on Ocean Dynamics Gas Transfer at Water Surfaces*. 2005.

[3] W. E. Asher, A. T. Jessup, and M. A. Atmane. "Oceanic application of the active controlled flux technique for measuring air-sea transfer velocities of heat and gases". In: *J. Geophys. Res.* 109 (2004), C08S12. DOI: 10.1029/2003JC001862.

[4] W. E. Asher and J. F. Pankow. "The interaction of mechanically generated turbulence and interfacial films with a liquid phase controlled gas/liquid transport process". In: *Tellus* 38B (1986), pp. 305–318. DOI: 10.1111/j.1600-0889.1986.tb00256.x.

[5] W. Asher et al. "Statistics of surface divergence and their relation to air-water gas transfer velocity". In: *J. Geophys. Res.* 117.C5 (2012), p. C05035. DOI: 10.1029/2011JC007390.

[6] M. A. Atmane, W. Asher, and A. T. Jessup. "On the use of the active infrared technique to infer heat and gas transfer velocities at the air-water free surface". In: *J. Geophys. Res.* 109 (2004), C08S14. DOI: 10.1029/2003JC001805.

[7] M. L. Bender et al. "Evaluating gas transfer velocity parameterizations using upper ocean radon distributions". In: *J. Geophys. Res.* 116.C2 (2011), p. C02010. DOI: 10.1029/2009JC005805.

[8] E. J. Bock et al. "Relationship between air-sea gas transfer and short wind waves". In: *J. Geophys. Res.* 104.C11 (1999), pp. 25821–25831. DOI: 10.1029/1999JC900200.

[9] M. Bopp. "Messung der Schubspannungsgeschwindigkeit am Heidelberger Aeolotron mittels der Impulsbilanzmethode". Bachelor thesis. Institut für Umweltphysik, Fakultät für Physik und Astronomie, Univ. Heidelberg, 2011.

[10] M. Bopp. "Luft- und wasserseitige Strömungsverhältnisse im ringförmigen Heidelberger Wind-Wellen-Kanal (Aeolotron)". Masterarbeit. Institut für Umweltphysik, Universität Heidelberg, Germany, 2014. URL: http://www.ub.uni-heidelberg.de/archiv/17151.

[11] M. Bopp and B. Jähne. "Measurements of the friction velocity in the Heidelberg Aeolotron, a large annular wind-wave tank by the momentum balance method". In: *Tellus* In Preparation (2017).

[12] M. Bourassa et al. "Remotely sensed winds and wind stresses for marine forecasting and ocean modeling". In: *Proceedings of OceanObs'09: Sustained Ocean Observations and Information for Society*. Ed. by J. Hall, D. Harrison, and D. Stammer. Vol. 2. ESA Publication WPP-306, 2010. DOI: 10.5270/OceanObs09.cwp.08.

[13] H. C. Broecker, W. Siems, and J. Petermann. "The influence of wind on CO_2 exchange in a wind wave tunnel, including the effects of monolayers". In: *J. Mar. Res.* 36 (1978), pp. 595–610. DOI: 10.1007/978-94-009-4738-2_5.

[14] G. Caulliez. "Dissipation regimes for short wind waves". In: *J. Geophys. Res.* 118.2 (2013), pp. 672–684. DOI: 10.1029/2012JC008402.

[15] M. Coantic. "A model of gas transfer across air–water interfaces with capillary waves". In: *J. Geophys. Res.* 91 (1986), pp. 3925–3943. DOI: 10.1029/JC091iC03p03925.

[16] M. Coantic and P. Bonmarin. "The air-sea interaction simulation facility at the Institut de Mecanique Statistique de la Turbulence". In: *Atmospheric Technology* 7 (1975), pp. 72–79.

[17] J. Crank. *The Mathematics of Diffusion*. 2nd. Oxford: Clarendon Press, 1975.

[18] G. T. Csanady. "The role of breaking wavelets in air-sea gas transfer". In: *J. Geophys. Res.* 95.C1 (1990), pp. 749–759. DOI: 10.1029/JC095iC01p00749.

[19] E. L. Cussler. *Diffusion - Mass Transfer in Fluid Systems*. 3rd ed. Cambridge University Press, 2009.

[20] P. V. Danckwerts. "Significance of a liquid-film coefficients in gas absorption". In: *Ind. Eng. Chem.* 43 (1951), pp. 1460–1467. DOI: 10.1021/ie50498a055.

[21] E. L. Deacon. "Gas transfer to and across an air-water interface". In: *Tellus* 29 (1977), pp. 363–374. DOI: 10.1111/j.2153-3490.1977.tb00746.x.

[22] K. Degreif. "Untersuchungen zum Gasaustausch - Entwicklung und Applikation eines zeitlich aufgelösten Massenbilanzverfahrens". Dissertation. Institut für Umweltphysik, Fakultät für Physik und Astronomie, Univ. Heidelberg, 2006. URL: http://www.ub.uni-heidelberg.de/archiv/6120.

[23] W. Demtröder. *Experimentalphysik 2: Elektrizität und Optik*. 6th ed. Springer, 2013. DOI: 10.1007/978-3-642-29944-5.

[24] E. L. Dereniak and G. D. Boreman. *Infrared Detectors and Systems*. Wiley-Interscience, 1996.

[25] F. M. Dickey, L. S. Weichman, and R. N. Shagam. "Laser beam shaping techniques". In: *University of North Texas Libraries* (2000).

[26] S. C. Doney et al. "Ocean acidification: the other CO2 problem". In: *Annual Review of Marine Science* 1 (2009), pp. 169–192. DOI: 10.1146/annurev.marine.010908.163834.

[27] C. W. Fairall et al. "Cool-skin and warm-layer effects on sea surface temperature". In: *J. Geophys. Res.* 101.C1 (1996), pp. 1295–1308. DOI: 10.1029/95JC03190.

[28] A. E. Fick. "Über Diffusion". In: *Ann. Phys.* 170 (1855), pp. 59–86. DOI: 10.1002/andp.18551700105.

[29] N. M. Frew. "The role of organic films in air-aea gas exchange". In: *The Sea Surface and Global Change*. Ed. by P. S. Liss and R. A. Duce. Cambridge University Press, 1997, pp. 121–171. DOI: 10.1017/CBO9780511525025.006.

[30] N. M. Frew et al. "Impact of phytoplankton-generated surfactants on air-sea gas-exchange". In: *J. Geophys. Res.* 95.C3 (1990), pp. 3337–3352. DOI: 10.1029/JC095iC03p03337.

[31] N. Frew et al. "Air-sea gas transfer: Its dependence on wind stress, small-scale roughness, and surface films". In: *J. Geophys. Res.* 109 (2004), C08S17. DOI: 10.1029/2003JC002131.

[32] B. R. Frieden. "Lossless Conversion of a Plane Laser Wave to a Plane Wave of Uniform Irradiance". In: *Appl. Opt.* 4.11 (1965), pp. 1400–1403. DOI: 10.1364/AO.4.001400.

[33] F. Friedl. "Investigating the Transfer of Oxygen at the Wavy Air-Water Interface under Wind-Induced Turbulence". Dissertation. Institut für Umweltphysik, Fakultät für Physik und Astronomie, Univ. Heidelberg, 2013. URL: http://www.ub.uni-heidelberg.de/archiv/14582.

[34] F. Friedl, N. Krah, and B. Jähne. "Optical sensing of oxygen using a modified Stern-Volmer equation for high laser irradiance". In: *Sens. Actuators, B* 206 (2015), pp. 336–342. DOI: 10.1016/j.snb.2014.09.073.

[35] D. Friedman. "Infrared characteristics of ocean water (1.5 –15 μ)". In: *Appl. Opt.* 8 (1969), pp. 2073–2078. DOI: 10.1364/AO.8.002073.

[36] C. S. Garbe. "Measuring Heat Exchange Processes at the Air–Water Interface from Thermographic Image Sequence Analysis". Dissertation. IWR, Fakultät für Physik und Astronomie, Univ. Heidelberg, 2001. URL: http://www.ub.uni-heidelberg.de/archiv/1875.

[37] C. S. Garbe, K. Degreif, and B. Jähne. "Estimating the viscous shear stress at the water surface from active thermography". In: *Transport at the Air Sea Interface — Measurements, Models and Parameterizations*. Ed. by C. S. Garbe, R. A. Handler, and B. Jähne. Springer, 2007, pp. 223–239. DOI: 10.1007/978-3-540-36906-6_16.

[38] C. S. Garbe, U. Schimpf, and B. Jähne. "A surface renewal model to analyze infrared image sequences of the ocean surface for the study of air-sea heat and gas exchange". In: *J. Geophys. Res.* 109.C8 (2004), pp. 1–18. ISSN: 0148-0227. DOI: 10.1029/2003JC001802.

[39] C. S. Garbe, H. Spies, and B. Jähne. "Estimation of surface flow and net heat flux from infrared image sequences". In: *J. Math. Imaging Vision* 19.3 (2003), pp. 159–174. DOI: 10.1023/A:1026233919766.

[40] C. S. Garbe et al. "Transfer across the air-sea interface". In: *Ocean-Atmosphere Interactions of Gases and Particles*. Ed. by P. S. Liss and M. T. Johnson. Springer, 2014, pp. 55–112. DOI: 10.1007/978-3-642-25643-1_2.

[41] C. Haltebourg. "Modeling of Heat Exchange Across the Ocean Surface as Measured by Active Thermography". Dissertation. Institut für Umweltphysik, Fakultät für Physik und Astronomie, Univ. Heidelberg, 2017.

[42] P. Harriott. "A random eddy modification of the penetration theory". In: *Chem. Eng. Sci.* 17 (1962), pp. 149–154. DOI: 10.1016/0009-2509(62)80026-8.

[43] H. Haußecker. "Messung und Simulation von kleinskaligen Austauschvorgängen an der Ozeanoberfläche mittels Thermographie". Dissertation. IWR, Fakultät für Physik und Astronomie, Univ. Heidelberg, 1996. DOI: 10.5281/zenodo.14789.

[44] I. Herlina and G. H. Jirka. "Experiments on gas transfer at the air–water interface induced by oscillating grid turbulence". In: *J. Fluid Mech.* 594 (2008), pp. 183–208. DOI: 10.1017/S0022112007008968.

[45] R. Higbie. "The rate of absorption of a pure gas into a still liquid during short periods of exposure". In: *Trans. Am. Inst. Chem. Eng.* 31 (1935), pp. 365–389.

[46] D. T. Ho et al. "Toward a universal relationship between wind speed and gas exchange: Gas transfer velocities measured with 3He/SF6 during the Southern Ocean Gas Exchange Experiment". In: *J. Geophys. Res.* 116 (2011), C00F04. DOI: 10.1029/2010JC006854.

[47] H. Hühnerfuss. "Basic physicochemical principles of monomolecular sea slicks and crude oil spills". In: *Marine Surface Films*. Ed. by M. Gade, H. Hühnerfuss, and G. M. Korenowski. Springer, 2006, pp. 21–35.

[48] H. Hühnerfuss et al. "The damping of ocean surface waves by a monomolecular film measured by wave staffs and microwave radars". In: *J. Geophys. Res.* 86.C1 (1981), pp. 429–438. DOI: 10.1029/JC086iC01p00429.

[49] S. Hunklinger. *Festkörperphysik*. 4th ed. Oldenbourg Wissenschaftsverlag GmbH, 2014.

[50] B. Jähne. *Digitale Bildverarbeitung*. 7th ed. Springer, 2012. DOI: 10.1007/978-3-642-04952-1.

[51] B. Jähne. "Zur Parametrisierung des Gasaustauschs mit Hilfe von Laborexperimenten". Dissertation. Institut für Umweltphysik, 1980. DOI: 10.5281/zenodo.10443. URL: http://www.ub.uni-heidelberg.de/archiv/16796.

[52] B. Jähne and H. Haußecker. "Air-water gas exchange". In: *Annu. Rev. Fluid Mech.* 30 (1998), pp. 443–468. DOI: 10.1146/annurev.fluid.30.1.443.

[53] B. Jähne. "Air-sea gas exchange". In: *Encyclopedia Ocean Sciences*. Ed. by J. H. Steele, K. K. Turekian, and S. A. Thorpe. invited. Elsevier, 2009, pp. 147–156. DOI: 10.1016/B978-012374473-9.00642-1.

[54] B. Jähne. "Transfer processes across the free water interface". Habilitation thesis. Institut für Umweltphysik, Fakultät für Physik und Astronomie, Univ. Heidelberg, 1985. DOI: 10.5281/zenodo.12202. URL: http://www.ub.uni-heidelberg.de/archiv/16798.

[55] B. Jähne et al. "Investigating the transfer process across the free aqueous boundary layer by the controlled flux method". In: *Tellus* 41B.2 (1989), pp. 177–195. DOI: 10.1111/j.1600-0889.1989.tb00135.x.

[56] B. Jähne et al. “On the parameters influencing air-water gas exchange”. In: *J. Geophys. Res.* 92 (1987), pp. 1937–1950. DOI: 10.1029/JC092iC02p01937.

[57] B. Jähne et al. “The influence of intermittency on air/water gas transfer measurements”. In: *Transport at the Air Sea Interface — Measurements, Models and Parameterizations*. Ed. by C. S. Garbe, R. A. Handler, and B. Jähne. Springer, 2007. DOI: 10.1007/978-3-540-36906-6_18.

[58] B. Jähne et al. “Wind/wave-tunnel experiments on the Schmidt number and wave field dependence of air-water gas exchange”. In: *Gas transfer at water surfaces*. Ed. by W. Brutsaert and G. H. Jirka. Hingham, MA: Reidel, 1984, pp. 303–309. DOI: 10.1007/978-94-017-1660-4_28.

[59] M. Johnson et al. “A Rumsfeldian analysis of uncertainty in air-sea gas exchange”. In: *Gas Transfer at Water Surface 2010*. Kyoto: Kyoto University Press, 2011, pp. 464–484. URL: https://ueaeprints.uea.ac.uk/id/eprint/33094.

[60] D. Kiefhaber. “Optical Measurement of Short Wind Waves — from the Laboratory to the Field”. Dissertation. Institut für Umweltphysik, Fakultät für Physik und Astronomie, Univ. Heidelberg, 2014. URL: http://www.ub.uni-heidelberg.de/archiv/16304.

[61] D. Kiefhaber et al. “High-speed imaging of short wind waves by shape from refraction”. In: *Journal of the European Optical Society* 9 (2014), p. 14015. DOI: 10.2971/jeos.2014.14015.

[62] K. E. Krall. “Laboratory Investigations of Air-Sea Gas Transfer under a Wide Range of Water Surface Conditions”. Dissertation. Institut für Umweltphysik, Fakultät für Physik und Astronomie, Univ. Heidelberg, 2013. URL: http://www.ub.uni-heidelberg.de/archiv/14392.

[63] C. Kräuter. “Visualization of air-water gas exchange”. Dissertation. Institut für Umweltphysik, Fakultät für Physik und Astronomie, Univ. Heidelberg, 2015. URL: http://www.ub.uni-heidelberg.de/archiv/18209.

[64] M. Kropp. “Untersuchung des Wärmetransfers an der Wasseroberfläche in Abhängigkeit von der Wirklänge des Windes (Fetch) am Heidelberger Aeolotron”. Bachelor thesis. Institut für Umweltphysik, Fakultät für Physik und Astronomie, Univ. Heidelberg, 2015.

[65] P. W. Kruse. *Uncooled Thermal Imaging — Arrays, Systems, and Applications*. SPIE, 2001.

[66] P. K. Kundu. *Fluid Mechanics*. 4th. Academic Press, Elsevier, 2008.

[67] J. Kunz. "Visualisierung der wasserseitigen Massengrenzschicht beim konvektionsgetriebenen Gasaustausch mithilfe einer Lumineszenzmethode und Thermografie". Bachelor thesis. Institut für Umweltphysik, Fakultät für Physik und Astronomie, Univ. Heidelberg, 2011.

[68] C. Le Quéré et al. "Global carbon budget 2013". In: *Earth Syst. Sci. Data* 6.1 (2014), pp. 235–263. DOI: 10.5194/essd-6-235-2014.

[69] P. Libner. "Die Konstantflußmethode: Ein neuartiges, schnelles und lokales Meßverfahren zur Untersuchung von Austauschvorgängen an der Luft-Wasser Phasengrenze". Dissertation. Institut für Umweltphysik, Fakultät für Physik und Astronomie, Univ. Heidelberg, 1987. URL: http://d-nb.info/881465941.

[70] P. S. Liss and L. Merlivat. "Air-sea gas exchange rates: Introduction and synthesis". In: *The Role of Air-Sea Exchange in Geochemical Cycling*. Springer, 1986, pp. 113–129. DOI: 10.1007/978-94-009-4738-2_5.

[71] P. S. Liss and P. G. Slater. "Flux of gases across the air-sea interface". In: *Nature* 247 (1974), pp. 181–184. DOI: 10.1038/247181a0.

[72] P. Liss. "Gas transfer: Experiments and geochemical implications". In: *Air-Sea Exchange of Gases and Particles*. Ed. by P. Liss and W. Slinn. Springer, 1983, pp. 241–298.

[73] G. Marmorino and G. Smith G.B.;and Lindemann. "Infrared imagery of large-aspect-ratio Langmuir circulation". In: *Cont. Shelf Res.* 25 (2004). DOI: 10.1016/j.csr.2004.08.002.

[74] W. K. Melville, R. Shear, and F. Veron. "Laboratory measurements of the generation and evolution of Langmuir circulations". In: *J. Fluid Mech.* 364 (1998), pp. 31–58. DOI: 10.1017/S0022112098001098.

[75] W. Mischler. "Systematic Measurements of Bubble Induced Gas Exchange for Trace Gases with Low Solubilities". Dissertation. Institut für Umweltphysik, Fakultät für Physik und Astronomie, Univ. Heidelberg, 2014. URL: http://www.ub.uni-heidelberg.de/archiv/17720.

[76] T. Münsterer. "LIF Investigation of the Mechanisms Controlling Air–Water Mass Transfer at a Free Interface". Dissertation. Institut für Umweltphysik, Fakultät für Physik und Astronomie, Univ. Heidelberg, 1996. DOI: 10.5281/zenodo.14542.

[77] L. Nagel. "Active Thermography to Investigate Small-Scale Air-Water Transport Processes in the Laboratory and the Field". Dissertation. Institut für Umweltphysik, Fakultät für Chemie und Geowissenschaften, Univ. Heidelberg, 2014. URL: http://www.ub.uni-heidelberg.de/archiv/16831.

[78] L. Nagel, K. E. Krall, and B. Jähne. "Comparative heat and gas exchange measurements in the Heidelberg Aeolotron, a large annular wind-wave tank". In: *Ocean Sci.* 11 (2015), pp. 111–120. DOI: 10.5194/os-11-111-2015.

[79] R. Nielsen. "Gasaustausch - Entwicklung und Ergebnis eines schnellen Massenbilanzverfahrens zur Messung der Austauschparameter". Dissertation. Institut für Umweltphysik, Fakultät für Physik und Astronomie, Univ. Heidelberg, 2004. URL: http://www.ub.uni-heidelberg.de/archiv/5032.

[80] P. D. Nightingale et al. "In situ evaluation of air-sea gas exchange parameterization using novel conservation and volatile tracers". In: *Global Biogeochem. Cycles* 14 (2000), pp. 373–387. DOI: 10.1029/1999GB900091.

[81] J. C. Orr et al. "Anthropogenic ocean acidification over the twenty-first century and its impact on calcifying organisms". In: *Nature* 437.7059 (2005), pp. 681–686. URL: http://dx.doi.org/10.1038/nature04095.

[82] K. Pearson. "The problem of the random walk". In: *Nature* 72.294 (1905). URL: http://www.nature.com/physics/looking-back/pearson/index.html.

[83] W. L. Peirson. "Measurement of surface velocities and shears at a wavy air-water interface using particle image velocimetry." In: *Exp. Fluids* 23 (1997), pp. 427–437. DOI: 10.1007/s003480050131.

[84] T. H. Peng et al. "Radon evasion rates in the Atlantic and Pacific oceans as determined during the geosecs program". In: *J. Geophys. Res.* 84.C5 (1979), pp. 2471–2487. DOI: 10.1029/JC084iC05p02471.

[85] C. J. Popp. "Untersuchung von Austauschprozessen an der Wasseroberfläche aus Infrarot-Bildsequenzen mittels frequenzmodulierter Wärmeeinstrahlung". Dissertation. Institut für Umweltphysik, Fakultät für Physik und Astronomie, Univ. Heidelberg, 2006. URL: http://www.ub.uni-heidelberg.de/archiv/6489.

[86] L. Prandtl. *Führer durch die Strömungslehre*. 9th ed. Vieweg, 1990. DOI: 10.1007/978-3-322-99491-2.

[87] C. Proß. "Analysis of Fetch Dependency of the Slope of Wind-Water Waves". Bachelor thesis. Institut für Umweltphysik, Fakultät für Physik und Astronomie, Univ. Heidelberg, 2016.

[88] H. Reichardt. "Vollständige Darstellung der turbulenten Geschwindigkeitsverteilung in glatten Leitungen". In: *Zeitschrift für angewandte Mathematik und Mechanik* 31 (1951), pp. 208–219. DOI: 10.1002/zamm.19510310704.

[89] W. Roether and B. Kromer. "Optimum application of the radon deficit method to obtain air–sea gas exchange rates". In: *Gas transfer at water surfaces*. Ed. by W. Brutsaert and G. H. Jirka. Springer Netherlands, 1984, pp. 447–457. DOI: 10.1007/978-94-017-1660-4_41.

[90] P. M. Saunders. "The temperature at the ocean-air interface". In: *Journal of Atmospherical Sciences* 24.3 (1967), pp. 269–273. DOI: 10.1175/1520-0469(1967)024<0269:TTATOA>2.0.CO;2.

[91] U. Schimpf. "Untersuchung des Gasaustausches und der Mikroturbulenz an der Meeresoberfläche mittels Thermographie". Dissertation. Institut für Umweltphysik, Fakultät für Physik und Astronomie, Univ. Heidelberg, 2000. URL: http://www.ub.uni-heidelberg.de/archiv/545.

[92] U. Schimpf, C. Garbe, and B. Jähne. "Investigation of transport processes across the sea surface microlayer by infrared imagery". In: *J. Geophys. Res.* 109.C8 (2004), C08S13. DOI: 10.1029/2003JC001803.

[93] U. Schimpf, L. Nagel, and B. Jähne. "First results of the 2009 sopran active thermography pilot experiment in the baltic sea". In: *Gas Transfer at Water Surfaces 2010*. Ed. by S. Komori, W. McGillis, and R. Kurose. 2011, pp. 358–367. DOI: 10.5281/zenodo.14956. URL: http://hdl.handle.net/2433/156156.

[94] J. Schnieders. "Analyzing the footprints of turbulence producing mechanisms at the free water surface". Dissertation. Institut für Umweltphysik, Fakultät für Physik und Astronomie, Univ. Heidelberg, 2015. URL: http://www.ub.uni-heidelberg.de/archiv/18469.

[95] J. Schnieders et al. "Analyzing the footprints of near surface aqueous turbulence - an image processing based approach". In: *J. Geophys. Res.* 118 (2013), pp. 1272–1286. DOI: 10.1002/jgrc.20102.

[96] K. Schwarz. "Spatio-Temporal Measurements of Water-Wave Height and Slope using Laser-Induced Fluorescence and Splines". Bachelor thesis. Institut für Umweltphysik, Fakultät für Physik und Astronomie, Univ. Heidelberg, 2016.

[97] T. Springer and R. Pigford. "Influence of surface turbulence and surfactants on gas transport through liquid interfaces". In: *Ind. Eng. Chem. Fundam.* 9 (1970), pp. 458–465. DOI: 10.1021/i160035a025.

[98] C. Sweeney et al. "Constraining global air-sea gas exchange for CO_2 with recent bomb ^{14}C measurements". In: *Global Biogeochem. Cycles* 21 (2007), B2015. DOI: 10.1029/2006GB002784.

[99] R. Upstill-Goddard et al. “Bacterioneuston control of air-water methane exchange determined with a laboratory gas exchange tank”. In: *Global Biogeochem. Cycles* 17.4 (2003), p. 1108. DOI: 10.1029/2003GB002043.

[100] F. Veron and W. K. Melville. “Experiments on the stability and transition of wind-driven water surfaces”. In: *J. Fluid Mech.* 446 (2001), pp. 25–65. DOI: 10.1017/S0022112001005638.

[101] M. Vollmer and K.-P. Möllmann. *Infrared Thermal Imaging: Fundamentals, Research and Applications*. Weinheim: Wiley-VCH, 2010.

[102] R. Wanninkhof. “Relationship between wind speed and gas exchange over the ocean”. In: *J. Geophys. Res.* 97 (1992), pp. 7373–7382. DOI: 10.1029/92JC00188.

[103] R. Wanninkhof and W. R. McGillis. “A cubic relationship between gas transfer and wind speed.” In: *Geophys. Res. Lett.* 26 (1999), pp. 1889–1892. DOI: 10.1029/1999GL900363.

[104] R. Wanninkhof et al. “Advances in quantifying air-sea gas exchange and environmental forcing”. In: *Annual Review of Marine Science* 1 (2009), pp. 213–244. DOI: 10.1146/annurev.marine.010908.163742.

[105] R. Wanninkhof et al. “Gas transfer experiment on Georges Bank using two volatile deliberate tracers”. In: *J. Geophys. Res.* 98.C11 (1993), pp. 20237–20248. DOI: 10.1029/93JC01844.

[106] A. J. Watson, R. C. Upstill-Goddard, and P. S. Liss. “Air-sea exchange in rough and stormy seas measured by a dual tracer technique”. In: *Nature* 349.6305 (1991), pp. 145–147. DOI: 10.1038/349145a0.

[107] W. G. Whitman. “The two-film theory of gas absorption”. In: *Chemical and Metallurgical Engineering* 29.4 (1923), pp. 146–148.

[108] D. M. Wieliczka, S. Weng, and M. R. Querry. “Wedge shaped cell for highly absorbent liquids: infrared optical constants of water”. In: *Appl. Opt.* 28.9 (1989), pp. 1714–1719. DOI: 10.1364/AO.28.001714.

[109] O. Wurl and J. P. Obbard. “A review of pollutants in the sea-surface microlayer (SML): a unique habitat for marine organisms”. In: *Mar. Pollut. Bull.* 48.11–12 (2004), pp. 1016–1030. DOI: http://dx.doi.org/10.1016/j.marpolbul.2004.03.016.

[110] O. Wurl et al. “Formation and global distribution of sea-surface microlayers”. In: *Biogeosciences* 8 (2011), pp. 121–135. DOI: 10.5194/bg-8-121-2011.

[111] A. M. Yaglom and B. A. Kader. "Heat and mass transfer between a rough wall and turbulent fluid flow at high Reynolds and Peclet numbers". In: *J. Fluid Mech.* 62 (1974), pp. 601–623. DOI: https://doi.org/10.1017/S0022112074000838.

[112] C. L. Yaws. *Chemical Properties Handbook: physical, thermodynamic, environmental, transport, safety, and health related properties for organic and inorganic chemicals*. McGraw-Hill, 1999.

[113] C. L. Young, ed. *IUPAC Solubility Data Series: Oxides of Nitrogen*. Vol. 8. Pergamon Press, 1981.

[114] C. J. Zappa, W. E. Asher, and A. T. Jessup. "Microscale wave breaking and air-water gas transfer". In: *J. Geophys. Res.* 106.C5 (2001), pp. 9385–9391. DOI: 10.1029/2000JC000262.

[115] C. J. Zappa et al. "Microbreaking and the enhancement of air-water transfer velocity". In: *Journal of Geophysical Research: Oceans* 109.C8 (2004). C08S16, n/a–n/a. DOI: 10.1029/2003JC001897. URL: http://dx.doi.org/10.1029/2003JC001897.

Appendix A

A.1. Tables of the Results of all Measurements

This section lists the tables with the numerical results from the measurements conducted within the scope of this thesis. Note that instead of the reference wind speed, the wind speed is given as the frequency of the electronic frequency converter for the wind turbines in the Aeolotron. This is intended to facilitate internal use of our working group. The corresponding reference wind speeds are listed in the tables in section 5. Note that the values for the friction velocity and for the mean square slope are listed with the full number of digits as they were provided to the author. The heat transfer velocities listed here also still show all digits obtained during the data processing scheme as described in section 6 and no rounding to integers has been applied. This should however not pretend that the measurements have an accuracy to this level.

Table A.1.: Results of the clean water measurement conditions.

date	time of day	wind speed [Hz]	fetch [m]	c_{Triton}	mss	u_* [cm/s]	Δu_* [cm/s]	k_{heat} [cm/h]	Δk_{heat} [cm/h]
19.06.2015	11:41 - 14:25	5.0	∞	0g/180001	0.005352	0.335	0.021	54.46247	3.65331
19.06.2015	14:25 - 16:21	7.9	∞	0g/180001	0.010922	0.441	0.026	76.16352	3.1054
19.06.2015	16:21 - 17:30	12.6	∞	0g/180001	0.018232	0.621	0.038	112.36394	4.89517
19.06.2015	17:30 - 18:28	15.8	∞	0g/180001	0.045032	0.810	0.052	207.09423	7.3659
19.06.2015	18:28 - 19:30	25.1	∞	0g/180001	0.104728	1.552	0.097	517.31026	16.95933
19.06.2015	19:30 - 20:31	39.7	∞	0g/180001	0.167363	3.164	0.184	1039.44115	126.65911
22.06.2015	10:36 - 12:17	6.3	∞	0g/180001	0.008933			67.40058	3.59806
22.06.2015	12:17 - 14:06	10.0	∞	0g/180001	0.012295	0.519	0.031	92.34112	3.74544
22.06.2015	14:06 - 15:16	12.6	∞	0g/180001	0.016454	0.621	0.038	115.4495	4.9356
22.06.2015	15:16 - 16:11	19.9	∞	0g/180001	0.071888	1.079	0.070	366.00473	10.31184
22.06.2015	16:11 - 17:10	31.5	∞	0g/180001	0.142629	2.149	0.140	702.62728	36.01869
22.06.2015	17:10 - 18:03	50.0	∞	0g/180001	0.190462	3.983	0.297	1595.79027	716.53565

Table A.2.: Results of the measurements with fetch variation.

date	time of day	wind speed [Hz]	fetch [m]	c_{Triton}	mss	k_{heat} [cm/h]	Δk_{heat} [cm/h]
15.07.2015	11:57 - 13:32	15.8	2	0g/180001	0.044695	283.36431	16.56044
15.07.2015	13:46 - 14:34	15.8	4	0g/180001	0.048688	272.65524	13.21397
15.07.2015	14:39 - 15:28	15.8	7	0g/180001	0.055346	298.74337	11.44078
15.07.2015	15:32 - 16:21	15.8	12	0g/180001	0.059303	296.48153	18.66943
15.07.2015	16:24 - 17:15	15.8	16	0g/180001	0.057624	264.54921	11.24373
15.07.2015	17:17 - 18:05	15.8	20.7	0g/180001	0.051756	264.80048	11.30885
16.07.2015	9:29 - 10:19	19.9	2	0g/180001	0.062285	360.79248	12.60223
16.07.2015	10:24 - 10:59	19.9	4	0g/180001	0.064905	383.87791	13.07404
16.07.2015	11:03 - 11:38	19.9	7	0g/180001	0.068988	440.76848	37.02231
16.07.2015	11:41 - 12:17	19.9	12	0g/180001	0.072187	361.89316	24.62832
16.07.2015	12:20 - 12:53	19.9	16	0g/180001	0.078727	360.04685	14.62425
16.07.2015	12:56 - 13:32	19.9	20.7	0g/180001	0.076316	357.52176	13.12503
16.07.2015	13:43 - 14:30	25.1	2	0g/180001	0.076051	524.63665	25.7508
16.07.2015	14:34 - 15:08	25.1	4	0g/180001	0.091512	550.5759	23.38801
16.07.2015	15:12 - 15:47	25.1	7	0g/180001	0.095528	520.08526	25.72976
16.07.2015	15:50 - 16:24	25.1	12	0g/180001	0.103455	547.6637	24.78716
16.07.2015	16:27 - 17:01	25.1	16	0g/180001	0.114778	522.79304	24.1462
16.07.2015	17:04 - 17:38	25.1	20.7	0g/180001	0.107174	482.72322	16.37532
17.07.2015	10:18 - 12:13	10.0	2	0g/180001	0.001596	92.00869	4.55277
17.07.2015	12:23 - 13:41	10.0	4	0g/180001	0.007308	122.92265	3.95321
17.07.2015	13:47 - 15:05	10.0	7	0g/180001	0.014808	130.04784	3.14047
17.07.2015	15:12 - 16:30	10.0	12	0g/180001	0.024797	144.02163	3.32113
17.07.2015	16:36 - 17:54	10.0	16	0g/180001	0.030943		
17.07.2015	18:01 - 19:19	10.0	20.7	0g/180001	0.034917	142.72641	5.29773
20.07.2015	9:44 - 10:42	12.6	2	0g/180001	0.023918	187.92327	3.96446
20.07.2015	10:50 - 11:38	12.6	4	0g/180001	0.028402	189.86936	4.08194
20.07.2015	11:41 - 12:29	12.6	7	0g/180001	0.036121	202.12623	5.14578
20.07.2015	12:32 - 13:20	12.6	12	0g/180001	0.04685	226.49236	9.48946
20.07.2015	13:25 - 14:13	12.6	16	0g/180001	0.048552	210.50154	9.75636
20.07.2015	14:16 - 15:05	12.6	20.7	0g/180001	0.03887	175.00182	8.89534
20.07.2015	15:14 - 17:09	10.0	16	0g/180001	0.033633	153.50676	7.69181

Table A.3.: Results from the measurements with 0.6 g Triton X-100 per 18000 l of deionized water in the Aeolotron.

date	time of day	wind speed [Hz]	fetch [m]	c_{Triton}	mss	u_* [cm/s]	Δu_* [cm/s]	k_{heat} [cm/h]	Δk_{heat} [cm/h]
11.08.2015	10:28 - 12:36	5.0	∞	0.6g/18000l	0.000946	0.159	0.017	62.92933	3.95338
11.08.2015	12:36 - 14:24	7.9	∞	0.6g/18000l	0.004832	0.316	0.020	77.10372	3.78383
11.08.2015	14:24 - 15:42	12.6	∞	0.6g/18000l	0.009797	0.537	0.032	106.82037	4.8634
11.08.2015	15:42 - 16:49	15.8	∞	0.6g/18000l	0.019122	0.706	0.044	132.3663	4.82274
11.08.2015	16:49 - 17:40	25.1	∞	0.6g/18000l	0.098903	1.478	0.094	438.12062	19.07918
11.08.2015	17:40 - 18:19	39.7	∞	0.6g/18000l	0.163587	3.017	0.184	904.41816	79.98618
12.08.2015	10:07 - 12:20	6.3	∞	0.6g/18000l	0.002045	0.227	0.017	69.18755	4.01636
12.08.2015	12:20 - 14:16	10.0	∞	0.6g/18000l	0.00779	0.424	0.025	92.32983	4.51256
12.08.2015	16:16 - 15:32	12.6	∞	0.6g/18000l	0.010284	0.539	0.032	106.76371	4.1812
12.08.2015	15:32 - 16:31	19.9	∞	0.6g/18000l	0.062817	0.987	0.064	285.41015	15.05583
12.08.2015	16:31 - 17:23	31.5	∞	0.6g/18000l	0.137669	2.074	0.137	655.43638	42.05
12.08.2015	17:23 - 17:49	50.0	∞	0.6g/18000l	0.182632	3.965	0.282	939.12208	231.0084

Table A.4.: Results from the measurements with 3 g Triton X-100 per 18000 l of deionized water in the Aeolotron.

date	time of day	wind speed [Hz]	fetch [m]	c_{Triton}	mss	u_* [cm/s]	Δu_* [cm/s]	k_{heat} [cm/h]	Δk_{heat} [cm/h]
13.08.2015	10:22 - 13:06	5.0	∞	3g/18000l	0.001074	0.159	0.017	62.06598	3.97337
13.08.2015	13:06 - 15:20	7.9	∞	3g/18000l	0.001128	0.276	0.019	77.9395	3.83193
13.08.2015	15:20 - 16:28	12.6	∞	3g/18000l	0.005943	0.504	0.030	102.65613	5.09447
13.08.2015	16:28 - 17:33	15.8	∞	3g/18000l	0.00672	0.504	0.030	124.57375	4.41112
13.08.2015	17:33 - 18:24	25.1	∞	3g/18000l	0.082631	1.333	0.083	313.8609	15.26832
13.08.2015	18:24 - 18:58	39.7	∞	3g/18000l	0.162741	3.005	0.168	790.79716	49.16981
14.08.2015	10:10 - 12:24	6.3	∞	3g/18000l	0.001011	0.187	0.017	75.28015	4.64753
14.08.2015	12:24 - 14:23	10.0	∞	3g/18000l	0.003789	0.388	0.023	90.13932	4.02752
14.08.2015	14:23 - 15:41	12.6	∞	3g/18000l	0.005729	0.502	0.030	106.76251	5.26118
14.08.2015	15:41 - 16:32	19.9	∞	3g/18000l	0.019323	0.831	0.053	154.0912	6.90425
14.08.2015	16:32 - 17:23	31.5	∞	3g/18000l	0.131217	2.011	0.131	570.22208	34.21145
14.08.2015	17:23 - 17:50	50.0	∞	3g/18000l	0.185675	3.951	0.281	923.39977	234.8631

Table A.5.: Results from the measurements with 15 g Triton X-100 per 18000 l of deionized water in the Aeolotron.

date	time of day	wind speed [Hz]	fetch [m]	c_{Triton}	mss	u_* [cm/s]	Δu_* [cm/s]	k_{heat} [cm/h]	Δk_{heat} [cm/h]
19.08.2015	9:15 - 11:33	5.0	∞	15g/18000l	0.000957	0.139	0.017	62.6411	4.2952
19.08.2015	11:33 - 13:52	7.9	∞	15g/18000l	0.001136	0.286	0.019	78.40799	4.169
19.08.2015	13:52 - 15:08	12.6	∞	15g/18000l	0.001049	0.444	0.026	104.30308	4.91246
19.08.2015	15:08 - 16:23	15.8	∞	15g/18000l	0.00104	0.543	0.032	121.9661	5.28821
19.08.2015	16:23 - 17:37	25.1	∞	15g/18000l	0.012961	0.973	0.063	185.9413	8.80397
19.08.2015	17:37 - 18:27	39.7	∞	15g/18000l	0.1535	2.984	0.188	719.40979	109.84226
21.08.2015	9:09 - 11:33	6.3	∞	15g/18000l	0.000934	0.185	0.017	75.2408	4.24547
21.08.2015	11:33 - 13:45	10.0	∞	15g/18000l	0.001024	0.350	0.021	83.51491	4.78078
21.08.2015	13:45 - 14:53	12.6	∞	15g/18000l	0.001548	0.442	0.026	103.77812	4.93776
21.08.2015	14:53 - 15:50	19.9	∞	15g/18000l	0.004197	0.710	0.045	143.80307	6.09942
21.08.2015	15:50 - 16:41	31.5	∞	15g/18000l	0.112596	1.980	0.118	427.35129	35.84061
21.08.2015	16:41 - 17:28	50.0	∞	15g/18000l	0.177761	4.145	0.363	1253.54309	502.91042

Table A.6.: Results from the sea water measurement campaign in the Aeolotron in November 2014.

condition	data	wind speed [Hz]	fetch [m]	c_{Triton} [g/18000l]	mss	u_* [cm/s]	u_{10} [m/s]	k_{heat} [cm/h]
1	04.11.2014	5.0	∞	21.0 ± 6.7	0.0002926			34.70083 ± 2.47253
2	04.11.2014	7.9	∞	8.5 ± 0.8	0.0005729			48.82995 ± 3.46305
3	04.11.2014	12.6	∞	10.6 ± 0.4	0.000311	0.408 ± 0.024	3.980 ± 0.252	67.12442 ± 4.74034
4	04.11.2014	15.8	∞	8.2 ± 0.2	0.0003405	0.539 ± 0.032	5.376 ± 0.346	82.62608 ± 5.81683
5	04.11.2014	25.1	∞	17.3 ± 0.7	0.1026	1.44 ± 0.085	11.068 ± 0.474	
6	04.11.2014	39.7	∞	13.9 ± 1.3	0.168	2.858 ± 0.207	17.892 ± 0.874	760.49873 ± 53.23648
7	06.11.2014	6.3	∞	18.3 ± 0.7	0.0004318	0.224 ± 0.017	2.092 ± 0.175	39.91884 ± 2.84896
8	06.11.2014	10.0	∞	9.4 ± 0.8	0.0003283	0.356 ± 0.022	3.437 ± 0.226	53.79845 ± 3.81962
9	06.11.2014	12.6	∞	11.0 ± 1.0	0.000649	0.439 ± 0.026	4.305 ± 0.276	67.96637 ± 4.79801
10	06.11.2014	19.9	∞	6.9 ± 0.3	0.05299	0.976 ± 0.067	8.306 ± 0.429	266.99437 ± 18.70127
11	06.11.2014	31.5	∞	9.4 ± 0.1	0.1368	2.031 ± 0.131	14.145 ± 0.640	587.84542 ± 41.1517
12	11.11.2014	5.0	∞	34.7 ± 7.8	0.0003598	0.168 ± 0.017	1.536 ± 0.163	34.90884 ± 2.46586
13	11.11.2014	7.9	∞	12.3 ± 0.3		0.255 ± 0.018	2.404 ± 0.185	49.87619 ± 3.55147
14	11.11.2014	12.6	∞	10.5 ± 0.4	0.0003648	0.416 ± 0.025	4.072 ± 0.260	70.35369 ± 4.95867
15	11.11.2014	15.8	∞	9.2 ± 0.4	0.0004604	0.531 ± 0.031	5.291 ± 0.336	86.28717 ± 6.06583
16	11.11.2014	25.1	∞	9.0 ± 0.0	0.09395	1.442 ± 0.089	11.080 ± 0.495	471.4524 ± 33.00327
17	13.11.2014	6.3	∞	13.2 ± 0.4	0.0003367	0.181 ± 0.017	1.663 ± 0.168	35.65384 ± 2.69677
18	13.11.2014	10.0	∞	8.7 ± 0.6	0.0003679	0.303 ± 0.019	2.890 ± 0.199	44.75253 ± 3.49932
19	13.11.2014	12.6	∞	9.3 ± 0.6	0.0004171	0.402 ± 0.024	3.925 ± 0.252	60.79584 ± 4.49814
20	13.11.2014	19.9	∞	7.9 ± 0.4	0.05202	0.934 ± 0.059	8.033 ± 0.389	155.93609 ± 10.9788
21	13.11.2014	19.9	∞	7.9 ± 0.4	0.05202	0.934 ± 0.059	13.955 ± 0.646	324.45989 ± 22.73198
22	13.11.2014	31.5	∞	10.5 ± 0.5	0.1299	1.993 ± 0.131	18.208 ± 0.816	
23	13.11.2014	39.7	∞	8.1 ± 0.6	0.1492	2.933 ± 0.195		
24	19.11.2014	5.0	∞	13.5 ± 0.8				31.02328 ± 2.34386
25	19.11.2014	7.9	∞	10.6 ± 1.1	0.0003748	0.264 ± 0.018	2.490 ± 0.187	41.63165 ± 3.40855
26	19.11.2014	12.6	∞	11.5 ± 0.7	0.0004822	0.423 ± 0.025	4.137 ± 0.261	61.30345 ± 4.48132
27	19.11.2014	15.8	∞	10.3 ± 0.4	0.004466	0.529 ± 0.032	5.267 ± 0.338	82.87816 ± 5.91999
28	19.11.2014	25.1	∞	11.4 ± 1.6	0.08261	1.459 ± 0.090	11.174 ± 0.500	418.22438 ± 29.29978
29	19.11.2014	39.7	∞	9.0 ± 0.2	0.1267	2.964 ± 0.192	18.340 ± 0.801	831.15392 ± 58.182

Table A.7.: Results from the sea water measurement campaign in the Aeolotron in November 2014.

condition	data	wind speed [Hz]	fetch [m]	c_{Triton} [g/18000l]	mss	u_* [cm/s]	u_{10} [m/s]	k_{heat} [cm/h]
30	21.11.2014	6.3	∞	12.4 ± 0.9	0.0003635	0.173 ± 0.017	1.580 ± 0.166	39.88065 ± 2.99716
31	21.11.2014	10.0	∞	10.4 ± 1.0	0.0003796	0.309 ± 0.020	2.954 ± 0.205	51.94811 ± 3.87697
32	21.11.2014	12.6	∞	10.5 ± 1.1	0.0004227	0.386 ± 0.023	3.755 ± 0.240	65.78575 ± 4.73539
33	21.11.2014	19.9	∞	7.3 ± 0.7	0.05351	0.964 ± 0.060	8.228 ± 0.390	316.59847 ± 22.17425
34	21.11.2014	31.5	∞	5.4 ± 0.5		1.993 ± 0.128	13.956 ± 0.631	
35	21.11.2014	50.0	∞	4.8 ± 0.7		3.919 ± 0.306	22.468 ± 1.312	
36	24.11.2014	5.0	∞	8.1 ± 0.6	0.001324	0.152 ± 0.017	1.371 ± 0.164	36.21751 ± 2.66094
37	24.11.2014	7.9	∞	6.3 ± 0.5	0.003522	0.152 ± 0.017	1.371 ± 0.164	51.32424 ± 3.72562
38	24.11.2014	12.6	∞	6.0 ± 0.3	0.008953	0.46 ± 0.027	4.529 ± 0.287	68.91313 ± 4.92589
39	24.11.2014	15.8	∞	4.9 ± 0.3	0.01265	0.607 ± 0.037	6.099 ± 0.395	91.99778 ± 6.61806
40	24.11.2014	25.1	∞	6.4 ± 0.6	0.07715	1.479 ± 0.089	11.283 ± 0.491	418.40867 ± 29.31029
41	24.11.2014	39.7	∞	9.3 ± 1.0		3.04 ± 0.202	18.652 ± 0.830	
42	26.11.2014	5.0	∞	4.9 ± 0.4	0.0003135	0.158 ± 0.017	1.438 ± 0.163	37.29048 ± 2.70059
43	26.11.2014	7.9	∞	4.5 ± 0.1	0.0003263	0.279 ± 0.019	2.645 ± 0.197	48.48268 ± 3.64096
44	26.11.2014	12.6	∞	7.1 ± 0.6	0.0003998	0.435 ± 0.026	4.269 ± 0.273	63.55852 ± 4.64947
45	26.11.2014	15.8	∞	5.5 ± 0.3	0.0009757	0.539 ± 0.032	5.375 ± 0.343	79.33233 ± 5.7461
46	26.11.2014	25.1	∞	6.1 ± 0.4	0.07382	1.494 ± 0.090	11.369 ± 0.495	442.00648 ± 30.95187
47	26.11.2014	39.7	∞	6.0 ± 0.6	0.116	2.914 ± 0.209	18.130 ± 0.877	
48	29.11.2014	6.3	∞	5.6 ± 0.3	0.000313			38.76423 ± 2.96549
49	29.11.2014	10.0	∞	9.8 ± 0.6	0.0003336	0.308 ± 0.020	2.945 ± 0.207	50.59089 ± 3.80388
50	29.11.2014	12.6	∞	10.1 ± 1.0	0.0003477	0.39 ± 0.023	3.790 ± 0.244	66.34089 ± 4.80318
51	29.11.2014	19.9	∞	6.5 ± 0.4	0.05101	0.957 ± 0.060	8.184 ± 0.388	149.73 ± 3.22723
52	29.11.2014	31.5	∞	9.0 ± 0.7	0.1096	2.029 ± 0.128	14.132 ± 0.627	
53	29.11.2014	50.0	∞	6.1 ± 0.6	0.1272	4.008 ± 0.307	22.848 ± 1.304	

Table A.8.: Results from the measurement campaign with unknown biological activity in the Aeolotron in October 2016.

date	wind speed [Hz]	fetch [m]	mss	k_{heat} [cm/h]
12.10.2016	39.7	∞		1093.38793 ± 240.17354
14.10.2016	12.6	∞		115.45366 ± 4.10562
17.10.2016	19.9	∞	0.08778	374.54085 ± 14.72037
18.10.2016	31.5	∞	0.17341	690.46048 ± 75.01821
19.10.2016	15.8	∞	0.03556	160.61648 ± 4.67263
21.10.2016	10	∞	0.00926	98.29482 ± 3.30787

Table A.9.: Results from the measurement campaign at Pytheas in Marseille in June 2016.

only wind						
date	u_{ref} [m/s]	fetch [m]	paddle freq. [Hz]	mss	u_* [cm/s]	k_{heat} [cm/h]
15.06.2016	2.5	27	0	1.12212	0.26879	65.63767 $\pm$ 1.44271
16.06.2016	3.0	27	0	1.40772	0.34785	70.79523 $\pm$ 1.65917
17.06.2016	4.0	27	0	1.77204	0.50596	101.85129 $\pm$ 3.47102
14.06.2016	5.0	27	0	2.21233	0.64827	126.26338 $\pm$ 5.13889
03.06.2016	10.0	27	0	6.542	1.51789	379.23267 $\pm$ 6.13958
10.06.2016	12.0	27	0	8.13793	1.92899	453.17845 $\pm$ 10.26386

paddle conditions with regular wave field					
date	u_{ref} [m/s]	fetch [m]	paddle freq. [Hz]	mss	k_{heat} [cm/h]
08.06.2016	6.0	27	1.1	4.63	145.02086 $\pm$ 10.82396
10.06.2016	12.0	27	0.9	7.656	452.11861 $\pm$ 65.04863
10.06.2016	8.0	27	0.9		282.09 $\pm$ 11.58746

paddle conditions with enhanced wave breaking					
date	u_{ref} [m/s]	fetch [m]	paddle freq. [Hz]	mss	k_{heat} [cm/h]
21.06.2016	6.0	27	1.3	5.004	223.15247 $\pm$ 6.42436
20.06.2016	10.0	27	1.3	7.571	412.64805 $\pm$ 85.80588

paddle conditions with enhanced wave breaking and 55 ppmv of butanol					
date	u_{ref} [m/s]	fetch [m]	paddle freq. [Hz]	mss	k_{heat} [cm/h]
22.06.2016	6.0	27	1.3	4.594	242.47553 $\pm$ 18.35859
23.06.2016	10.0	27	1.3	7.492	386.39806 $\pm$ 32.18237

A.2. Estimating Heat Flux Variations

The calculations underlying the considerations for the optimal combination of two separate laser intensity profiles into one large intensity profile for the experimental setup in Marseille are presented here (c.f. section 4.2.2). The results are shown in figure 4.12.

Incident Laser Beams without Inclination to the Water Surface

For the case of two laser beams that shine down straight vertically onto the water surface, i.e. the case represented in figure 4.12 (a), (c) and (e), the heat flux density is constructed of two independent intensity profiles with a homogeneous intensity of one. The simple assumption of a sinusoidal displacement of the whole water surface is made to simulate a wave. For the maximal wave height of 0.1 m the single intensity profiles have the smallest elongation. This case is shown in figure A.1. The elongation of these intensity profiles is calculated via

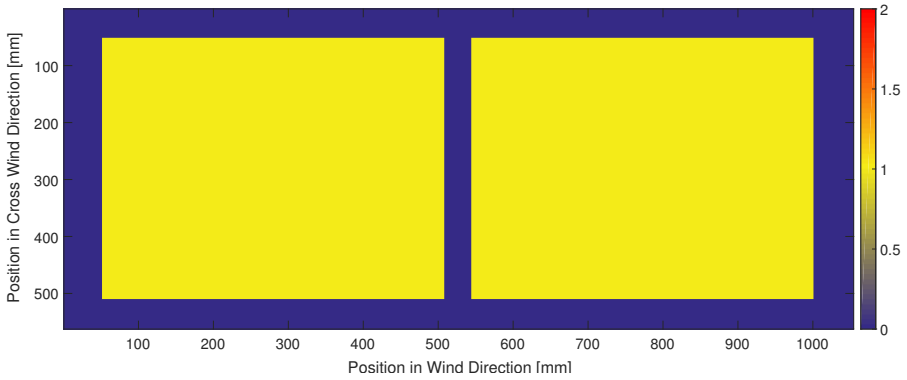

Figure A.1.: Artificial intensity distribution at the water surface for a distance of 1.3 m between the beam shaping element and the water surface. This corresponds to the distance between the beam shaping element and the crest of the largest waves observed in the Marseille facility. The colour corresponds to the artificial intensity.

simple geometrical considerations: The distance from the beam shaping element to the water surface at rest d_0 is 1.4 m. The complete opening angle 2α of the

beam shaping element is 19.92°. This yields for the elongation L_{wind} in wind direction and cross wind direction:

$$L_{wind} = 2\tan(\alpha)d_0 \tag{A.1}$$

For the wave crest the distance between the beam shaping element and the water surface is $d_{min} = 1.3$ m and for the trough of the wave it is $d_{max} = 1.5$ m.
The two individual intensity profiles are now mapped onto each other. Therefore a discrete grid is created with spacing of 1 mm per pixel. The distance between the centres of the individual intensity profiles is chosen in a way, that the two profiles match exactly for the case of a water surface that is not elongated. This case is shown in figure A.2. For the case of the largest distance between the

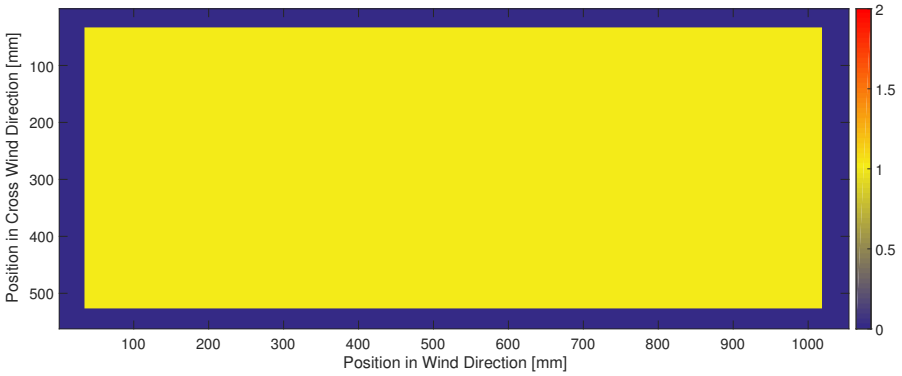

Figure A.2.: Artificial intensity distribution at the water surface for a distance of 1.4 m between the beam shaping element and the water surface. This case corresponds to a calm water surface without elongation due to waves. The colour corresponds to the artificial intensity.

beam shaping element and the water surface, i.e. in the trough of the wave, the intensity distribution is shown in figure A.3. The mean heat flux density for each of the cases described above is obtained by calculating the mean in cross wind direction for each pixel in wind direction. This has been done for 41 iteration steps for distances from 1.3 m to 1.5 m between the beam shaping element and the water surface. The values shown in figure 4.12 are then obtained from the mean of the heat flux densities from the 41 height steps at each pixel in wind direction. The error is given by the standard deviation of these heat flux densities.

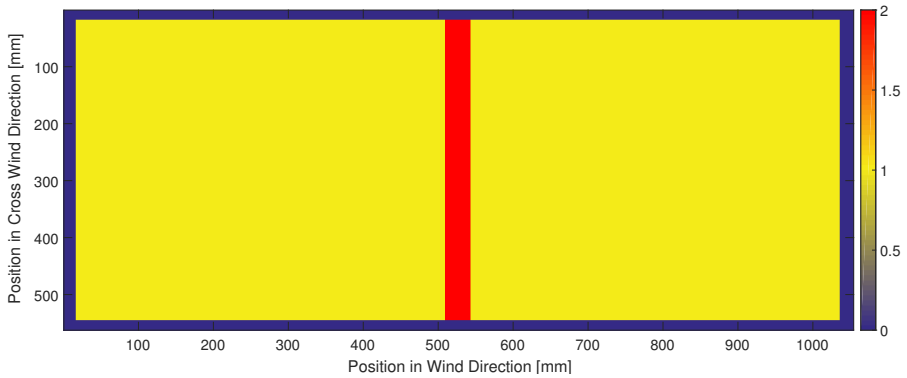

Figure A.3.: Artificial intensity distribution at the water surface for a distance of 1.5 m between the beam shaping element and the water surface. This corresponds to the distance between the beam shaping element and the trough of the largest waves observed in the Marseille facility. The colour corresponds to the artificial intensity.

Incident Laser Beams with Inclination to the Water Surface

For the case with tilted incoming laser beams, shown in figure 4.12 (b), (d) and (f), the discretization is also chosen with 1 mm resolution for the spatial coordinate on the water surface and with 41 steps to cover the wave elongations, that correspond to distances between 1.3 and 1.5 m between the water surface and the beam shaping element. Thus, the vertical resolution is 0.5 mm. The elongation in cross wind direction $L_{\text{cross-wind}}$ for a beam, that has an inclination of $2\alpha = 19.92°$, can again be calculated from simple geometrical considerations. Figure 4.7 visualizes this situation for a single laser beam. $L_{\text{cross-wind}}$ for distances d between beam shaping element and water surface is given by

$$L_{\text{cross-wind}} = \sqrt{d + L_{\text{wind}} \tan(2\alpha)} \tag{A.2}$$

Two such single beam profiles are combined in a way, that the two beam profiles match at the smallest cross wind elongation as shown in figure 4.12 (d). In this way the cross wind elongation can be calculated for each pixel in wind direction and for each distance between the beam shaping element and the water surface. The artificial heat flux density is then taken as the inverse of the cross wind direction at each pixel in wind direction. The dimensions are thus not correct for an intensity, but the calculation is only intended to serve as an estimation for the optimal experimental configuration. Again the mean of the heat flux density

at each pixel in wind direction for the 41 different heights is calculated and the error is again given by the standard deviation of this averaging process. The result of this calculation is shown in figure 4.12 (f).

A.3. Bad Pixel Removal

In section 6.2 the bad pixel removal from the recorded measurement data was discussed. As explained there for the evaluation of the data for this thesis a 5x5 median filter was applied to each image in order to get rid of the bad pixels and to smoothen the images. In cases where this smoothing process should be avoided a different approach can be taken to replace only the bad pixels and leave the other pixels unaffected. For this approach a mask **B** is created, where all bad pixels are marked with the value one. All other pixels have the value zero. The selection of bad pixels has been tested experimentally and the optimal results were obtained for the following criterion: if the value of a single pixel exceeds the mean intensity of the whole image by more than 0.5 times the standard deviation of this mean value or if the value of a single pixel is more then 0.5 times the standard deviation smaller than the mean value, then it is selected as a bad pixel. A 5x5 median filter is then applied to the original image and multiplied with the mask **B**. In this way the newly created correction image **C** contains median values at the positions of the bad pixels. An inverted mask $\mathbf{B}^{-1}$ is then multiplied with the initial image **I**, which yields an image which is identical to the initial image but contains only zero entries at the positions of the bad pixels. Finally the corrected image **F** is obtained by adding the correction image **C**:

$$\mathbf{F} = (\mathbf{B})^{-1} \cdot \mathbf{I} + \mathbf{C} \tag{A.3}$$

Danksagung

Ich möchte mich ganz herzlich bei allen bedanken, die zum Gelingen dieser Arbeit beigetragen haben.
Zuallererst möchte ich Prof. Dr. Bernd Jähne dafür danken, dass er mir diese spannende Arbeit ermöglicht hat. Durch ihn habe ich viele neue Themengebiete entdeckt und meinen Horizont erweitern können. Ganz besonders möchte ich mich auch dafür bedanken, dass er es mir ermöglicht hat, an internationalen Konferenzen und an der Messkampagne in Marseille teilzunehmen.
Bei Prof.Dr. Werner Aeschbach bedanke ich mich für die Übernahme der Zweitbegutachtung dieser Arbeit.
Prof. Dr. Rüdiger Klingeler und Prof. Dr. Georg Wolschin danke ich für ihre Bereitschaft, Teil meines Prüfungskomitees zu sein.
Der gesamten Windkanal-Arbeitsgruppe danke ich für die stets gute Arbeitsatmosphäre.
Dr. Kerstin Krall danke ich für die gute Zusammenarbeit während der Messkampagnen am Aeolotron und in Marseille. Außerdem danke ich ihr für die Bereitstellung der Gastransferdaten und der Schmidtzahlexponenten für die Meerwasserkampagne und die Messkampagne vom Oktober 2016.
Dr. Christine Kräuter danke ich für die gute Zusammenarbeit während der Fetchmessungen im Sommer 2015.
Dr. Daniel Kiefhaber danke ich für die Implementierung der live-Auswertung der ISG. Christin Proß danke ich für die kurzfristige Schnellauswertung von Teilen der ISG-Daten für die Messkampagne vom Oktober 2016.
Bei Maximilian Bopp möchte ich mich für die gute gemeinsame Planung, Vorbereitung und Umsetzung aller Arbeiten bezüglich der optischen Messtechniken für die Messungen in Marseille bedanken. Außerdem danke ich ihm für die zahlreichen Hilfestellungen rund um den Kanal und für die Bereitstellung der Schubspannnungsgeschwindigkeiten für fast alle Messkampagnen am Aeolotron.
Dr. Leila Nagel danke ich für ihre Hilfe am Anfang meiner Promotion, rund um

alles, was mit Thermographie zu tun hat. Dr. Jana Schnieders danke ich für die Hilfe beim Aufbau der ersten Version der Strahlführung für den Homogenisierer. An dieser Stelle möchte ich außerdem allen danken, die mir im Laufe dieser Arbeit beim Justieren des CO_2-Lasers geholfen haben und die mit mir gemeinsam zahlreiche Justierlöcher in unzählige Styrodur-Plättchen gebrannt haben...
Dr. Wolfgang Mischler danke ich für sämtliche Hilfestellungen rund um den Framegrabber der IR-Kamera.
Angelika Klein danke ich für das Korrekturlesen von großen Teilen dieser Arbeit und die gute Zusammenarbeit während der Messkampagne im Oktober 2016.
Nicht zuletzt möchte ich mich bei Dr. Günther Balschbach für diverse Hilfestellungen bedanken, sei es beim Konfigurieren von Servern, beim Transport von Messgeräten oder beim Korrekturlesen von Teilen dieser Arbeit.
Desweiteren möchte ich Karin Kruljac und Barbara Werner danken, die mich bei administrativen Aufgaben immer gut unterstützt haben.
I want to thank Dr. Mariana Ribas-Ribas for providing the Triton X-100 equivalent concentrations of natural surfactants, meaured during the sea water campaign.
Merci à Dr. Guillemette Caulliez pour la bonne collaboration et la possibilité d'exécuter une campagne de mesure à Luminy. Merci aussi pour les resultats de mss et u_*.
Zu guter Letzt möchte ich mich bei meiner Familie und bei meinen Freunden bedanken, die mich stets unterstützt und in meinen Vorhaben bestärkt haben. Ganz besonderer Dank gebührt meiner Freundin Elisabeth Brühl, insbesondere für ihre Unterstützung und ihre Geduld in der letzten Phase dieser Arbeit.